Energy Advances



REVIEW ARTICLE

View Article Online



Cite this: Energy Adv., 2022.

Received 5th May 2022, Accepted 2nd October 2022

DOI: 10.1039/d2ya00106c

rsc.li/energy-advances

Recent progress in ZnCo₂O₄ and its composites for energy storage and conversion: a review

Josué M. Goncalves, 🕩 * a Matheus I. da Silva, a Murillo N. T. Silva, b Paulo R. Martins, 60 Edson Nossol, Henrique E. Toma 60 and Lucio Angnes 60 *

Transition metal oxides have attracted growing attention for application in energy storage and conversion technologies. In particular, spinel-based materials, such as ZnCo₂O₄, exhibit structures suitable for performing as multifunctional electrodes in energy devices. In fact, great efforts have been dedicated to the design of micro- and nanomaterials based on ZnCo₂O₄, using different synthesis approaches and controlled conditions. Consequently, interesting morphologies and structures have been recently obtained, exhibiting outstanding electrochemical performance. Hence, in this review we report a comprehensive survey of the progress of multifunctional ZnCo₂O₄-based materials, focusing on the development of supercapacitor devices and batteries. The top 10 electrode materials for each application are highlighted, including key findings in the development of slurry-cast or binder-free electrodes. In addition, the main strategies in the design of ZnCo₂O₄-based electrocatalysts for the oxygen evolution reaction (OER) and hydrogen evolution reaction (HER) are reviewed, including electrocatalysts capable of performing tetra-electron oxygen reduction reactions (ORRs).

1. Introduction

Clean, sustainable and efficient technologies for energy production, conversion, and storage are becoming crucial for the energy crisis which is confronting the world. In this regard, the development of new electrode materials may play a primary role, impacting the performance of these energy systems.¹ Therefore, materials chemistry is becoming the key to the design of systems that can overcome the current challenges of our modern society. Among the emerging challenges, one can highlight the development of electrode materials capable of using solar energy and/or electricity to promote the oxygen evolution reaction (OER) and the hydrogen evolution reaction (HER) by electrochemical and/or photochemical water-splitting processes, respectively. This corresponds to the conversion of renewable energy into a high-energy-content chemical species, approaching the ultimate clean energy resource due to the zero emission of carbonaceous species.² Another challenging step is how to store energy more efficiently, especially in a faster way, e.g., by assembling devices with high energy and power density. This is the case of hybrid supercapacitors (HSCs) combining the outstanding power density of supercapacitive materials with the high-energy density of battery-type materials.³

Among the emerging materials recently studied, transition metal oxides (TMOs) deserve special consideration because of their rich redox chemistry and abundant density of active sites, in addition to their low cost, environmental friendliness, and excellent electrochemical performance.4,5 In fact, special attention has been given to spinel materials with a bimetallic oxide structure of the typical chemical formula AB₂O₄. Spinels consist of cation A, typically charged as 2+, in tetrahedral sites (Td), and cation B charged as 3+ occupying octahedral sites (O_b).⁶ The interest in this type of material is justified by its higher electrochemical activity, electrical conductivity, and more abundant redox reactions, compared with monometallic oxides of the types A₃O₄ and B₃O₄.^{7,8}

It is also important to mention that among various spineltype oxides, structures based on bimetallic cobaltite (MCo₂O₄, where M = Mg, Ni, Zn, Cu, Fe, and Mn) have been most widely reported,9 as recently summarized in several review articles. In particular, one can highlight the use of nickel cobaltite spinel (NiCo2O4) in different applications such as in supercapacitors, 9,10 batteries 11 and sensors. 12 Similarly, Gonçalves et al.8 summarized the main advances in MnCo2O4-based materials for energy applications and the main strategies used for the design of these materials, including HSCs, LIBs and MABs, as well as the advancements achieved as electrocatalysts for water-splitting, more specifically for the HER and OER. Similarly, Wu and colleagues¹³ highlighted the current research

^a Instituto de Química, Universidade de São Paulo, Av. Prof. Lineu Prestes 748, 05508-000, São Paulo-SP, Brazil. E-mail: josuemartins@usp.br, luangnes@iq.usp.br

^b Institute of Chemistry, Federal University of Uberlândia, Av. João Naves de Ávila 2121, 38400-902, Uberlândia-MG, Brazil

^c Instituto de Química, Universidade Federal de Goiás, Av. Esperança s/n, 74690-900,

progress regarding synthetic strategies for MgCo2O4-based electrode materials and their applications in supercapacitors, Li-ion batteries, Mg-ion batteries, and some other rechargeable ion batteries. J. Sun, C. Xu & H. Chen¹⁴ reviewed the synthesis of CuCo₂O₄-based electrode materials and their applications in supercapacitors, while Gao et al. 15 briefly summarized the recent applications of FeCo2O4 (and CoFe2O4) in energy storage and conversion, as well as the current understanding of the mechanisms and especially the relevance of morphologies and structures and composites to the electrochemical performance.

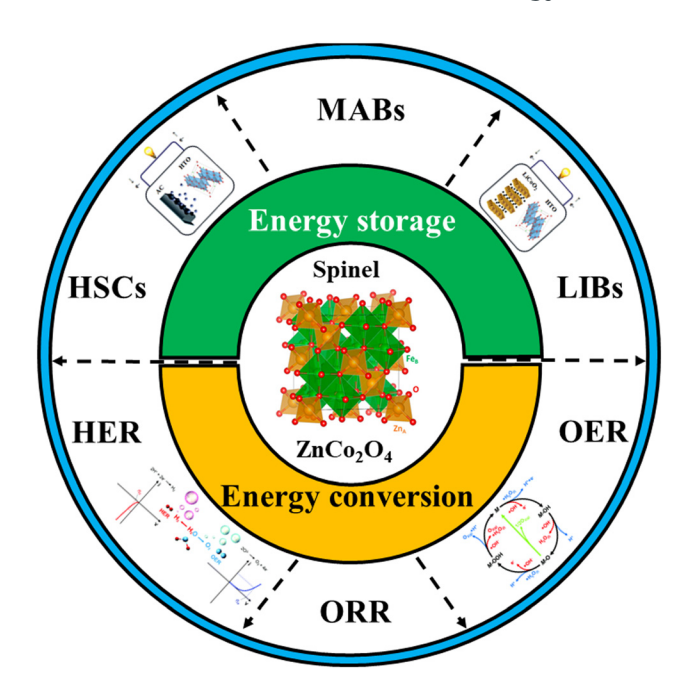
As shown above, several review articles show the progress made for Mg, Mn, Fe, Cu and especially Ni cobaltite. However, to our knowledge, more than 800 papers report the syntheses and/or use of ZnCo₂O₄ spinel for various applications, including sensor, and energy conversion and storage applications. Its multifunctionality and excellent electrochemical properties are closely related to its structure which presents a regular spinel structure where Zn²⁺ only replaces Co²⁺ in the T_d sites in Co₃O₄, leaving the Co³⁺ content in the O_h sites unchanged, while Ni and Mn mainly occupy Oh sites in NiCo2O4 and MnCo2O4.16 In fact, the effect of the oxidation state and cation distribution in the spinel on the electrocatalytic activity for the OER in an alkaline solution has been studied, and a comparison of the electrochemical and physicochemical behavior of MCo₂O₄ (where M = Mn, Fe, Co, Ni, and Zn) was made by M. Harada, F. Kotegawa, & M. Kuwa. 16 Interestingly, their catalytic activity for the OER follows the order: $ZnCo_2O_4 > NiCo_2O_4 > FeCo_2O_4 > Co_3O_4 > MnCo_2O_4$. According to the authors, the active sites for the OER are M³⁺ species in the octahedral site, and their activities are significantly dependent on the Co³⁺/Co²⁺ and M³⁺/M²⁺ content ratios in the octahedral site as demonstrated according to XPS and in situ X-ray absorption fine structure (XAFS) measurements, demonstrating the importance of the presence of Zn²⁺ ions in ZnCo₂O₄. ¹⁶ Complementarily, ZnCo₂O₄ is a promising energy storage material which shows advantageous properties, including low cost, low-toxicity, different morphologies, high electrical conductivity, 17,18 and high theoretical capacity in comparison with unitary ZnO and CoO and binary Co₃O₄. 17

Inspired by the above considerations, and despite being the second most reported cobaltite, as far as we know, there is no review work summarizing recent progress in ZnCo₂O₄ in energy applications. Therefore, in this review article we focus on ZnCo₂O₄ and its composites as electrode materials for energy technologies, including the main strategies used for the design (Scheme 1) of HSCs, LIBs and MABs, as well as the advancements as electrocatalysts for water-splitting (HER and OER) and the ORR. The pros and cons of using this spinel in the different devices are critically discussed, encompassing the perspectives and possible future directions.

2. Water-splitting and electrochemical energy storage systems

2.1. Water-splitting

Electrocatalytic water-splitting is an effective way to produce hydrogen with high purity.²² The overall reaction includes two



Scheme 1 Applications of ZnCo₂O₄-based materials. Reproduced with permission.¹⁹ Copyright © 2018, The Author(s). Creative Commons CC BY license. Reproduced with permission.²⁰ Copyright Royal Society of Chemistry, 2017. Reproduced with permission. 21 Copyright: © 2021 by the authors. Licensee MDPI, Basel, Switzerland (CC BY).

half reactions, e.g., HER and OER, taking place, respectively, at the cathode and the anode, 23 as shown in Fig. 1A. In addition, the water splitting reactions are dependent on the pH, as expected for reactions involving protons,23 as demonstrated by the equations presented in Fig. 1B. For instance, for the HER, there are two main steps on the electrode surface, described by the Volmer-Heyrovsky and Volmer-Tafel mechanisms proposed for acidic and basic solutions²⁴ (Fig. 1C). On the other hand, the OER is a more complex, requiring a high energy to overcome the sluggish kinetic barrier associated with the four-electron transfer process, and involves a larger overpotential²⁵ (Fig. 1C).

The electrocatalytic performance is usually measured by linear sweep voltammetry (LSV), cyclic voltammetry (CV)²⁵ and electrochemical chrono-methods where several parameters are used to classify catalysts according to their performance, and even to unravel the reaction mechanisms. Among the electrochemical activity criteria, the overpotential (η) , Tafel slope and stability are the most used ones to study the performance of electrocatalysts based on metal oxides/hydroxides.

The overpotential (η) is one of the essential criteria to evaluate the activity of electrocatalysts. It represents the difference between the potentials for achieving a specific current density and the onset potential to start the reaction (HER = 0 V and OER = 1.23 V). 25 Generally, the overpotentials at a current density of 10 mA cm⁻² (η_{10}) are used to compare the electrocatalytic activity between different catalysts. This corresponds to the equivalent efficiency of 12.3% for photoelectrochemical water splitting.25 In practice, a catalyst providing an overpotential in the range of 300-400 mV is considered to be an excellent

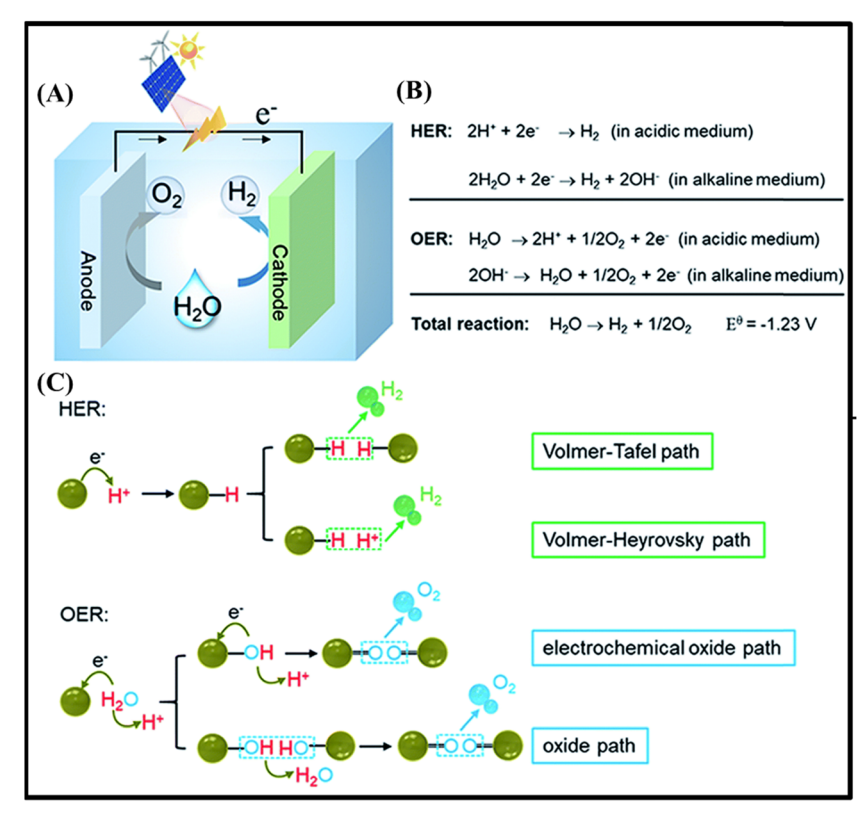


Fig. 1 (A) Scheme of a conventional water electrolyzer. (B) Water splitting reactions under acidic and alkaline conditions. (C) Proposed mechanisms of the HER and OER in an acidic aqueous solution. Reproduced with permission.²⁶ Copyright Marketplace™, Royal Society of Chemistry.

catalyst for the OER. 27,28 However, η_{10} has a great influence on the loading mass even considering the same geometrical area; thus it cannot be the only criterion to evaluate the activity.²⁵ In this regard, Tafel analysis provides additional information to understand the reaction kinetics and mechanism, such as the magnitude of the slope, which helps in establishing the ratedetermining step and the response sensitivity.²⁷ For instance, Tafel slopes of 120, 40 and 30 mV dec⁻¹ were observed, respectively, for the Volmer, Heyrovsky and Tafel determining rate steps. The smaller value of the Tafel slope means a faster electron-transfer kinetics of the electrocatalyst. 22,24,25

In addition to low overpotential and Tafel slope values, a good electrocatalyst should also be stable for long periods of time, under operating conditions. This evaluation can be performed by different techniques, including continuous CV cycling and LSV. The measurements allow comparing the overpotentials before and after cycling.²⁵ Another way to obtain information about the stability of electrocatalysts is by galvanostatic or potentiostatic electrolysis, registering the variation of potential or current density.²⁵

In summary, the overpotential (η) , Tafel slope and stability are the main criteria to categorize electrocatalysts based on ZnCo₂O₄, for the OER and HER.

2.2. Electrochemical energy storage systems

In an effort to overcome past limitations, recent years have seen intense research efforts in energy storage areas, such as fuel cells, capacitors, supercapacitors, and batteries. Electrochemical energy storage systems (EESSs) play a critical role in renewable energy integration applications. They serve as energy sources to provide power supply and/or energy buffers to improve efficiency and the overall economy. This has triggered intensive research efforts in the past three decades, which have resulted in the advent of modern EESSs such as batteries and supercapacitors.29-31

2.2.1. Supercapacitor materials and devices. An important point that should be clarified in the initial evaluation of electrode materials is whether their electrochemical data correspond to a battery or a supercapacitor. Electrodes with a capacitor-like behavior present cyclic voltammograms (CVs) and linear potential responses during constant-current discharging (Fig. 2A–C). In contrast, the battery-type electrode presents CVs with defined oxidative and reductive peaks (Fig. 2G and H) and flat (plateau) galvanostatic charge/discharge (GCD) profiles (Fig. 2I). One criterion that could help the identification of the electrode's nature is the analysis of current versus scan rate curves. For battery-type materials, the peak current (i) will be proportional to the square root of the scanning rate $(i \sim v^{1/2})$, whereas for a capacitor-like electrode the current will be proportional to the scan rate $(i \sim \nu)$.³²

Distinct from conventional capacitors, supercapacitors store charges electrochemically but show high-energy density compared to the former, with high rate capability and excellent cycling stability. According to their charge storage mechanisms,

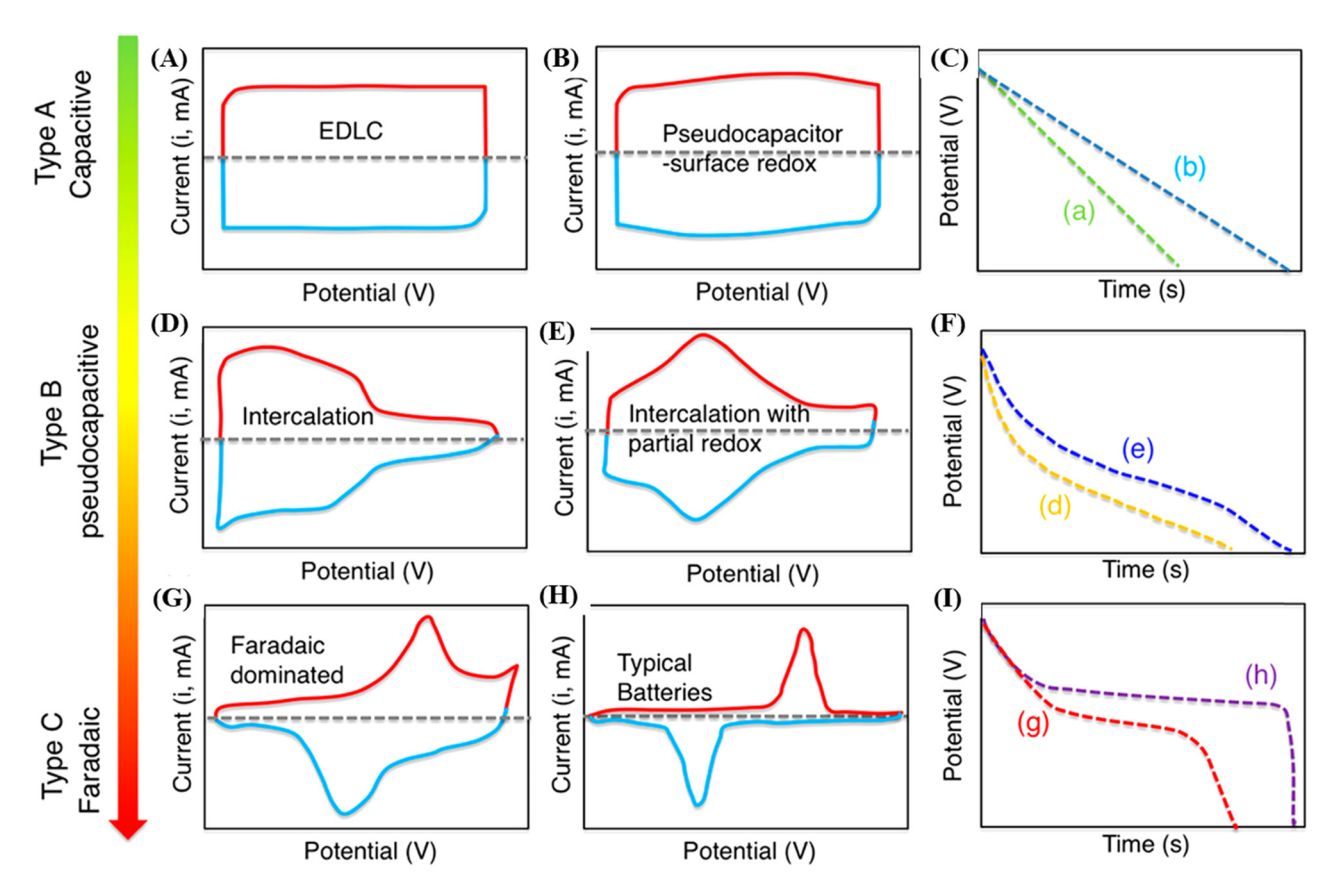


Fig. 2 Illustrative cyclic voltammograms (A, B, D, E, G and H) and the corresponding GCD curves (C, F and I) for different types of energy-storage materials. Electrochemical double-layer capacitors: CV profile (A) and the corresponding discharge curve (C). A pseudocapacitive electrode could present an electrochemical response of one, or a mix, of the following categories: (B and C) surface redox materials and (D-F) intercalation-type materials. Electrochemical profiles in (G-I) correspond to battery-like materials. Reproduced with permission. 32 Copyright © 2018 American Chemical Society.

supercapacitors are divided into two categories, namely, electrochemical double-layer capacitors (EDLCs) and pseudocapacitors.³³ In EDLCs, the electrochemical behavior is due to the storage of charges at the electrode/electrolyte interface by establishing electrochemical double layers through a nonfaradaic process (Fig. 2A and C.a). In pseudocapacitors, the electrochemical behavior in terms of current is neither totally capacitive nor entirely faradaic (like batteries). These electrodes present fast and reversible oxidation/reduction reactions through either intercalation or surface ion processes and quasi-rectangular CVs and quasi-linear GCD curves.34 In surface-redox pseudocapacitors, the charge storage is mostly assigned to the charge transfers occurring at the surface of the material. As can be seen in Fig. 2B and C.b, the CV and the GCD characteristics for surfaceredox pseudocapacitors present the linear dependency of the charge storage over the entire potential window, storing charges through surface faradaic and double layer mechanisms. Intercalation-type materials involve the core of the electrode materials and are expressed by the intercalation of charges between layers or in channels originating from the faradaic reaction and lack of phase changes during cycling (Fig. 2D-F).³⁵

EDLCs can reach fast charging/discharging rates and high cycling stability. However, the energy density of this type of material is relatively low, due to the deficient contact at the electrode/electrolyte interface. On the other hand, the capacitance of pseudocapacitors is attributed to the fast and reversible redox process of materials, such as some transition metal oxides/hydroxides and conducting polymers. Hence, pseudocapacitors can provide higher specific capacitance but present lower power density,² due to the low conductivity of pseudocapacitive materials. In this way, one strategy to increase the performance of electrodes is the preparation of nanocomposites containing carbon structures.³⁶

The configuration of conventional supercapacitors is based on button cells or spiral-wound designs, which are composed of two collectors, two electrodes, and a separator, all soaked in electrolyte.37 Distinct from the case of conventional supercapacitors, the development of materials in smart configurations (films, fibers, and micro-scale supercapacitors) has increased, aiming for the construction of thin, flexible, and even foldable devices. Thinfilm electrodes are prepared with a layer of active material with its thickness varying from nanometers to micrometers, resulting in short charge and ion transport distances, and thus promoting fast physical or chemical processes during charge storage.³⁸ Fiber supercapacitors are commonly designed like 1D wires with diameters varying from micrometers to millimeters and constructed based on parallel, twisted, coaxial, or woven structures.³⁹ Microsupercapacitors generally consist of a vertical structure composed

Energy Advances Review

of two electrodes and electrolyte sandwiched in the middle of both or, in the case of the in-plane interdigital device architecture, electrodes are separated by an insulated gap, with no need for separators in the construction of the device. The electrolyte is subsequently deposited on the top of devices to guarantee ion transport between electrodes. The total size of microsupercapacitors could be in the order of millimeters. 36,40

2.2.2. Rechargeable batteries. Unlike capacitors and supercapacitors, battery cells have high specific capacity values and high volumetric and gravimetric energy density values. In battery electrodes, during charging, ions are deintercalated (extracted) from the cathode and diffuse into the anode via the electrolyte medium, which is a conductor for ions and an insulator for the electrons generated at the cathode, while the electrons reach the anode via an external circuit, whereas discharging reverses this process. This is followed by faradaic charge transfer processes to generate the energy capacity (mA h kg⁻¹). Thus, the specific capacity obtained in battery electrodes is limited by solid-state ion diffusion, exhibiting relatively poor kinetics; however, the use of the entire bulk of the electrode for charge storage leads to very high energy density.^{29,41-43}

Among a number of different energy storage technologies, metal-ion batteries, in particular lithium-ion batteries (LIBs), have recently been accepted as the leading candidate for commercial EESSs. LIBs, as the main power source, dominate the portable device market due to their high energy density, high output voltage, long life and environmentally friendly operation. 31,44 It is important to mention that many review works already published highlighting recent progress, 45-47 issues and challenges facing rechargeable LIBs, 48 as well as rechargeable sodium-ion batteries (SIBs) as potential alternatives to current LIBs, 49 which can be used to obtain more detailed information about these EESSs.

On the other hand, metal-air batteries (MABs) are a family of electrochemical cells powered by metal oxidation and oxygen reduction; in this system oxygen is used as the active cathode material. This oxygen is obtained from air, which diffuses into the electrolyte from the atmosphere and undergoes reduction at the cathode, exhibiting a great advantage regarding theoretical energy density, which is about 3-30 times higher than those of commercial LIBs. 50-52

In typical continuum-based models, the cathode material is considered as a porous medium and the structure is represented by several parameters, such as porosity, permeability, and tortuosity.⁵² In addition, it is necessary to design oxygen electrode catalysts with special structures for use in MABs to overcome the sluggish kinetics of the oxygen reduction reaction (ORR) and the oxygen evolution reaction (OER).53-55

3. ZnCo₂O₄-based materials for energy storage applications

3.1. ZnCo₂O₄-based electrode materials for supercapacitive applications

One of the best electrochemical performances is observed for RuO2 as a supercapacitor electrode material, exhibiting a high

specific capacitance of 1580 F g⁻¹. However, because of its high cost and element scarcity, it becomes necessary to seek environmentally friendly and low-cost alternative electrode materials. Recently, transition metal oxides (TMOs) such as MnO2, NiO, and Co3O4 have been studied as promising electrode materials for supercapacitor applications, ⁵⁶ especially those based on doped-Co₃O₄. The bimetallic oxide ZnCo₂O₄ has recently attracted much attention because of its excellent electrochemical properties, with lower activation energy, higher conductivity and electroactivity in comparison with pristine Co_3O_4 . It also exhibits high theoretical capacitance (2604 F g⁻¹), and is environmentally compatible and a cost-effective and abundant material. In addition, ZnCo₂O₄ presents a p-type semiconducting nature, which influences the electrical conductivity of the material, and shares the same Co3O4 spinel crystal structure. The replacement of Co2+ ions with Zn2+ ions, with Zn occupying the tetrahedral sites and Co occupying the octahedral sites, results in much richer redox reactions. However, ZnCo₂O₄ has the disadvantage of exhibiting an intrinsically poor electrical conductivity, involving large volume changes through the charge/ discharge processes. This leads to some intrinsic electrical insulation, showing rapidly fading capacitance at higher current densities and during charge/discharge cycles, thus usually presenting low rate-capability and cycling stability. 57,58

Therefore, to overcome these limitations, rational design of suitable electrode materials is imperative, since the electrochemical performance strongly depends on their mechanical properties. To surpass the limitations of ZnCo₂O₄-based electrodes for supercapacitor applications, it is important to seek for an optimized morphology that can provide high active surface area, short lengths and high rates of ion and electron diffusion. Plenty of redox sites should be available. For this reason, pristine ZnCo₂O₄ has been synthesized as microparticles, ⁵⁹ microsheets, ⁶⁰ microspheres, ⁶¹⁻⁶⁴ microflowers, ^{65,66} nanoparticles (NPs), ^{67,68} nanocubes, ⁶⁹ nanosheets, ⁷⁰⁻⁷³ nanoplates,⁵⁶ nanoflowers,⁷⁴ nanorods,⁷⁵ nanospheres,⁷⁶ and nanotubes⁷⁷ to produce slurry-cast supercapacitive electrodes (Table 1).

Other strategies rely on the production of hybrid materials, such as composites and core@shell structures, which will be discussed later, and/or combining the morphology design and hybrid materials engineering with binder-free and selfsupporting architectures. The use of binders to produce slurrycast electrodes for supercapacitor applications significantly reduces the electronic conductivity, limits the active material availability, hinders the ion-diffusion, and increases the mass density as "dead-mass". Additionally, after repetitive redox reactions, the material can lose the integrity and/or peel-off from the substrate, reducing the capacitance retention through several charge/discharge cycles. Therefore, the above-mentioned downsides can be resolved by the growth of ZnCo₂O₄ electroactive materials directly on the surfaces of electrode substrates, such as nickel foam (NF), carbon foam (CF) and carbon cloth (CC). These strategies not only avoid "dead-mass" but also greatly improve the electroactive surface area, and offer fast electron transportation and short ion diffusion paths. In addition, these strategies will decrease the resistance between the electroactive material and

Table 1 Relevant electrochemical parameters of pristine $Z_{D_x}C_{D_3-x}O_{4}$ -based slurry-cast electrodes and their performance in supercapacitive energy storage devices assembled with a suitable cathode material

							Negative	
Electrode material	Specific capacitance or specific capacity	Potential window (V)/ref. electrode	Rate capability/ current density range	Stability retention/cycle numbers	Stability retention/cycle Highest energy numbers density (W h ${\rm kg^{-1}})$	Highest power density (W ${\rm kg^{-1}}$)	electrode material in SCs	Ref.
ZnCo ₂ O ₄ nanocubes	434 F g ⁻¹ at 5 mV s ⁻¹	-0.5 to	9.9%/5-50	ı			ı	69
Peony-like ZnCo ₂ O ₄ nanoparticles	$440 \text{ F g}^{-1} \text{ at } 1 \text{ A g}^{-1}$	0.5/Ag/AgCI 0.0-0.55/SCE	(mV s ⁻) 67.7%/1-10	155.6%/3000	29.76 at 398.53 W kg ⁻¹	I	AC	89
Mesoporous ZnCo ₂ O ₄ nanosheets	3.3 F cm $^{-2}$ at 1.01 mA cm $^{-2}$	0.0-0.35/SCE	59.8%/1-10	96.5%/5000	$33.98 \text{ at } 800 \text{ W kg}^{-1}$	$4800 \text{ at } 16.67 \text{ W h kg}^{-1}$	AC	20
Hollow ZnCo ₂ O ₄ microspheres	$78.89 \text{ mA h g}^{-1} \text{ at } 1 \text{ A g}^{-1}$	0.0-0.5/SCE	56%/1-10	145%/2000	27.78 at 158.5 W kg ⁻¹	920.8 at 12.62 W h kg ⁻¹	AC	62
es	$805.3 \text{ F g}^{-1} \text{ at } 1 \text{ A g}^{-1}$	0.0-0.5/Ag/AgCl	56%/1-25	88%/5100			Symmetric	26
${ m ZnCo_2O_4}$ nanosheets	$290.5 \text{ F g}^{-1} \text{ at } 0.5 \text{ A g}^{-1}$	0.0-0.45/Ag/AgCl	64.3%/0.5-10	1	$0.46 \text{ at } 22.44 \text{ W kg}^{-1}$	$107.53 \text{ at } 0.21 \text{ W h kg}^{-1}$	Symmetric	71
ZnCo ₂ O ₄ microparticles	$158 \text{ F g}^{-1} \text{ at 5 mV s}^{-1}$	-0.4 to $0.6/SCE$	7.6%/5-200	75%/1000	1	1	1	29
			$(mV s^{-1})$					
Urchin-like ZnCo ₂ O ₄ microspheres	$677 \text{ F g}^{-1} \text{ at } 1 \text{ A g}^{-1}$	0.0-0.45/SCE	77.5%/1-15	107.3%/5000	1		I	64
	689 F g^{-1} at 1 A g^{-1}	0.0-0.44/SCE	81.3%/1-15	98.7%/2000			I	65
	$126 \text{ F g}^{-1} \text{ at } 1 \text{ A g}^{-1}$	0.0-0.6/SCE	77.7%/1-7	1	1		I	61
cles	843 F g^{-1} at 1 A g^{-1}	0.0-0.45/Ag/AgCI	72.7%/1-3	97%/5000	$26.28 \text{ at } 716 \text{ W kg}^{-1}$	$3850 \text{ at } 3.85 \text{ W h kg}^{-1}$	AC	29
Porous ZnCo ₂ O ₄ nanosheets	$3.07 \mathrm{\ Fcm}^{-2}$ at	0.0-0.35/SCE	61.2%/1.04-10.4	96.3%/5000	$42.83 \text{ at } 425 \text{ W kg}^{-1}$	8500 at 12.99 W h kg ⁻¹	AC	72
	1.04 mA cm^{-2}							
Sheet-like ZnCo ₂ O ₄ microstructures		$0.0-0.4/\mathrm{Ag/AgCl}$	19.9%/10-1000	170%/1000	1	1	1	09
	$10~\mu\mathrm{A~cm}^{-2}$							
Mesoporous ZnCo ₂ O ₄ microflowers	$680 \text{ F g}^{-1} \text{ at } 1 \text{ A g}^{-1}$	0.0-0.4/Ag/AgCI	89.4%/0.35-1	0002/%06	,	,		99
sre	$763.32 \text{ Fg}^{-1} \text{ at } 1 \text{ Ag}^{-1}$	0.0-0.5/Hg/HgO	55.31%/1-30	89.42%/20000	40.49 at 397.37 W kg ⁻¹	50 080 at 20.87 W h kg ⁻¹	AC	74
Rod-like ZnCo ₂ O ₄ nanoparticles	$135 \text{ F g}^{-1} \text{ at } 1 \text{ A g}^{-1}$	0.0-0.45/Ag/AgCl	I	1	1	1	1	75
${ m ZnCo_2O_4}$ microspheres	$460 \text{ F g}^{-1} \text{ at } 1 \text{ A g}^{-1}$	0.0-0.45/Ag/AgCl	54.8%/1-5	165%/1000				63
Mesoporous ZnCo ₂ O ₄ nanosheets	$835.26 \text{ F g}^{-1} \text{ at } 1 \text{ A g}^{-1}$	0-0.38/SCE	35.6%/1-10	73.28%/1000			1	73
-like $\mathrm{ZnCo_2O_4}$	$420 \text{ F g}^{-1} \text{ at } 0.5 \text{ A g}^{-1}$	-0.1 to	\sim 71.4%/0.5 $-$ 10	1	$28.6 \text{ at } 100 \text{ W kg}^{-1}$	$2500 \text{ at } 18 \text{ W h kg}^{-1}$	NPC	9/
nanoparticles		$0.45/\mathrm{Hg/HgO}$						
Hollow ZnCo ₂ O ₄ nanotubes	$362 \text{ F g}^{-1} (181 \text{ C g}^{-1})$	0.0-0.5/SCE	75.1%/0.5-10	97.4%/10 000	$10.42 \text{ at } 375.12 \text{ W kg}^{-1}$	10.42 at 375.12 W kg $^{-1}$ 7503.75 at 6.67 W h kg $^{-1}$ AC		77
	at 0.5 a &							

current collector, provide efficient ion-diffusion channels, ensure excellent mechanical strength, enhance the electrical conductivity and accommodate the volume changes through cycling. Therefore, the challenge to fabricating highly efficient binder-free electrode materials capable of storing rapidly larger amounts of energy, at low cost, can be solved by using ZnCo₂O₄-modified electrodes. Hence, binder-free electrodes based on pristine ZnCo₂O₄ nanorods, ^{78,79} nanobelts, ⁸⁰ nanoribbons, ⁸¹ nanoflowers, ⁸² nanoflakes, ^{83,84} nanosheets, ^{85–89} nanomuscles, ⁹⁰ nanowires, ^{65,91} nanoleaves, ⁹² nanocubes, ⁹³ micro-urchins, ^{94,95} and nanoneedles ⁸⁹ were also reviewed for supercapacitor applications (Table 2) and will be discussed along with slurry-cast electrodes according to their morphology.

3.1.1. Pristine ZnCo₂O₄ electrode materials. The micro/ nano-structured ZnCo₂O₄ electrode materials discussed in this review article have been prepared via different synthetic strategies and, therefore, present distinct electrochemical performances according to their morphologies in both slurry-cast and binder-free electrodes. As expected, in general, less bulky morphologies with higher surface area and lower thickness present higher supercapacitive performance, due to the improved availability of active sites and thus the reduced amount of "dead-mass" of ZnCo2O4. Furthermore, the production of 2D, 1D, hollow and/or porous pristine ZnCo₂O₄ structures is another important factor, increasing the surface area and cycle stability. It allowed enhancing even further the active site availability and specific surface area and mass ratio, resulting in high charge/discharge capacitances even at high current densities.

In the case of $\mathrm{Co_3O_4}$ -based materials, the direct comparison between different $\mathrm{MCo_2O_4}$ materials can only be understood by further analyzing their morphologies instead of just their composition, as reported by Merabet *et al.*⁵⁹ (M = Zn, Ni, Mn, and Cu) and Alqahtani *et al.*⁶¹ (M = Zn, Ni, Mn, Cu, and Fe). Both author groups synthesized sphere-like $\mathrm{ZnCo_2O_4}$ microparticles for slurry-cast electrodes, but different morphologies were obtained for other $\mathrm{MCo_2O_4}$ species, impacting their performance. Since their sphere-like $\mathrm{ZnCo_2O_4}$ microparticles presented bulkier morphologies and lower electroactive surface, they exhibited the lowest electrochemical performance, delivering 158 F g⁻¹ at 5 mV s⁻¹⁵⁹ and 126 F g⁻¹ at 1 A g^{-1.61}

Notwithstanding, there are some structural strategies that can be applied to optimize 3D ZnCo₂O₄ morphologies for slurry-cast electrodes, *e.g.*, nanocubes $(434 \text{ F g}^{-1} \text{ at 5 mV s}^{-1})$, ⁶⁹ spherelike NPs $(843 \text{ F g}^{-1} \text{ at 1 A g}^{-1})$ ⁶⁷ and rod-like NPs $(135 \text{ F g}^{-1} \text{ at 1 A g}^{-1})$. However, even though nanocubes ⁶⁹ and sphere-like NPs ⁶⁷ presented cycling stability (97% after 5000 cycles) and relatively good specific capacitance in comparison to bulk microspheres ⁵⁹ and nanorods, ⁷⁵ they showed poor rate capability. Nonetheless, the overall stability can be further enhanced by producing hollow (78.89 mA h g⁻¹ at 1 A g⁻¹)⁶² and porous microspheres (460 F g⁻¹ at 1 A g⁻¹⁶³ and 420 F g⁻¹ at 0.5 A g⁻¹⁷⁶). Differently from bulk and smooth microparticles ⁵⁹ (Fig. 3A), which presented 75% of their initial specific capacity of hollow ZnCo₂O₄ microspheres ⁶² (Fig. 3B) increased to

145% after 2000 cycles, while porous microspheres⁶³ (Fig. 3C) delivered 165% of their initial specific capacitance after 1000 cycles. These results suggest that porous and hollow particles show superior cycling performance due to the facile mass transfer from the interconnected structure of NPs and the void/space in between the particles, alleviating the strain effects of the volume changes during charge/discharge processes. As for binder-free electrodes, there are $\rm ZnCo_2O_4$ connected nanomuscle network microstructures uniformly grown onto NF (1156.3 F g⁻¹ at 1 A g⁻¹), ⁹⁰ which originate from agglomerated nanosheets and present a highly porous 3D structure. This can partially buffer the strain effect through the charge–discharge processes, improve the specific surface area and active site availability, and lower the interior resistance, facilitating electron transfer and resulting in such high specific capacitance.

Aside from 3D ZnCo₂O₄ NPs, the literature has reported a series of 2D-structured ZnCo₂O₄, such as micro-⁶⁰ and nanosheets, ^{70–73,85–89} nanoplates, ⁵⁶ nanoflakes, ^{83,84} nanoleaves, ⁹² nanobelts, ⁸⁰ nanoribbons, ⁸¹ and those based on radial growth of nanosheets, *i.e.*, micro-^{65,66} and nanoflowers. ^{74,82} In addition, there are 1D-structured ZnCo₂O₄, such as urchin-like microspheres, ⁶⁴ nanorods ^{75,78,79} and nanotubes. ⁷⁷ Two-dimensional sheet-like morphologies are known to be generally more suitable than traditional bulk (3D) materials for supercapacitor applications, once they present high specific surface area, higher surface area-to-volume ratios, and shorter ion transportation channels due to their greatly reduced thickness in one dimension, thus improving the availability of electroactive sites for redox reactions, electrical conductivity, cycling stability and ion-diffusion rates. ^{56,60,70–73}

All sheet-like ZnCo₂O₄ materials for slurry-cast electrodes encountered in this review had superior capacitance retention through cycling in comparison to bulk spherical and cubic ZnCo₂O₄ nanoparticles due to their more stable morphology. However, they also presented some limitations in rate capability, with a significant decrease in specific capacitance at increasing current density. Presumably, the electrolyte ions have insufficient time to diffuse into the electrode material and to access the active sites at higher scan rates. Even though the highest specific capacitance between slurry-cast electrodes of 835.26 F g⁻¹ at 1 A g⁻¹ was achieved by mesoporous ZnCo₂O₄ nanosheets produced by Xiao et al. 73 (Fig. 4A), similar results were achieved with porous $Zn_{1.36}Co_{1.64}O_4$ nanoplates (805.3 F g^{-1} at 1 A g^{-1}), ⁵⁶ as well as with mesoporous ZnCo₂O₄ nanosheets (3.3 F cm⁻² at 1.01 mA cm⁻²) and porous ZnCo₂O₄ nanosheets (3.07 F cm⁻² at 1.04 mA cm⁻²).⁷² In fact, these results are attributed to their porosity and nanosized morphology. Smooth ZnCo₂O₄ nanosheets 71 delivered only 290.5 F g^{-1} at 0.5 A g^{-1} and ZnCo₂O₄ microsheets⁶⁰ delivered the poorest areal capacitance (16.13 mF cm $^{-2}$ at 10 μ A cm $^{-2}$) among all materials, along with rather low rate-capability, owing to their inferior specific surface area and the lower availability of electroactive sites, especially at higher current densities.

When assembled in binder-free electrodes, on the other hand, sheet-like $\rm ZnCo_2O_4$ materials present superb specific capacitance, rate capability and cycling stability and are quite

Table 2 Relevant electrochemical parameters of pristine $Z_{n_x}C_{O_{3-x}}O_4$ -based binder-free electrodes and their performance in supercapacitive energy storage devices assembled with a suitable cathode material

Electrode material	Specific capacitance or specific capacity	Potential window (V)/ref. electrode	Rate capability/ current density range	Stability retention/cycle numbers	Stability retention/cycle Highest energy density numbers $(W \text{ h kg}^{-1})$	Highest power density (W ${ m kg}^{-1}$)	Negative electrode material in SCs	Ref.
ZnCo ₂ O ₄ nano-rods on CC	$5.18~\mathrm{F~cm^{-2}}$ at 5 mA $\mathrm{cm^{-2}}$	$0-0.6/\mathrm{Ag/AgCl}$	59.8%/5-100	92.8%/3000	2.3 mW h cm^{-2}	-	PPy/CC	78
${ m ZnCo_2O_4}$ nano-belt-decorated 1197.14 F ${ m g}^{-1}$ at 2 A ${ m g}^{-1}$	1197.14 F $\rm g^{-1}$ at 2 A $\rm g^{-1}$	$0-0.7/\mathrm{Ag/AgCl}$	75.2%/2-10	95.01%/5000	79.48 at 894.24 W kg ⁻¹	8900 at 62.1 W h ${\rm kg}^{-1}$	AC/CC	80
Porous ZnCo_2O_4 nanoribbons 1957.7 F g ⁻¹ at 3 mA cm ⁻² 0-0 on NF	1957.7 F g^{-1} at 3 mA cm $^{-2}$	0-0.5/SCE	61.7%/3-60	84%/3000	-		I	81
O ₄ nano-flowers on NF like ZnCo ₂ O ₄ nano-	\sim 41 mA h g ⁻¹ at 2 A cm ⁻² 0-0.5/Hg/H	0-0.5/Hg/HgO 0-0.35/SCE	$\sim 45\%/1-16$ $\sim 36\%/2-20$	89%/2000 94.8%/2000	40 at 1016 W kg ⁻¹ 	$\sim\!11000$ at $\sim\!22$ W h kg $^{-1}$ Symmetric —	Symmetric —	83
Ultra-thin ZnCo ₂ O ₄ curved sheets on NF	1848.9 F g^{-1} (832 C g^{-1}) at 5 A g^{-1}	0-0.45/Ag/AgCl	88.6%/5-15	85.5%/5000	$20.31 \text{ at } 855 \text{ W kg}^{-1}$	$4250 \text{ at } 10.2 \text{ W h kg}^{-1}$	AC/NF	85
ZnCo ₂ O ₄ nano-muscle net- works on NF	1156.3 F g^{-1} 462.5 C g^{-1} at 1 A g^{-1}	$0-0.4/\mathrm{Ag/AgCl}$	71.5%/1-8	97.4%/5000	I	I	1	06
ZnCo ₂ O ₄ nano-wires on NF ZnCo ₂ O ₄ nano-flake-decorated		$0-0.5/\mathrm{SCE}$ $0-0.6/\mathrm{Ag/AgCl}$	83.6%/2-30 51.3%/2-30	88.8%/3000 95%/3000	37.5 at 358.2 W kg ⁻¹ 28.8 mW h cm ⁻² at 3 W cm ⁻²	4776.1 at 19.9 W h kg ⁻¹ 	AC/NF Fe ₂ O ₃ /3D-Ni	96 84
Porous ZnCo ₂ O ₄ nanosheet	$3.19~\mathrm{F}~\mathrm{cm}^{-2}$ at 2 mA cm^{-2}	0-0.5/Hg/HgO	83.9%/2-30	72.5%/2500	$50.7 \text{ at } 187.6 \text{ W kg}^{-1}$	$2950.4 \text{ at } 37.7 \text{ W h kg}^{-1}$	AC/NF	98
Leaf-like ZnCo ₂ 0 ₄ nano- structures on NF	$1700 \text{ F g}^{-1} \text{ at } 1 \text{ A g}^{-1}$	0-0.4/SCE	$\sim 36.8\%/1-10$	110%/8000	63 at 795.5 W ${ m kg}^{-1}$	I	AC/NF	92
$_{\rm St. Co_2O_4}^{\rm St. Co_2O_4}$ intertwined heterostructured nanocubes $_{\rm CO_2O_4}^{\rm St. Co.}$ NF.	$2040~{\rm F~g}^{-1}$ at $20~{\rm A~g}^{-1}$	0-0.5/SCE	47.7%/50-200 (mV s ⁻¹)	92%/1000	I	I	I	93
Urchin-like ZnCo_2O_4	127.8 F $\rm g^{-1}$ at 1 mA cm ⁻²	0-0.5/Ag/AgCl	64%/1-10	80.7%/3000				94
Porous $ZnCo_2O_4$ micro- urchins on NF	1527.2 F ${\rm g}^{-1}$ at 1 A ${\rm g}^{-1}$	0-0.5/Hg/HgO	78.8%/1-10	86%/2000	69.2 at 774.6 W ${\rm kg}^{-1}$	7742.2 at 35.7 W h ${ m kg}^{-1}$	AC/NF	91
wined nanosh-	$1750 \text{ F g}^{-1} \text{ at } 1.5 \text{ A g}^{-1}$	0-0.8/Ag/AgCl	72%/1.5-10	0008/%8.96	117.92 at 1490.4 W ${\rm kg}^{-1}$	13 520 at 76.69 W h kg ⁻¹	NPC/CC	87
nno-rods on FSSM nno-sheets on NF icro-urchins on NF		0-0.35/Ag/AgCl 0-0.45/SCE 0.1-0.5/Hg/HgO	92.4%/2–10 81.8%/1–10 69%/1–16	87.09%/6000 93%/5000 82.5%/10 000	25.45 at 3620 W kg ⁻¹ 14.1 at 375 W kg ⁻¹ 1.27 mW h cm ⁻² at 14.18 W cm ⁻²	~ 6050 at ~ 5 W h kg ⁻¹ 6000 at 4.4 W h kg ⁻¹ 62.27 at 0.66 mW h cm ⁻²	FeCo ₂ O ₄ /FSSM N-doped AC/NF AC/NF	79 88 95
Porous ZnCo ₂ O ₄ micro- urchins on NF	$1000 \text{ F g}^{-1} \text{ at } 20 \text{ A g}^{-1}$	0-0.5/SCE	52.6%/10-50	93%/2000	I	1	1	68
Porous Al _{0.5} Zn _{0.5} Co ₂ O ₄ nanosheets on NF	$\sim\!1200~\mathrm{F~g}^{-1}$ at 20 A g^{-1}	0-0.5/SCE	56.7%/10-50	95%/5000	I	1	I	

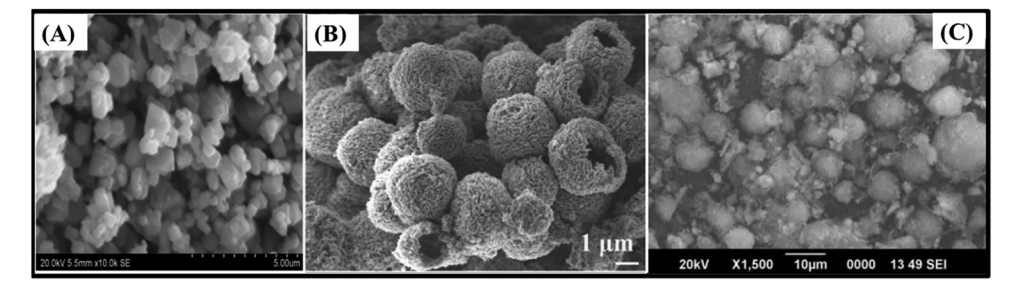


Fig. 3 (A) SEM image of bulk ZnCo₂O₄ microparticles. Reproduced with permission.⁵⁹ Copyright © 2018 Elsevier Ltd and Techna Group S.r.l. All rights reserved. (B) SEM image of hollow ZnCo₂O₄ microspheres. Reproduced with permission.⁶² Copyright © 2018 Elsevier Ltd. All rights reserved. (C) SEM image of porous ZnCo₂O₄ microspheres. Reproduced with permission. 63 Copyright © 2018, Springer-Verlag GmbH Germany, part of Springer Nature.

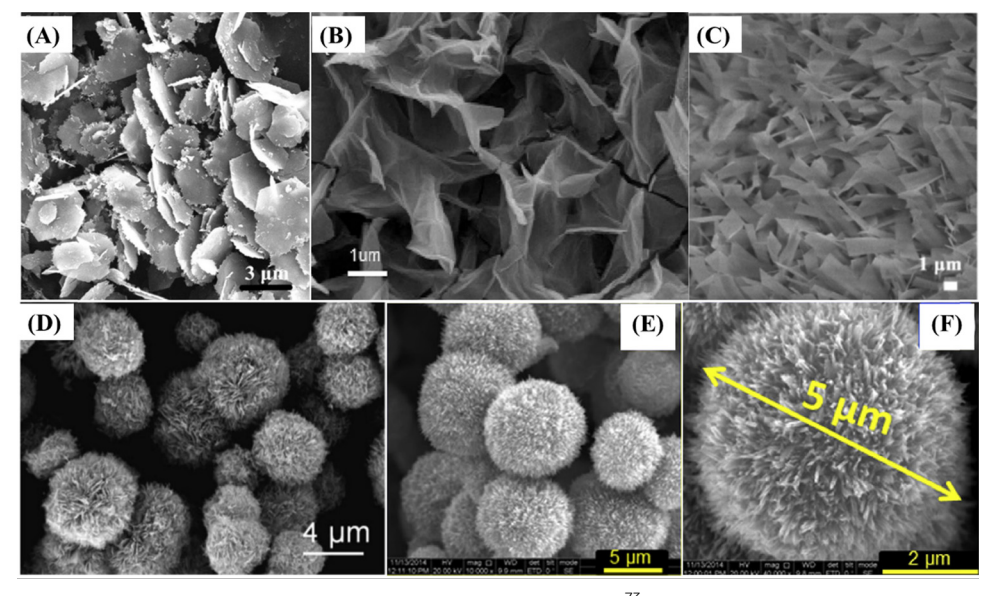


Fig. 4 (A) SEM image of mesoporous ZnCo₂O₄ nanosheets. Reproduced with permission.⁷³ Copyright © 2017, Springer-Verlag GmbH Germany, part of Springer Nature. (B) FESEM image of ultra-thin ZnCo₂O₄ curved nanosheets/NF. Reproduced with permission. **S Copyright © 2019 Elsevier Ltd. All rights reserved. (C) SEM image of porous ZnCo₂O₄ nanoribbons/NF. Reproduced with permission. 81 Copyright © 2017 Elsevier Ltd. All rights reserved. (D) SEM image of porous ZnCo₂O₄ microflowers. Reproduced with permission.⁶⁵ Copyright © 2019 Elsevier Ltd and Techna Group S.r.l. All rights reserved. (E and F) SEM images of ZnCo₂O₄ nanoflowers/NF. Reproduced with permission. 82 Copyright © 2017 Elsevier Ltd. All rights reserved.

competitive. $^{80,81,83-89,92}$ Nanosheets are the most studied 2D morphology of $ZnCo_2O_4$, $^{85-88}$ featuring porous nanosheet networks on NF (3.19 F cm⁻² at 2 mA cm⁻²), 86 intertwined nanosheet arrays on CC (1750 F $\rm g^{-1}$ at 1.5 A $\rm g^{-1})^{87}$ and NF (400 F g^{-1} at 1 A g^{-1}),⁸⁸ ultra-thin curved nanosheet arrays on NF (1848.9 F g^{-1} at 5 A g^{-1})⁸⁵ (Fig. 4B). These materials presented high rate-capabilities and cycling stabilities, besides porous nanosheet networks on NF,86 with a capacitance retention of 72.5% after 2500 cycles. Such good rate capabilities are achieved owing to the nanosheet array arrangements with adequate space between individual nanosheets, composed of many NPs and pores^{85,86,88} or intertwined nanosheets,⁸⁷ which facilitates the transport path for ion-diffusion in charge/ discharge processes.

Other binder-free electrodes based on 2D ZnCo₂O₄ materials were also produced in recent years, *i.e.* nanobelts (1197.14 F g^{-1} at 2 A g⁻¹), 80 nanoribbons (1957.7 F g⁻¹ at 3 mA cm⁻²), 81

flake-like nanostructures (\sim 41 mA h g⁻¹ at 2 A cm⁻²), ⁸³ nanoflakes (1170 F g^{-1} at 2 A g^{-1}), ⁸⁴ nanoleaves (1700 F g^{-1} at 1 A $\rm g^{-1}),^{92}$ and porous $\rm Al_{0.5}Zn_{0.5}Co_{2}O_{4}$ nanosheet arrays on NF ($\sim\!1200~F~g^{-1}$ at 20 A g^{-1}). 89

ZnCo₂O₄ nanobelt-decorated CC⁸⁰ had a similar structure to interconnected nanosheets and thus provided similar performance to ZnCo₂O₄ nanosheet materials, 85-88 while flake-like ZnCo₂O₄ nanostructures on CC, 83 leaf-like ZnCo₂O₄ nanostructures on NF⁹² and Al_{0.5}Zn_{0.5}Co₂O₄ nanosheet arrays on NF⁸⁹ presented poor rate capabilities despite their high cycling stabilities. The trimetallic oxide-based electrode delivered slightly better performance than pristine ZnCo₂O₄ microurchin arrays on NF produced in the same work (approximately 1000 F g^{-1} at 20 A g^{-1}) due to the incorporation of a third metallic center that can enhance even further the ZnCo2O4 electrochemical behavior. The leaf-like ZnCo2O4 nanostructures on NF92 delivered high initial specific capacitance, due

to their high specific surface area and electroactive site availability, but limited morphology for fast ion-diffusion. The poor specific capacity of flake-like ZnCo₂O₄ nanostructures on CC⁸³ seems to be caused by their smooth surface and low specific surface area.

On the other hand, porous ZnCo₂O₄ nanoribbon arrays on NF⁸¹ (Fig. 4C) not only delivered the highest specific capacitance among binder-free 2D ZnCo₂O₄-modified electrodes, but also demonstrated a good rate capability of 61.7% upon a 20-fold current density increase. In this case, good cycling stability was noticed, maintaining 84% of the initial specific capacitance after 3000 cycles, attributed to the appropriately spaced and highly porous nanoribbon arrays, which provided multiple and facile channels for fast ion-diffusion.

Compared with 2D nanomaterials based on radial growth of nanosheets, i.e., micro-65,66 and nanoflowers,74 slurry-cast electrodes presented even better rate capability, high specific capacitance and cycling stability. Mesoporous ZnCo2O4 microflowers⁶⁶ (680 F g^{-1} at 1 A g^{-1}), porous ZnCo₂O₄ microflowers⁶⁵ (689 F g^{-1} at 1 A $g^{-1})$ and porous $\rm Zn_{1.5}Co_{1.5}O_{4-\delta}$ nanoflowers 74 $(763.32 \text{ F g}^{-1} \text{ at 1 A g}^{-1})$ (Fig. 4D) presented 89.4% (0.35 to 1 A g^{-1}), 81.3% (1 to 15 A g^{-1}) and 55.31% (1 to 30 A g^{-1}) capacitance retention, respectively.

Micro- and nanoflower NPs combine the benefits of strongly interconnected sheet-like structures with a highly porous and hierarchical structure. They also present high specific surface area, promoting reduced mechanical stress. This arises from the huge volumetric expansion during the charge/discharge processes, facilitating electrolyte penetration and ion diffusion into the electroactive material. There is a high availability of electroactive sites even at high current densities and numerous charge/discharge cycles. The binder-free electrode with radial growth of ZnCo₂O₄ nanoflowers on an NF electrode⁸² (Fig. 4E

and F) delivered 1657 F g⁻¹ at 1 A g⁻¹, and was designed along with a flake-like ZnCo₂O₄-modified NF electrode, which delivered 1803 F g^{-1} at 1 A g^{-1} . They presented, respectively, $\sim 45\%$ and $\sim 33.3\%$ rate capability at 16 A g⁻¹, which makes ZnCo₂O₄ nanoflowers on the NF electrode a better candidate for supercapacitive applications even though they still present low specific capacitance retention at higher current densities. Presumably, nanoflower structures are more stable under high current conditions and repeated charge/discharge cycles. The abundance of ion-diffusion channels can improve the electrolyte and electron transport. However, it is still very limited, and the parallelly grown structures can be more suitable for binderfree electrodes in comparison to those radially grown.

There are also some recent works about pristine 1D structured ZnCo₂O₄. These structures can have some advantages, exhibiting optimal specific surface area and material mass ratios which are only surpassed by typical 0D materials, such as quantum-dots. In this case, it is important to mention their extremely reduced length in two dimensions, shorter ion diffusion lengths and facile electrical transport exclusively in the axial direction. Also relevant are the quantum confinement effects, altering the material properties in such a way that photons can be absorbed at one wavelength and transmitted at another. 97 These advantages can be further enhanced in slurrycast electrodes by producing hollow nanotubes (362 F g⁻¹ at 0.5 A g^{-1})⁷⁷ (Fig. 5A), with low density, superior specific surface area and shorter ion transport path. Alternatively, urchin-like microspheres (677 F g^{-1} at 1 A g^{-1})⁶⁴ (Fig. 5B) with radially grown porous nanorods have almost the same benefits of porous microflowers, both with high rate capability and capacitance retention through cycling for slurry-cast electrodes.

Binder-free electrodes, ZnCo₂O₄ nanorods/CC (5.18 F cm⁻² at 5 mA cm⁻²), ⁷⁸ nanorods/flexible stainless-steel mesh (FSSM)

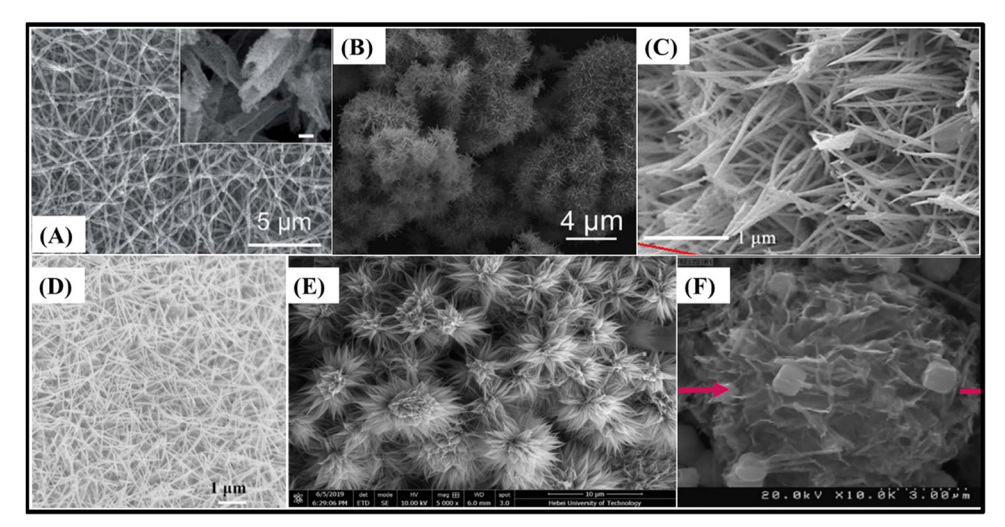


Fig. 5 SEM images of (A) hollow $ZnCo_2O_4$ nanotubes, ⁷⁷ (B) urchin-like $ZnCo_2O_4$ microspheres, ⁶⁴ (C) $ZnCo_2O_4$ nanorods/CC, ⁷⁸ (D) $ZnCo_2O_4$ nanowire arrays/NF, ⁹⁶ (E) porous $ZnCo_2O_4$ micro-urchins/NF ⁹¹ and (F) $ZnCo_2O_4$ intertwined heterostructured nanocubes/NF. ⁹³ Panel A: Reproduced with permission.⁷⁷ Attribution 3.0 Unported (CC BY 3.0), Royal Society of Chemistry. Panel B: Reproduced with permission.⁶⁴ Copyright © 2018 Elsevier Ltd and Techna Group S.r.l. All rights reserved. Panel C: Reproduced with permission. 78 Copyright © 2018 Elsevier B.V. All rights reserved. Panel D: Reproduced with permission. 96 Panel E: Reproduced with permission. 91 Copyright © 2019, Springer-Verlag GmbH Germany, part of Springer Nature. Panel F: Reproduced with permission. 93 Copyright © 2019 Korean Physical Society. Published by Elsevier B.V. All rights reserved.

(315 F g⁻¹ at 2 A g⁻¹), ⁷⁹ nanowires (2049 F g⁻¹ at 2 A cm⁻²), ⁶⁵ micro-urchins/FSSM (127.8 F g⁻¹ at 1 mA cm⁻²), 94 microurchins/NF (390 F g⁻¹ at 1 A g⁻¹), 95 and two porous ZnCo₂O₄ micro-urchins on NF electrodes (1000 F g⁻¹ at 20 A g⁻¹;⁸⁹ 1527.2 F $\rm g^{-1}$ at 1 A $\rm g^{-1\,91}$) were also assembled. The ZnCo₂O₄ nano-rod arrays on CC⁷⁸ (Fig. 5C) presented one of the highest rate capabilities based on 1D-morphology, with 59.8% capacitance retention and a 20-fold current density increase, along with a good areal capacitance. The other nanorod-modified electrode, ZnCo₂O₄ nano-rod arrays on FSSM,⁷⁹ delivered not only low specific capacitance but also good rate-capability. This is attributed to the uniform thickness, length, and parallel oriented distribution of ZnCo₂O₄ nanorods with suitable spaces between them, allowing rapid ion-diffusion and active site availability. Nanowire arrays of ZnCo₂O₄ on NF⁹⁶ (Fig. 5D) share almost the same properties of nanorod-modified electrodes, but instead they deliver one of the highest specific capacitances and rate-capabilities among all pristine 1D ZnCo₂O₄-modified binder-free electrodes, with 83.6% capacitance retention after a 15-fold increase in current density. They also exhibit the unusually high cycling stability observed for binder-free electrodes (88.8%, 3000 cycles). This superior performance is inferred to be caused by the higher length of the nanowires in comparison to nanorods. As a result, an interconnective mesoporous structure with very high specific area, abundant available electroactive sites, and shortened distances of electron transportation is obtained. There are also suitable spaces between nanowires for allowing fast and effective ion-diffusion.

Interestingly, two of the reported micro-urchin architectures deliver relatively low specific capacitances for a binder-free ZnCo₂O₄-based electrode, ^{94,95} although much higher than those of slurry-cast micro-urchin electrodes produced by a similar synthesis route. 95 Porous ZnCo₂O₄ micro-urchins on NF electrodes89,91 deliver good specific capacitances, due to their larger spatial and porous structure (Fig. 5E), which greatly improves electroactive site availability and promotes better charge transport and ion-diffusion. However, all these mentioned materials presented limited rate-capability as 2D-morphologybased microflowers, due to the lack of parallel orientation. There is no adequate space between the nanostructures for optimizing the electrolyte penetration. Additionally, by combining 1D and 2D features in cubic structures, ZnCo2O4 intertwined heterostructured nanocubes on an NF electrode⁹³ (Fig. 5F) were produced. They encompass mixed nanowires and nanosheets directly grown onto NF, with connective channels for electron transfer and suitable pores facilitating rapid ion-diffusion. This results in a high specific capacitance, e.g., 2040 F g⁻¹, at a high current density of 20 A g^{-1} .

3.1.2. ZnCo₂O₄/transition metal-based material composite electrodes. Although pristine ZnCo₂O₄-based electrodes presented relatively good performance due to the increase in supercapacitive performance by morphology design, another strategy to improve their electrochemical performance is by increasing the electroactive site abundancy and the specific surface area, combining ZnCo2O4 with other TMOs materials, such as MnO₂, 98 ZnO, 99-102 MnCo₂O₄, 103 NiCo₂O₄ 104-106 and

Ni₃V₂O₈¹⁰⁷ for slurry-cast electrodes (Table 3) or MnO₂, ^{108,109} ZnO, 110 NiO, 111 Co₃S₄, 112 ZnCo₂S₄ 113 and Zn-Co-S¹¹⁴ for binderfree electrodes (Table 4). These heterojunction-structured materials are composed of a base material that can provide better conductivity for charge and electron transfer and another material that can provide more active sites. 103 Following a similar strategy, great attention has been directed to core@shell architectures in binderfree electrodes, with ZnCo₂O₄ acting principally as the core material, due to its high electrical conductivity and facile morphological design using MnO_2 , 58,115 CdS, 116 Ni $_3$ S $_2$, 117 Ni–Co–S, 118 ZnCo $_2$ S $_4$, 113 Zn–Co–S, 114 NiMoO $_4$, $^{199-121}$ CoMoO $_4$, 122 ZnWO $_4$, 123 NiWO $_4$, 124 Ni(OH)₂, ^{125,126} and Co-Al LDH¹²⁷ as shell materials, and Co₃O₄ as a core material 128 (Table 5).

MnO2 has been considered to be an ideal electrode active material owing to its superior electrochemical activity and high theoretical capacitance (about 1370 F g⁻¹); however, its poor conductivity still precludes practical application in highperformance energy storage devices. Nevertheless, the addition of MnO2 NPs and nanostructures onto more conductive materials, such as ZnCo₂O₄, can further enhance the electrochemical performance of nanocomposite-based electrodes. As a result, a MnO2 NP-decorated ultrathin ZnCo2O4 nanosheet slurry-cast electrode (286 F g⁻¹ at 1 A g⁻¹)⁹⁸ presents more electroactive sites and specific surface area in comparison to pristine ZnCo₂O₄. Consequently, it provides better transmission channels for electrons due to the superior electrical conduction and suitable morphology of ZnCo2O4 support, while the appropriate content of MnO₂ NPs further improves its electrochemical properties, acting as a highly active cocatalyst. Similarly, concerning binder-free electrodes, porous ZnCo₂O₄ nanoflakes of interconnected NPs, with sufficient space to serve as the backbone for the growth of MnO2 nanosheets, were used to produce a ZnCo2O4/MnO2 heterostructure on NF¹⁰⁸ (Fig. 6A). This drastically increased the availability of electroactive sites and specific surface area, but maintained the space needed for electrolyte diffusion at higher current densities. This new structure was able to deliver 2057 F g^{-1} at 1 A g^{-1} with a cycling stability of 96.5% after 5000 cycles and a rate capability of 65% after a 15-fold current density increase.

In fact, heterostructured nanosheet architectures are among the best for ZnCo₂O₄ composite-based binder-free electrodes due to their electrochemical stability, large specific surface area and optimal space between the nanosheets, which maximizes the availability of electroactive sites even at high current density. Therefore, ZnCo₂O₄@MnO₂ hierarchical nanosheet arrays on NF (2170 F g^{-1} at 3 mA cm⁻²),⁵⁸ based on the growth of MnO2 nanosheets onto porous ultrathin ZnCo2O4 nanosheets, delivered a high specific capacitance similarly to the ZnCo₂O₄/MnO₂ heterostructure on NF. 108 The capacitance retention was 117.5% after 2500 charge/discharge cycles, and the rate capability was 50.4% at 40 mA cm⁻², due to the slow diffusion of electrolyte between the spaces of abundant MnO₂ nanosheets. Moreover, such core@shell materials were also studied in 1D morphology as ZnCo2O4@MnO2 nanowire arrays on NF (4.98 F cm⁻² at 2 mA cm⁻²)¹¹⁵ (Fig. 6B), encompassing

129 97 99 100 130 131 132 134 136 103 Ref. 105 133 106 102 135 107 101 104 86 Relevant electrochemical parameters of Zn_xCo_{2-x}O₄-based composite materials for slurry-cast electrodes and their performance in supercapacitive energy storage devices assembled with — Symmetric Symmetric AC Symmetric Symmetric Negative electrode material in SCs rGO AC AC ACACAC I $^{\mathsf{AC}}$ $^{\mathsf{AC}}$ AC 7987.5 at $\sim 21 \text{ W h kg}^{-1}$ at 11.3 W h kg^{-1} 7494 at 15.4 W h kg⁻¹ h kg⁻¹ 7909 at 75 W h kg⁻¹ 2121 at 31 W h kg⁻¹ 4540 at 7 W h kg⁻¹ 6040 at 17 W h kg⁻¹ 3880 mW cm^{-3} at 8.3 mW h cm⁻³ density $(\bar{W} \text{ kg}^{-1})$ 15 500 at 11 W Highest power 7500 46.04 at 799.99 W kg⁻⁻ $16.94 \text{ at } 750 \text{ W kg}^{-1}$ 101.6 at 1600 W kg $24.46~{
m at}~750~{
m W~kg}^{-1}$ $47.8 \text{ at } 800 \text{ W kg}^{-1}$ 83.11 at 800 W kg – 19.5 at 750 W kg⁻¹ density (W h $\widetilde{k}g^{-1}$) 39 at 1478 W kg⁻¹ kg^{-1} 62 at 720 W kg^{-1} 71 at 980 W kg^{-1} 31.8 mW h cm $^{-3}$ at 280 mW cm $^{-3}$ Highest energy 90 at 812 W Stability retention/cycle $\sim 96.4\%/10000$ 87%/3000 125%/1000 $\sim 90\%/2500$ 91%/10000 93.8%/5000 86.5%/5000 68.7%/5000 88.1%/2000 98.9%/1000 0008/%96 89%/1500 66%/2000 97%/2000 90%/2500 numbers Rate capability/ current density 18.3%/0.25-15 $\sim 31.2\%/1-30$ 56.6%/1-20 27.5%/0.5-8 90.6%/1-10 58.4%/1-20 69.6%/1-15 64.1%/1-10 89.4%/0.3-1 61.5%/1-1058.2%/1-20 \sim 66%/4-8 64%/0.5-4 73%/1-10 76.6%/1-3 90%/1-10 range 0-0.625/Ag/AgCl 0-0.55/Hg/HgO 0-0.55/Hg/HgO 0-0.45/Ag/AgCl 0-0.4/Ag/AgCl 0-0.5/Hg/HgO 0-0.5/Hg/HgO 0-0.5/Ag/AgCl 0-0.4/Ag/AgCl 0-0.4/Ag/AgCl 0-0.45/SCE 0-0.4/SCE 0-0.5/SCE 0-0.5/SCE 0-0.4/SCE 0-0.5/SCE 0-0.5/SCE Potential electrode window V)/ref. 1386 F g⁻¹ (154 mA h g⁻¹) at 4 A g⁻¹ 867 F g⁻¹ at 0.5 A g⁻¹ 254 F g⁻¹ at 1 A g⁻¹ 1870.9 F g^{-1} (1029 C g^{-1}) at 1 A g^{-1} 1203.8 F g^{-1} at 1 A g^{-1} 327.5 F g^{-1} at 0.5 A g^{-1} 826.7 F g^{-1} (372 C g^{-1}) at 1 A g^{-1} 1734 F g^{-1} at 1 A g^{-1} 705.1 F g^{-1} at 0.3 A g⁻¹ 2176.4 F g⁻¹ (1197 C g⁻¹) at 1 A g⁻¹ 64 mA h g⁻¹ at 1 A g⁻¹ 593.6 F g⁻¹ at 0.25 A g⁻ 720 F g⁻¹ at 1.5 A g⁻¹ 1581.5 F g⁻¹ at 1 A g⁻¹ 1892.5 F ${
m g}^{-1}$ at 1 A ${
m g}^{-1}$ 1136.4 F ${
m g}^{-1}$ at 1 A ${
m g}^{-1}$ $286 \text{ F g}^{-1} \text{ at 1 A g}^{-1}$ Specific capacitance or specific capacity at 25 mA $\rm cm^{-2}$ 54.1 mA h g^{-1} ZnCo₂O₄/rGO ultrathin nanosheets Cauliflower-like AuNP/rGO-ZnCo₂O₄ $NiCo_2O_4/ZnCo_2O_4$ heterostructure Nanosheet-like ZnCo₂O₄/N-GO/PANI Hydrangea-like ZnCo₂O₄/Ni₃V₂O₈ N-doped C supported P-ZnCo₂O₄ Porous NiCo₂O₄/ZnCo₂O₄/Co₃O₄ Nanosheet-like g-C₃N₄/ZnCo₂O₄ CNP/ZnO/ZnCo₂O₄ nanosheets Nanosheet-based hollow ZnO/ Snowflake-like ZnCo₂O₄/ZnO MWCNT/ZnCo2O4 hexagonal PANI/ZnCo₂O₄ nanoparticles Marigold-like ZnO/ZnCo₂O₄ ZnCo₂O₄/NiO microspheres Heterostructured NiCo₂O₄-ZnCo₂O₄/CNT nanoflowers neterojunction nanosheets ZnCo₂O₄/rGO nanosheets Ultrathin ZnCo₂O₄/MnO₂ suitable cathode material ZnCo₂O₄/C nanofibers $ZnCo_2O_4/MnCo_2O_4$ Electrode material hollow nanocages nanosheets Table 3

This article is licensed under a Creative Commons Attribution-NonCommercial 3.0 Unported Licence.

suitable cathode material								
Electrode material	Specific capacitance or specific capacity	Potential window (V)/ref. electrode	Rate capability/ current density range	Stability retention/cycle numbers	Highest energy density (W h kg ⁻¹)	Highest power density (W kg^{-1})	Negative electrode material in SCs	Ref.
Mesoporous ZnCo ₂ O ₄ /NiO	$2797 \text{ F g}^{-1} \text{ at 1 A g}^{-1}$	0-0.5/SCE	81.8%/1-10	$\sim 100\%/3000$	ı	ı	1	111
Porous $ZnCo_2O_4/MnO_2$	2057 F g^{-1} at 1 A g^{-1}	0-0.4/SCE	65%/1–15	96.5%/5000	69 at 400 W kg^{-1}	$4900 \text{ at } 21.7 \text{ W h kg}^{-1}$	AC/NF	108
ZnCo ₂ O ₄ /rGO intertwined sheets on NF	$3222 \mathrm{~Fg^{-1}}$ at $1\mathrm{~Ag^{-1}}$	0-0.5/HgO/Hg	26.7%/1-20	65%/5000	49.1 at $\sim 600 \text{ W kg}^{-1}$	$7625 \text{ at } 18.8 \text{ W h kg}^{-1}$	AC	137
hollow vs on CT	$\sim 2003.8 \text{ F g}^{-1}$	0.05-0.45/Ag/AgCl	74.7%/	$\sim\!99.4\%/10000$	$2.32 \text{ mW h cm}^{-3}$	166.7 mW cm ⁻³	${ m Fe_3O_4}/{ m r-GO//CT}$	138
_	1075.4 F g ⁻¹ at 1 A g ⁻¹	0-0.4		89.3%/10 000				139
ianieuar minis 3D flower-like ZnCo ₂ O ₄ /PVP NC ZnCo ₂ O ₄ honey	761 F g ⁻¹ at 0.35 A g ⁻¹ 1289 F g ⁻¹ at 3.5 A g ⁻¹	0-0.4/Ag/AgCl 0.2-0.45/Ag/AgCl	\sim 89.4%/0.35-1 70%/3.5-20	90%/2000 86%/2000	— 41.9 at 1065.1 W kg ⁻¹	\sim 14 900 at \sim 29 W h kg ⁻¹	AC/CC	66 140
nest nanostructures Heterostructured	$1600 \text{ F g}^{-1} \text{ at 1 A g}^{-1}$	-0.2 to 0.4/SCE	78.1%/1-30	I	66.1 at 701 W ${ m kg}^{-1}$	$7016 \text{ at } 43.66 \text{ W h kg}^{-1}$	AC	141
MnO ₂ -decorated ZnCo ₂ O ₄ manochaete on rCO ₂ dened NE	$3405.2 \; \mathrm{F \; g^{-1}} \; \mathrm{at} \; 2 \; \mathrm{A} \; \mathrm{g^{-1}}$	0-0.5/SCE	64.9%/2-20	91.2%/5000	$46.85 \text{ at } 166.67 \text{ W kg}^{-1}$	$1666.67 \text{ at } 17.13 \text{ W h kg}^{-1}$	rGO/NF	109
ZnCo ₂ O ₄ /Co ₃ S ₄ nanowires	$2.02~\mathrm{C~g}^{-1}$ at $0.8~\mathrm{A~g}^{-1}$	I	I	95.3%/6000	$0.0798 \text{ at } 1795 \text{ W kg}^{-1}$	$9760 \text{ at } 0.0732 \text{ W h kg}^{-1}$	I	112
Porous $ZnCo_2O_4$	680 F g^{-1} at 1 A g^{-1}	$0-0.45/\mathrm{Hg/HgO}$	88%/1–5	95.6%/3000	$31.25 \text{ at } 375 \text{ W kg}^{-1}$	$3750 \text{ at } 11.46 \text{ W h kg}^{-1}$	AC	142
$ZnCo_2O_4/ZnO$ heterostructured nanorods on ITO	150 $\mu F cm^{-2}$ at 1.2 $\mu A cm^{-2}$ (UV-radiation)	0-0.6/symmetric SC	174%/off-on (UV)	I	11.8 $10^{-3} \mu \text{W h cm}^{-2}$ at 1.2 $\mu \text{A cm}^{-2} \left(\text{UV} \right)$	I	Symmetric	110

This article is licensed under a Creative Commons Attribution-NonCommercial 3.0 Unported Licence. Open Access Article. Published on 03 októbra 2022. Downloaded on 9.12.2025 11:08:47.

Table 5 Relevant electrochemical parameters of $Zn_xCo_{3-x}O_4$ -based core@shell composite materials for binder-free electrodes and their performance in supercapacitive energy storage devices assembled with a suitable cathode material

Electrode material	Specific capacitance or specific capacity	Potential window (V)/ref. electrode	Rate capability/ current density range	Stability retention/cycle numbers	Stability retention/cycle Highest energy density numbers $(W \text{ h kg}^{-1})$	Highest power density (W ${\rm kg}^{-1}$)	Negative electrode material in SCs	Ref.
ZnCo ₂ O ₄ @MnO ₂ nanowires on NF	$4.98~\mathrm{F~cm^{-2}}$ at 2 mA cm $^{-2}$	0-0.45/SCE	~78.9%/2-16	106.2%/10 000	$0.058 \text{ mW h cm}^{-3}$ at 7150 W cm $^{-3}$	I	AC	115
ZnCo ₂ O ₄ @Ni ₃ S ₂ heterostructured	$2200 \; \mathrm{F} \; \mathrm{g}^{-1} \; \mathrm{at} \; 2 \; \mathrm{A} \; \mathrm{g}^{-1}$	0-0.4/Ag/AgCl	55.7%/2-10	88.9%/1000		I	I	1117
ZnCo ₂ O ₄ @NiMoO ₄ heterostructured	2316 F g^{-1} (1158 C g^{-1})	0-0.5/SCE	75.3%/3-40	103.4%/5000	$25.3~\mathrm{at}~787.9~\mathrm{W~kg}^{-1}$	$9467.5 \text{ at } 18.4 \text{ W h kg}^{-1}$	AC	119
$ZDCo_2O_4$ (a) NIMOO4 heterostructured nanowires on NF		$0-0.5/\mathrm{Ag/AgCl}$	55%/1-20	I	$57.5 \text{ at } 900 \text{ W kg}^{-1}$	$18000~at~30~W~h~kg^{-1}$	CNT/NF	120
$ZnCo_2O_4$ $ZnWO_4$ heterostructured nanowires on NF	13.4 F cm $^{-2}$ at 4 mA cm $^{-2}$	$0-0.4/\mathrm{Ag/AgCl}$	28.1%/4-64	98.5%/5000	$24~\mathrm{at}~400~\mathrm{W~kg}^{-1}$	2001.07 at 16.68 W h ${\rm kg}^{-1}$	AC	123
) ₄	2192.2 F g^{-1} (1096.1 C g^{-1}) at 10 mA cm ⁻²	0-0.5/SCE	73.8%/3-40	104.1%/5000	$29.24 \ {\rm at} \ 884.57 \ {\rm W} \ {\rm kg}^{-1}$	$10526.32~{\rm at}~20.76~{\rm W}~h~{\rm kg}^{-1}$	AC	122
$(OH)_2$	1901.6 F g^{-1} (237.7 mA h g^{-1})	0-0.45/Ag/AgCl	85.7%/2-20	98.7%/5000	$80.10 \ at \ 662.06 \ W \ kg^{-1}$	$9200 \text{ at } 64.75 \text{ W h kg}^{-1}$	Fe_2O_3/NF 125	125
.0	1 1762.6 F g^{-1} at 1 A g^{-1}	0-0.5/Hg/HgO	81.3%/1-50	81.4%/5000	$37.1~\mathrm{at}~433.1~\mathrm{W~kg}^{-1}$	5124.3 at 28.3 W h ${\rm kg}^{-1}$	AC	118
$ZnCo_2O_4$ ($@Co-Al\ LDH$	$2041 \; \mathrm{F} \; \mathrm{g}^{-1} \; \mathrm{at} \; 1 \; \mathrm{A} \; \mathrm{g}^{-1}$	0-0.5/SCE	70%/1-10	I	$50.1 \text{ at } 400 \text{ W kg}^{-1}$	$6200 \text{ at } 16.53 \text{ W h kg}^{-1}$	AC	127
O_4 · H_2 O	$3.53 \mathrm{\ Fcm}^{-2} \mathrm{\ at\ 1\ mA\ cm}^{-2}$	$0-0.5/\mathrm{Ag/AgCl}$	I	95.4%/5000	2.55 mW h cm ⁻³	0.169 W cm^{-3}	CNT	121
뇬	$^{2340} \text{ F g}^{-1} (7.02 \text{ F cm}^{-2})$	0-0.5/Hg/HgO	$\sim 57\%/1-20$	92.6%/10000	35.75 at 73.17 W kg ⁻¹	$\sim 1900 \text{ at } \sim 4.5 \text{ W h kg}^{-1}$	AC	143
$Ni(OH)_2$	1021.1 F g^{-1} (3.06 F cm ⁻²)	0-0.5/SCE	55.3%/1-10	50.1%/5000	$40.0~{\rm at}~802.7~{\rm W~kg}^{-1}$	$8020 \text{ at } 17.6 \text{ W h kg}^{-1}$	AC	126
	at 1 mA cm 1210 F ${ m g}_{1}^{-1}$ (605 C ${ m g}^{-1}$)	0-0.5/Ag/AgCl	56%/1-10	93.5%/9000	$141.3 \text{ at } 2700.5 \text{ W kg}^{-1}$	$\sim 27000 \text{ at } \sim 90 \text{ W h kg}^{-1}$	AC	57
	at 1 A $\rm g^{-1}$ 1782 F $\rm g^{-1}$ (2.14 F cm ⁻²)	0-0.5/Hg/HgO	35.5%/1-10	95.4%/5000	$42.2 \text{ at } 716 \text{ W kg}^{-1}$	$3087 \text{ at } 34.3 \text{ W h kg}^{-1}$	AC	124
heterostructures on NF ZnCo ₂ O ₄ @MnO ₂ hierarchical	at 1 mA cm $^{-2}$ 2170 F g $^{-1}$ (2.6 F cm $^{-2}$)	0-0.5/SCE	50.4%/3-40	117.5% 2500	$29.41 \text{ at } 628.42 \text{ W kg}^{-1}$	8378.38 at 6.98 W h kg ⁻¹	AC	58
	at 3 mA cm $^{-2}$ 2507.0 F g $^{-1}$ (3.75 F cm $^{-2}$)	0-0.5/Hg/HgO	~69%/0.5-20	83.2%/5000	$44.15 \text{ at } 850 \text{ W kg}^{-1}$	4250 at 33.06 W h kg ⁻¹	AC	144
NiCo ₂ O ₄ @PPy on NF ZnCo ₂ O ₄ @CdS nanoflowers on NF	at 0.5 A g^{-1} 5.91 F cm ⁻² (2.66 C cm ⁻²)	0-0.45/SCE	62.2%/25-40	I	I	1	I	116
Mesoporous Co_3O_4 \otimes $ZnCo_2O_4$	at 25 mA 2255.5 F g^{-1} (1240.5 C g^{-1}) at 2 mA gm^{-2}	0-0.55/Hg/HgO	59.0%/2-30	90.9%/3000	37.3 at 800 W kg^{-1}	$8000 \text{ at } 21.3 \text{ W h kg}^{-1}$	AC	128
Flower-like ZnCo ₂ O ₄ @ZnCo ₂ S ₄	4 L 2 IIIA 2 L $^{-1}$ at 1 A 2 L	SCE	54.6%/1-10	I	127.4 at 2520 W ${ m kg}^{-1}$	36497.16 at 40.55 W h ${\rm kg}^{-1}$	CNTs	113
nanostructures on Nr ZnCo ₂ O ₄ @Zn–Co–S hybrid nanowires on CNTFs	\sim 1.35 F cm $^{-2}$ at 0.5 mA cm $^{-2}$	-0.1 to 0.6/SCE	I	I	32.01 μ W h cm ⁻² at 698.42 μ W cm ⁻²	6999.99 $\mu W \text{ cm}^{-2}$ at 12.38 $\mu W \text{ h cm}^{-2}$	H-Co ₃ O ₄ / CoNC/ CNTFS	113

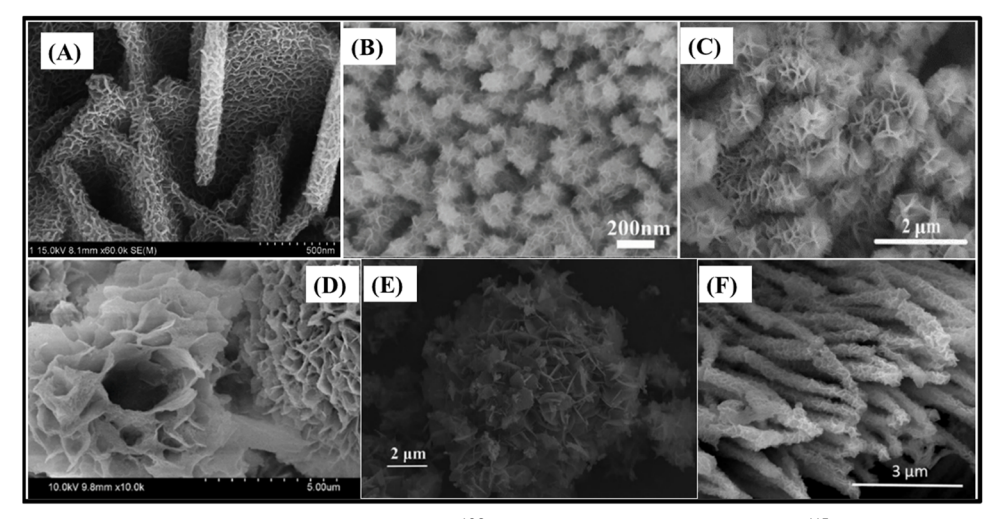


Fig. 6 SEM images of (A) porous ZnCo₂O₄/MnO₂ heterostructures/NF, ¹⁰⁸ (B) ZnCo₂O₄@MnO₂ nanowires/NF, ¹¹⁵ (C) mesoporous ZnCo₂O₄/NiO flowerlike clusters/NF, 111 (D) ZnCo₂O₄@CdS nanoflowers/NF, 116 (E) hydrangea-like ZnCo₂O₄/Ni₃V₂O₈ nanostructures/NF 107 and (F) ZnCo₂O₄@Ni₃S₂ heterostructured nanowires/NF.¹¹⁷ Panel A: Reproduced with permission.¹⁰⁸ Copyright © 2018 Elsevier Ltd. All rights reserved. Panel B: Reproduced with permission. 115 Copyright MarketplaceTM, Royal Society of Chemistry. Panel C: Reproduced with permission. 111 Copyright © 2018 Elsevier Ltd. All rights reserved. Panel D: Reproduced with permission. 116 Copyright © 2020 Korean Physical Society. Published by Elsevier B.V. All rights reserved. Panel E: Reproduced with permission. 107 Copyright © 2019 Elsevier Ltd and Techna Group S.r.l. All rights reserved. Panel F: Reproduced with permission. 117 Copyright © 2017 Elsevier B.V. All rights reserved

smooth ZnCo₂O₄ nanowires uniformly covered with a porous MnO₂ thin film. This largely increased the specific surface area of the electrode, delivering 5 times more specific capacitance than that of pristine ZnCo₂O₄ nanowires, in addition to exhibiting much better cycling stability (106.2% vs. 87.7% after 10 000 cycles) and rate capability (\sim 78.9% vs. 57.4% at 16 mA cm⁻²).

Binder-free electrodes were studied in recent years, using the same strategy of designing decorated nanocomposites, ZnCo₂O₄/Co₃S₄ nanowire arrays on NF (2.02 C g⁻¹ at 0.8 A g⁻¹)¹¹² and mesoporous ZnCo₂O₄/NiO flower-like clusters on NF (2797 F g^{-1} at 1 A g^{-1}), 111 as well as slurry-cast electrodes and ZnCo₂O₄@CdS nanoflowers on NF (5.91 F cm⁻² at 25 mA). 116 Mesoporous ZnCo₂O₄/NiO flower-like clusters on NF¹¹¹ (Fig. 6C) make use of highly electroactive NiO nanosheets, with a theoretical specific capacitance of 3750 F g^{-1} , assembled onto ZnCo₂O₄ microspheres. In this case, the NiO nanosheets form flower-like clusters, and relieve the internal stress and restrain the capacitance decay through the chargedischarge processes. In addition, they help in reducing the ion-diffusion path length and increasing the specific surface area. As a result, very high specific capacitance and overall stability are achieved, with a retention of 81.8% upon a 10-fold current density increase and ~100% after 3000 cycles. CdS is another highly electroactive semiconductor candidate for supercapacitive applications due to its excellent conductivity and high theoretical capacity of 1675 F g^{-1} . Therefore, it is assembled with CdS nanoparticles as the coating shell and ZnCo₂O₄ nanoflowers as the core (Fig. 6D), ¹¹⁶ delivering more than 10 times the specific capacitance of pristine ZnCo₂O₄ nanoflowers. There is a low rate capability, mainly due to the intrinsically low electrolyte diffusion at higher current densities for the flower-like structured binder-free electrode, and

also some limitation of ion-diffusion through the CdS nanoparticle shell.

In addition, Ni₃V₂O₈ and Ni₃S₂ have also been used for supercapacitive applications owing to their high performance and capacity. In fact, slurry-cast hydrangea-like ZnCo₂O₄/ Ni₃V₂O₈ nanostructures composed of ZnCo₂O₄ nanospheres and Ni₃V₂O₈ nanosheets¹⁰⁷ (Fig. 6E) present nanoflower-like heterostructures that can provide open space for ion-diffusion pathways, exposing various redox active sites for electrochemical reactions and electron transport, delivering 1734 F g⁻¹ at 1 A g⁻¹. It also presents superior cycling stability and rate capability, retaining 96% of its initial specific capacitance after 8000 cycles and 90% from 1 to 10 A g^{-1} . The binder-free core@shell ZnCo₂O₄@Ni₃S₂//NF electrode (2200 F g⁻¹ at 2 A g^{-1})¹¹⁷ (Fig. 6F) exhibits interconnected Ni₃S₂ nanosheets coated on the surfaces of the highly ordered and dense ZnCo₂O₄ nanowire arrays. It delivered high specific capacitance because of the two-dimensional (2D) nanosheet coating, which largely increases the specific surface area. However, 55.7% rate capability at 5-fold current density is due to the reduced space between nanowires that limits the electrolyte diffusion at higher current densities.

Zinc oxide (ZnO), an n-type semiconductor with a wide band gap (~ 3.37 eV), can synergize well with $ZnCo_2O_4$, a p-type semiconductor, to produce ZnCo₂O₄/ZnO heterostructures with p-n junctions. The n-type region has a high electron concentration and the p-type, a high hole concentration; so electrons diffuse from the n-type side to the p-type side. Therefore, the electrons generated at ZnO sites in charge/discharge cycles can rapidly diffuse into the ZnCo₂O₄ matrix, potentially enhancing the overall electronic conduction of the composite. All ZnCo₂O₄/ ZnO composites used in slurry-cast electrodes found in the

(C) ZnO l um ZnCo,O4/NiO **(F)**

 $\label{eq:Fig.7} \textbf{Fig. 7} \hspace{0.2cm} \textbf{(A)} \hspace{0.2cm} \textbf{SEM} \hspace{0.2cm} \textbf{image} \hspace{0.2cm} \textbf{of} \hspace{0.2cm} \textbf{snowflake-like} \hspace{0.2cm} \textbf{ZnCo}_2O_4/\textbf{ZnO} \hspace{0.2cm} \textbf{microstructures.} \\ \textbf{99} \hspace{0.2cm} \textbf{(B)} \hspace{0.2cm} \textbf{TEM} \hspace{0.2cm} \textbf{image} \hspace{0.2cm} \textbf{of} \hspace{0.2cm} \textbf{nanosheet-based} \hspace{0.2cm} \textbf{hollow} \hspace{0.2cm} \textbf{ZnCo}_2O_4/\textbf{ZnCo}_2O_4/\textbf{NiO} \\ \textbf{microspheres,} \\ \textbf{102} \hspace{0.2cm} \textbf{and} \hspace{0.2cm} \textbf{SEM} \hspace{0.2cm} \textbf{images} \hspace{0.2cm} \textbf{of} \hspace{0.2cm} \textbf{(C)} \hspace{0.2cm} \textbf{ZnCo}_2O_4/\textbf{ZnO} \hspace{0.2cm} \textbf{heterostructured} \hspace{0.2cm} \textbf{nanorods/ITO,} \\ \textbf{110} \hspace{0.2cm} \textbf{(D)} \hspace{0.2cm} \textbf{porous} \hspace{0.2cm} \textbf{NiCo}_2O_4/\textbf{ZnCo}_2O_4/\textbf{Co}_3O_4 \hspace{0.2cm} \textbf{hollow} \\ \textbf{102} \hspace{0.2cm} \textbf{NiCo}_2O_4/\textbf{ZnC$ $nanocages, ^{105} \ (E) \ flower-like \ ZnCo_2O_4@ZnCo_2S_4 \ nanostructures/NF, ^{113} \ and \ (F) \ ZnCo_2O_4@Ni-Co-S \ nanosheet-based \ microspheres/NF, ^{118} \ Panel \ A: \ Another \ Anoth$ Reproduced with permission. 99 © 2019 Elsevier Ltd and Techna Group S.r.l. All rights reserved. Panel B: Reproduced with permission. 102 Copyright MarketplaceTM, Royal Society of Chemistry. Panel C: Reproduced with permission. 110 Copyright © 2018 American Chemical Society. Panel D: Reproduced with permission. 105 Copyright © 2018 Elsevier B.V. All rights reserved. Panel E: Reproduced with permission. 113 Copyright © 2020, Springer Science Business Media, LLC, part of Springer Nature. Panel F: Reproduced with permission. 118 Copyright © 2020 Elsevier B.V. All rights reserved

literature presented very high specific surface area, due to radially grown structures such as snowflake-like ZnCo₂O₄/ZnO (826.7 F g⁻¹ at 1 A g⁻¹)⁹⁹ and marigold-like ZnO/ZnCo₂O₄ (705.1 F g⁻¹ at 0.3 A g⁻¹),¹⁰¹ or hollow structures, such as nanosheet-based hollow ZnO/ZnCo₂O₄/NiO microspheres (1136.4 F g⁻¹ at 1 A g⁻¹). 102 Snowflake-like ZnCo₂O₄/ZnO microstructures⁹⁹ (Fig. 7A) presented superior performance not only in specific capacitance but also in rate capability. They delivered 69.6% of their initial capacitance after a 15-fold increase in current density, due to the more suitable open space for the ion-diffusion pathway in comparison to tight nanosheets in marigold-like ZnO/ZnCo₂O₄ (89.4%, 0.3-1 A g⁻¹).¹⁰¹

Hollow ZnO/ZnCo2O4/NiO microspheres102 are covered with numerous ultrathin nanosheets and decorated with tiny pores (Fig. 7B), which provide optimized specific surface area and access to plenty of electrolyte. Such characteristics are beneficial for the exposure of electroactive sites, buffering the effect of volume changes and promoting suitable channels to facilitate rapid ion/electron diffusion during the charge/ discharge processes. The result encompasses 86.5% capacitance retention after 5000 cycles and, due to the tiny pore sizes and spaces within the ultrathin nanosheets, rate capabilities of ~31.2% and 54.9% with 30- and 10-fold current density increases, respectively. As for binder-free electrodes, there are ZnCo₂O₄/ZnO heterostructured nanorods on an ITO electrode (150 μF cm⁻² at 1.2 μA cm⁻² with UV-radiation)¹¹⁰ (Fig. 7C), which feature both the photoelectric effect and direct electron transportation pathway. Photoinduced electrons and holes, under UV radiation, participate directly in the electrolyte ion separation process to boost the overall capacitive response, thus delivering 174% (2.7 times) more specific capacitance under UV illumination as compared to the absence of UV.

Differently from the mentioned core@shell materials, the mesoporous Co₃O₄@ZnCo₂O₄/NF electrode (2255.5 F g⁻¹ at 2 mA cm⁻²)¹²⁸ features ZnCo₂O₄ as the shell material, due to its excellent rate capability and cycling stability. In this way it could improve the practical application of the electrode; even so, it has better electrical conductivity than its core. The directly grown needle-like Co₃O₄ nanowire arrays are composed of numerous polycrystalline interconnected nanoparticles, which provides good roughness, increasing the specific surface area and facilitating the uniform coating with the ZnCo₂O₄ thin film composed of multiple nanoparticles. As a result, the electrode delivers high specific capacitance, about 3-times more than that of Co₃O₄/NF, with a capacitance retention of 59.0% and 90.9% after a 15-fold current density increase and 3000 cycles, respectively.

Composites based on heterojunctions of ZnCo₂O₄ and other MCo₂O₄ usually present: (i) richer and more abundant redox reaction sites and, thus, higher specific capacitances; (ii) more stability, since both have high contents of Co₂O₄²⁻; and (iii) similar lattice parameters, in which the internal resistance of the adjacent interfaces is greatly reduced during the charge/ discharge processes and facilitates the electron transport. In this context, ZnCo₂O₄/MnCo₂O₄ heterojunction nanosheets $(254 \text{ F g}^{-1} \text{ at 1 A g}^{-1})^{103}$ and NiCo₂O₄/ZnCo₂O₄ heterostructures (1870.9 F g^{-1} at 1 A g^{-1})¹⁰⁴ composed of $ZnCo_2O_4$ nanosheets and urchin-like NiCo₂O₄, and porous NiCo₂O₄/ZnCo₂O₄/Co₃O₄ hollow nanocages (1892.5 F g^{-1} at 1 A g^{-1})¹⁰⁵ (Fig. 7D) formed by interconnecting ultra-small nanoparticles with many voids that results in porous multiple shells have been reported.

Despite delivering relatively low specific capacitance, slurry-cast ZnCo₂O₄/MnCo₂O₄ heterojunction nanosheet electrodes¹⁰³ presented higher specific capacitance and overall stability than pristine ZnCo₂O₄ and MnCo₂O₄. In fact, the other two composites also presented much better performance than their counterparts in slurry-cast electrodes NiCo₂O₄/Co₃O₄ and ZnCo₂O₄/ Co₃O₄, with NiCo₂O₄/ZnCo₂O₄/Co₃O₄ hollow nanocages, and urchin-like NiCo2O4 and sheet-like ZnCo2O4 for NiCo2O4/ ZnCo₂O₄ heterostructures. Notwithstanding, these NiCo₂O₄/ ZnCo₂O₄-based composites exhibit the second and third highest specific capacitances among all reported slurry-cast electrodes. They also show superior electrical conductivity, rich and abundant electrochemically active sites, high specific surface area, and good rate capability and cycling stability, 104,105 with a capacitance retention of 58.4% and 91% after a 20-fold current density increase and 10000 cycles, respectively.

Transition metal sulfides display higher electrical conductivity than their oxide counterparts because the replacement of oxygen with sulfur allows easier electron transport, lower electronegativity and smaller band-gaps, making them good candidates for supercapacitive applications and thus improving the energy storage properties of ZnCo₂O₄ in composite architectures. From this perspective, there are binder-free electrodes based on core@shell ZnCo₂O₄@Zn_xCo_{3-x}S₄ materials, such as those based on flower-like ZnCo₂O₄@ZnCo₂S₄ arrays//NF (1057.78 F g^{-1} at 1 A g^{-1})¹¹³ and ZnCo₂O₄@Zn-Co-S hybrid arrays//CNTFs ($\sim 1.35 \text{ F cm}^{-2}$ at 0.5 mA cm⁻²)¹¹⁴ and microsphere-structured ZnCo₂O₄@Ni-Co-S nanosheets (1762.6 F g⁻¹ at 1 A g⁻¹). The flower-like ZnCo₂O₄@ZnCo₂S₄//NF¹¹³ electrode (Fig. 7E) delivered good specific capacitance and, even so the hierarchical micro-nanostructured features could further improve the electrochemical properties of the electrode by offering larger spacing for the penetration of electrolyte into the structure. Thus, it could increase the availability of electroactive sites at higher current densities and electron transfer. A capacitance retention of 54.6% was achieved by a 10-fold increase in current density, as expected for a flower-like structure-based binder-free electrode.

Among bimetallic sulfides, nickel-cobalt sulfides have attracted a lot of attention due to their excellent conductivity, superior to nickel and cobalt sulfide counterparts and about 100 times higher than those of the corresponding oxides, and better capacitance performance compared with other metallic sulfides, such as NiS, Ni₃S₂, and CoS. In this context, slurry-cast core@shell ZnCo2O4@Ni-Co-S microspheres composed of radially grown ZnCo₂O₄ nanosheets, with a rough surface of electrodeposited Ni-Co-S¹¹⁸ (Fig. 7F), delivered higher specific capacitance, rate capability and cycling stability than their pristine ZnCo₂O₄ and Ni-Co-S counterparts. The increase of capacitance occurs mainly due to their hierarchical micronanostructure that has an open network of individual nanosheets. They facilitate ion-diffusion and help in maintaining the structural integrity. The highly conductive Ni-Co-S shell can efficiently decrease the charge transfer resistance, leading to a fast reversible redox reaction, ample redox active site availability and short ion diffusion pathways, thus resulting in a capacitance retention of 81.3% at a 50-fold increase in current density and 81.4% after 5000 cycles.

Notwithstanding, other materials have also attracted great attention as promising electrodes for energy storage devices, such as molybdenum- and tungsten-based metal oxides, nickel hydroxides and layered double hydroxides (LDHs). Core@shell structures along with ZnCo2O4 have been studied as shell materials, to achieve competitive supercapacitive performance. Molybdenum-based metal oxides such as NiMoO₄ ¹¹⁹⁻¹²¹ and CoMoO₄¹²² in core@shell architectures with ZnCo₂O₄ were studied, due to their high theoretical specific capacity attributed to Ni and Co ions, and excellent electrical conductivity, attributed to the multiple redox reactions of Mo ions. 119-122 All three reviewed core@shell ZnCo2O4@NiMoO4 materials had hierarchical nanowire and nanosheet architectures grown on NF, although with some differences that were relevant to their electrochemical performance, respectively: intercrossed ZnCo₂O₄ nanowires covered with NiMoO₄ nanosheets (2316 F g⁻¹ at 10 mA cm⁻²)¹¹⁹ (Fig. 8A); ZnCo₂O₄ nanowires covered with an ultrathin porous NiMoO₄ nanosheet network (1912 F g⁻¹ at 1 A g^{-1})¹²⁰ (Fig. 8B); and smooth reduced-ZnCo₂O₄ nanowires covered with NiMoO₄ nanosheets (3.53 F cm⁻² at 1 mA cm⁻²)¹²¹ (Fig. 8C). Comparing all three electrodes, the first one 119 not only had the best cycling stability and specific capacitance, but also presented hierarchical heterostructures for the nanowires with the smallest diameter, which facilitated ion-diffusion. The rate-capability was the best one, although it was still relatively low as a nanowire-based binder-free electrode. On the other hand, the core@shell ZnCo2O4@CoMoO4/NF electrode (2192.2 F g⁻¹ at 10 mA cm⁻²) presented smooth honeycomblike ZnCo2O4 nanosheets covered with interconnected rough CoMoO₄ nanosheets. In this way, it could effectively shorten the ion transport distance and increase the availability of electroactive sites, thus delivering high specific capacitance and excellent cycling stability, along with good rate-capability.

Tungsten-based metal oxides with wolframite structure, such as ${\rm ZnWO_4}^{123}$ and ${\rm NiWO_4},^{124}$ are promising materials for sensor, photocatalyst and energy storage systems. They allow supercapacitive applications, with high theoretical specific capacitance, where both Zn/Ni and W elements participate in the faradaic redox reactions and have high electrical conductivity. Core@shell ZnCo2O4@ZnWO4 (13.4 F cm-2 at 4 mA cm $^{-2}$) 123 (Fig. 8D) and ZnCo $_2$ O $_4$ @NiWO $_4$ (1782 F g $^{-1}$ and 2.14 F cm⁻² at 1 mA cm⁻²)¹²⁴ (Fig. 8E) present heterostructured ultrathin and interconnected nanosheet-covered nanowires on NF architecture. They can deliver high specific and areal capacitance, especially in the case of ZnCo2O4@ZnWO4 where the highly conductive ZnCo₂O₄ nanowire arrays rationally overcome the poor conductivity of ZnWO4 nanosheets which could shorten the ion-diffusion and electron transport pathways. Additionally, both electrodes present relatively poor rate-capability as nanowire-based binder-free electrodes, with a capacitance retention of 28.1% at 64 mA cm $^{-2}$ 123 and 35.5% 124 at 10 mA cm⁻², respectively.

Considering hydroxide-based shell materials, recent reports can be found in the literature for Ni(OH)₂^{125,126} and Co-Al

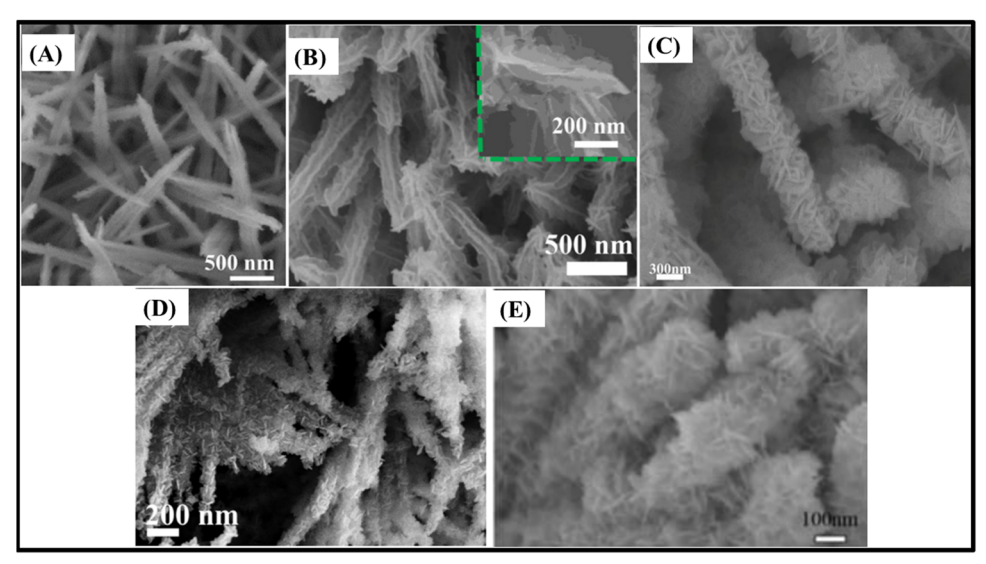


Fig. 8 SEM images of (A) ZnCo₂O₄@NiMoO₄ heterostructured nanowires/NF,¹²⁰ (B) ZnCo₂O₄@NiMoO₄ heterostructured nanowires/NF,¹²¹ (C) r-ZnCo₂O₄@NiMoO₄·H₂O heterostructured nanowires/NF,¹²¹ (D) ZnCo₂O₄@ZnWO₄ heterostructured nanowires/NF,¹²³ and (E) ZnCo₂O₄@NiWO₄ heterostructures/NF.¹²⁴ Panel A: Reproduced with permission.¹¹⁹ Copyright © 2020 Elsevier Ltd. All rights reserved. Panel B: Reproduced with permission.¹²⁰ Copyright © 2020 Elsevier Ltd. All rights reserved. Panel D: Reproduced with permission.¹²³ Copyright © 2018 Published by Elsevier Inc. Panel E: Reproduced with permission.¹²⁴ Copyright © 2020, Springer-Verlag GmbH Germany, part of Springer Nature.

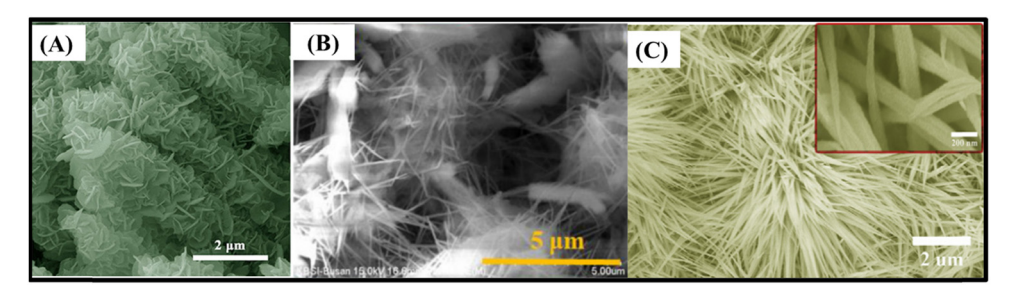


Fig. 9 SEM images of (A) porous $ZnCo_2O_4@Ni(OH)_2$ nanosheets/NF. 126 (B) $ZnO-ZnCo_2O_4@Ni(OH)_2$ heterostructured nanowires/NF. 125 and (C) $ZnCo_2O_4@Co-Al$ LDH nanowires on NF. 127 Panel A: Reproduced with permission. 126 Copyright © 2018 Wiley-VCH Verlag GmbH & Co. KGaA, Weinheim. Panel B: Reproduced with permission. 125 Copyright © 2020 Elsevier Ltd. All rights reserved. Panel C: Reproduced with permission. 127 Copyright © 2019 Elsevier Ltd and Techna Group S.r.l. All rights reserved.

LDH. 127 The ZnCo₂O₄@Ni(OH)₂/NF electrode (1021.1 F g⁻¹ and 3.06 F cm⁻² at 1 mA cm⁻²)¹²⁶ (Fig. 9A) based on crosslinked ultrathin nanoflakes, covering porous nanosheets with a thick triangular shape, delivered good specific capacitance but low rate-capability and cycling stability. They have been ascribed to the bulkiness of the ZnCo2O4 nanosheets and reduced space between them, which hinders the ion-diffusion and electron transfer. This also reduces the control of the strain effects due to volume changes through cycling. Conversely, ZnO- $ZnCo_2O_4@Ni(OH)_2/NF$ (1901.6 F g^{-1} at 2 A g^{-1})¹²⁵ (Fig. 9B) delivered not only higher specific capacitance, but also high rate-capability for a heterostructured nanowire-based binderfree electrode, with 85.7% capacitance retention at 20 A g^{-1} , along with high cycling stability, retaining 98.7% of its initial capacitance after 5000 cycles. Additionally, the ZnO-ZnCo₂O₄@ ZnO/NF, ZnO-ZnCo₂O₄@CoO/NF and ZnO-ZnCo₂O₄/NF electrodes have been studied for comparison purposes, delivering

approximately 54%, 40% and 31%, respectively, of the specific capacitance of $\rm ZnO-ZnCo_2O_4@Ni(OH)_2/NF$. The superior performance of $\rm ZnO-ZnCo_2O_4@Ni(OH)_2/NF$ is attributed to the nanoflake-covered interconnected nanowires forming a hierarchical porous 2D network on top of the NF. This provides a high surface area, with plenty of space for electrolyte diffusion, which in conjunction with the available electroactive sites facilitates the electron transport through the $\rm ZnO-ZnCo_2O_4$ nanowires

Layered double hydroxides (LDHs) have high theoretical capacity, low cost and environmental compatibility. However, their inherent low conductivity and aggregation effects hinder charge transportation, leading to low electrochemical performance. However, when an LDH is assembled as a shell material combined with a highly conductive core, such as ZnCo₂O₄, superior performance is expected. In fact, ZnCo₂O₄@Co–Al LDH nanowires on NF (2041 F g⁻¹ at 1 A g⁻¹)¹²⁷ (Fig. 9C),

Energy Advances Review

composed of urchin-like porous ZnCo2O4 nanowires, which were uniformly covered with Co-Al LDH nanosheets, delivered higher specific capacitance and rate-capability than pristine ZnCo₂O₄, Ni-Al LDH and Co-Al LDH, and core@shell ZnCo₂O₄@Ni-Al LDH electrodes, retaining 70% of the initial capacitance at 10 A g⁻¹ due to the increase in specific surface area, the high electroactivity of the Co-Al LDH shell, and band alignments between ZnCo₂O₄ and Co-Al LDH, thus facilitating the charge transfer.

3.1.3. ZnCo₂O₄/carbon material composite electrodes. Several carbonaceous materials can be derived from ZnCo₂O₄ as composites encompassing carbon nanotubes (CNTs), 129,134 carbon nanoparticles, 97,100 N-doped carbon, 132 reduced graphene oxide (rGO), 106,130,133 polyaniline (PANI) 131,136 graphitic-carbon nitride (g-C₃N₄)¹³⁵ in slurry-cast electrodes, and carbon, ¹⁴³ N-doped carbon, ^{138,140} rGO, ^{109,137,139,141,142} polyvinylpyrrolidone (PVP)⁶⁶ and polypyrrole (PPy)^{57,144} in binderfree electrodes. Accordingly, is should be possible to explore the combined effects of electric double-layer capacitance (EDLC) from carbonaceous materials, and pseudocapacitance from transition metal oxide materials. In this way, one could overcome the inherent limitations of these carbon materials, e.g., low specific capacitance, and of ZnCo2O4, e.g., low electronic conductivity. They can hinder charge transfer, resulting in low capacitance and poor rate capability, including cyclability, in accordance with theoretical expectations. 100

Polymers, e.g., PANI, 131,136 g-C₃N₄ 135 and PVP, 66 can act as support materials for ZnCo₂O₄, while PPy^{57,144} has been explored as a shell material in core@shell architectures. Embedding ZnCo₂O₄ in g-C₃N₄, a mesoporous sheet-like soft polymer, can produce $g-C_3N_4$ (2 N_4 (1386 F g^{-1} at 4 A g^{-1}) (1386 F g^{-1} at 4 A g^{-1}) (Fig. 10A) with the benefit of the highly active nitrogen sites, large

specific surface area and good overall stability, in addition to lowcost. However, in comparison to pristine ZnCo₂O₄, only 66% of the initial specific capacity was maintained for a 2-fold density current increase. PVP is a bulky, non-toxic, non-ionic polymer containing carbonyl, amine, and alkyl functional groups that can be used as a surfactant, reducing agent, shape controlling agent, and dispersant in nanoparticle synthesis. The self-assembly of PVP was used to produce binder-free hierarchical microflowers of $ZnCo_2O_4/PVP$ composites (761 F g⁻¹ at 0.35 A g⁻¹)⁶⁶ (Fig. 10B) *via* an assisted hydrothermal method. These materials presented relatively poor rate capability, as expected for a flower-like structured material-based binder-free electrode. Notwithstanding, PANI, a semi-flexible rod-like polymer, exhibits a good electrical conductivity with multi-redox activity involving protonation, and can modify ZnCo₂O₄ particles' sizes and shapes thanks to its strong interactions, shortening electron/ion pathways and increasing surface area due to interconnective rodlike structures. As a result, nanosheet-like ZnCo₂O₄/N-GO/PANI $(720 \text{ F g}^{-1} \text{ at } 1.5 \text{ A g}^{-1})^{131}$ (Fig. 10C), based on $\text{ZnCo}_2\text{O}_4/\text{N-GO}$ coverage with multifaceted PANI, and PANI/ZnCo2O4 nanoparticle (867 F g^{-1} at 0.5 A g^{-1})¹³⁶ (Fig. 10D) slurry-cast electrodes exhibited significant changes in size, shape, specific surface area, bond length, electron density, and other parameters. Both delivered excellent cyclability and specific capacitance in comparison to the ZnCo₂O₄/N-GO nanocomposite¹³¹ and pristine ZnCo₂O₄ NPs. 136

PPy is considered to be a promising electrode material owing to its high electrical conductivity, greatly improving the specific capacitance and cycle performance as well as decreasing the overpotential attributed to the promotion of electron transport and reduction of internal resistance. 57,144 ZnCo₂O₄@ PPy/NF (1210 F g^{-1} at 1 A g^{-1})⁵⁷ (Fig. 10E), architectured as

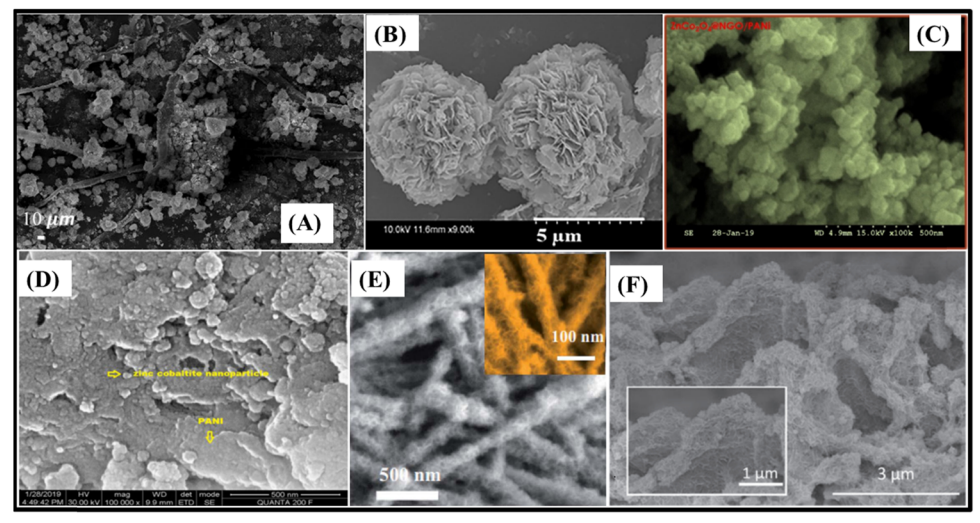


Fig. 10 SEM images of (A) nanosheet-like $g-C_3N_4/ZnCo_2O_4$, (B) 3D flower-like $ZnCo_2O_4/PVP$, (C) nanosheet-like $ZnCo_2O_4/N-GO/PANI$, (B) 3D flower-like $ZnCo_2O_4/PVP$, (C) nanosheet-like $ZnCo_2O_4/N-GO/PANI$, (B) 3D flower-like $ZnCo_2O_4/PVP$, (C) nanosheet-like $ZnCo_2O_4/N-GO/PANI$, (B) 3D flower-like $ZnCo_2O_4/PVP$, (C) nanosheet-like $ZnCo_2O_4/N-GO/PANI$, (B) 3D flower-like $ZnCo_2O_4/PVP$, (C) nanosheet-like $ZnCo_2O_4/N-GO/PANI$, (B) 3D flower-like $ZnCo_2O_4/PVP$, (C) nanosheet-like $ZnCo_2O_4/N-GO/PANI$, (B) 3D flower-like $ZnCo_2O_4/PVP$, (C) nanosheet-like $ZnCo_2O_4/N-GO/PANI$, (D) $ZnCo_2O_4/N-GO/PANI$ (D) PANI/ZnCo₂O₄ annoparticles, 136 (E) ZnCo₂O₄@PPy nanostructures/NF 57 and (F) core@shell ZnCo₂O₄@NiCo₂S₄@PPy. 144 Panel A: Reproduced with permission. 135 Copyright © 2020, The Author(s). Panel B: Reproduced with permission. 66 Copyright © 2020 John Wiley & Sons Ltd. Panel C: Reproduced with permission.¹³¹ © 2020 Elsevier B.V. All rights reserved. Panel D: Reproduced with permission.¹³⁶ Copyright © 2019, Springer-Verlag GmbH Germany, part of Springer Nature. Panel E: Reproduced with permission.⁵⁷ CC BY 3.0. Royal Society of Chemistry. Panel F: Reproduced with permission. 144 Copyright Marketplace TM. IOP Publishing

ultrathin PPv film-coated ZnCo₂O₄ nanowires, delivered about 9 times more specific capacitance than pristine spinel species. On the other hand, the core@shell ZnCo2O4@NiCo2S4@PPy/NF electrode (2507.0 F g⁻¹ and 3.75 F cm⁻² at 0.5 A g⁻¹)¹⁴⁴ (Fig. 10F) presented much better rate-capability, with 69% capacitance retention after a 40-fold increase in current density. This result is associated with its composition, since NiCo₂S₄ exhibits abundant valence states and high theoretical specific capacitance in addition to the more suitable architecture. It resembles porous leaf-like ZnCo2O4 nanosheets covered hierarchically with thin and abundant NiCo2S4 nanosheets and a thin PPy film. This core@shell structure formed by three materials created a bi-interface that can promote the contact with the electrolyte and facilitate ion-diffusion, accelerate the electron transfer, and increase the availability of electroactive sites. However, PPy can contribute to the pseudocapacitance through doping and de-doping redox reactions, increasing the volume changes along the cycling and thus reducing the mechanical stability of the material. Slightly poorer cycling stability than that of ZnCo₂O₄@NiCo₂S₄/NF was observed, without PPy coating, but, in contrast, the specific capacitance

Carbon (C) is also considered to be a promising candidate to form a composite material for ZnCo2O4-based electrodes in supercapacitive applications, due to its good volume expansion tolerance and excellent electron transport. The use of C can effectively improve the overall electrical conductivity of the material, decrease the volume expansion, and inhibit the agglomeration of ZnCo₂O₄ in the redox reaction process, thus improving the specific capacitance and cycling stability. This is the case of the core@shell ZnCo₂O₄@C/NF electrode (2340 F g⁻¹

almost doubled after the coating.

and 7.02 F cm⁻² at 1 mA cm⁻²), ¹⁴³ composed of agglomerated ZnCo₂O₄ nanoparticles as porous nanowire arrays, covered with a thin amorphous carbon layer, leading to high specific capacitance and good cycling stability (capacitance retention of 92.6% after 10 000 cycles).

Notwithstanding, N-doped carbon (NC) supported P- $ZnCo_2O_4$ nanosheets (1581.5 F g^{-1} at 1 A g^{-1})¹³² (Fig. 11A), in which the NC acted as a 3D continuous network, provided a highly electrically conductive support with large surface area for the growth of P-doped ZnCo₂O₄ nanosheets. They showed much better results, with 90.6% rate capability after a 10-fold current density increase. The triangular-shaped P-doped ZnCo₂O₄ nanosheets are rich in oxygen vacancies, due to their substitution for phosphorus ions. In this way, ion-diffusion and the absorption of OH⁻ are facilitated. There are a large interface contact area and shortened electron/ion diffusion paths, which is an interesting strategy to improve ZnCo₂O₄ electrochemical performances in slurry-cast electrodes.

As for binder-free electrodes, in recent years the relevant systems studied were ZnCo₂O₄/NC hollow nanowall arrays/ flexible carbon textiles (CT) ($\sim\!2003.8~F~g^{-1}$ at $\sim\!1.79~A~g^{-1})^{138}$ and NC/ZnCo₂O₄ honeycomb-like nanostructures (1289 F g⁻¹ at 3.5 A g⁻¹). 140 The first one 138 (Fig. 11B) is based on NC hollow nanowall arrays that serve as the backbone and conductive connection for porous ultrathin ZnCo2O4 nanoflakes. They increase the contact area with the electrolyte and enable fast redox reaction, featuring high specific surface area and short ion diffusion paths. This leads to high rate-capability and cycling stability, with 74.7% and ~99.4% capacitance retention, when increasing the current density to 57.14 A g⁻¹ and after 10 000 cycles, respectively. The second one 140 (Fig. 11C)

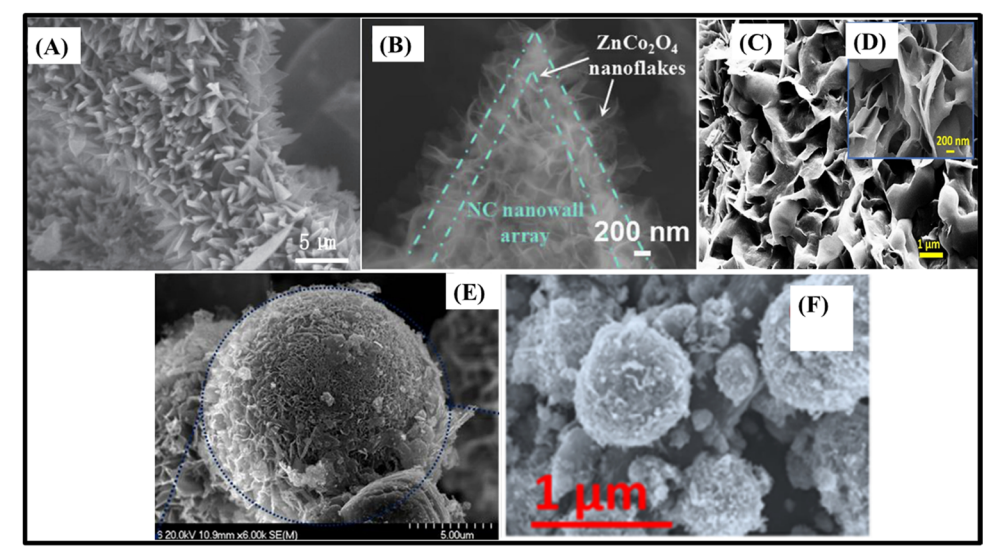


Fig. 11 (A) SEM image of N-doped C supported P-ZnCo₂O₄ nanosheets. (B) TEM image of ZnCo₂O₄/N-doped carbon hollow nanowall arrays/CT. (138) SEM images of (C and D) N-doped carbon/ZnCo₂O₄ honey nest nanostructures, ¹⁴⁰ (E) cauliflower-like AuNP/rGO-ZnCo₂O₄ ¹³³ and (F) NiCo₂O₄-ZnCo₂O₄/rGO nanosheets. ¹⁰⁶ Panel A: Reproduced with permission. ¹³² © 2020 Elsevier B.V. All rights reserved. Panel B: Reproduced with permission. ¹³⁸ © 2019 Published by Elsevier B.V. Panels C and D: Reproduced with permission. 140 Copyright © 2020, Springer Science Business Media, LLC, part of Springer Nature. Panel E: Reproduced with permission. 133 Copyright © 2019 Elsevier B.V. All rights reserved. Panel F: Reproduced with permission. 106 Copyright © 2020 American Chemical Society

Energy Advances Review

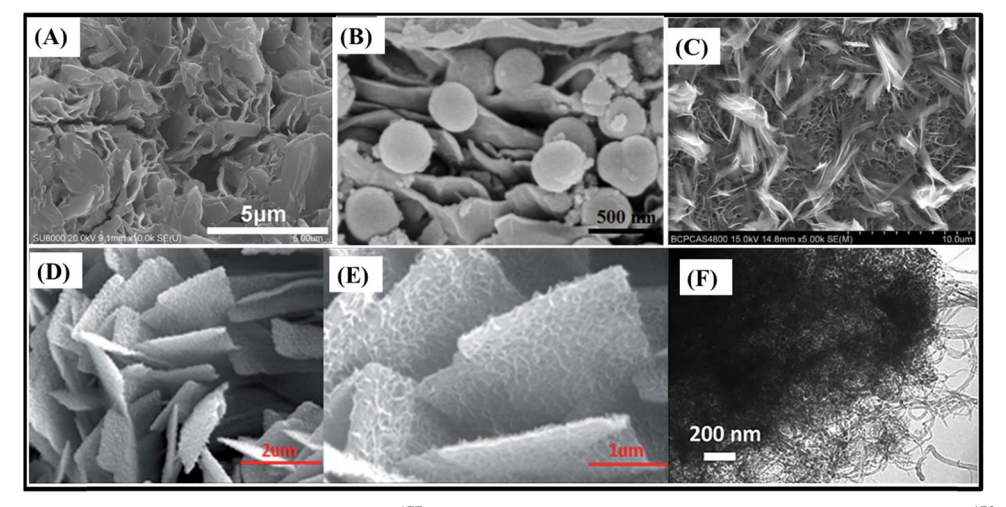
shows less competitive performance, but it involves an interesting strategy for the production of NC using high fructose corn syrup as a green, abundant, and inexpensive carbon source for producing 3D porous ultrathin nanoflakes in a honeycomb-like morphology. The arrangement facilitates the penetration of the electrolyte, providing small contact impedance, and improved ion and electron transportation, yielding relatively good rate capability and cycling stability, with 70% and 86% capacitance retention at 20 A g⁻¹ and after 2000 cycles.

As for carbon nanoparticles (CNPs), there are examples in which they were dispersed onto ZnO/ZnCo₂O₄ nanosheets to produce CNP/ZnO/ZnCo₂O₄ derivatives (593.6 F g⁻¹ at 0.25 A g⁻¹). 100 Electrospun 1D ZnCo₂O₄/C nanofibers, consisting of a ZnCo₂O₄ and carbon nanoparticle mixture (327.5 F g⁻¹ at 0.5 A g⁻¹), have also been reported.⁹⁷ Both materials don't use carbon as a conductive support, but in the form of dispersed nanoparticles. Therefore, the ions should diffuse through them to reach the electroactive material. As a result, they present low specific capacitances and very poor rate capabilities, despite the high cycling stability due to their optimized morphologies and CNP incorporation. 97,100

Other highly conductive carbon materials, such as CNTs¹²⁹ and rGO, 106,133 have also been studied as supports for ZnCo₂O₄ in slurry cast electrodes, and both presented remarkable results. It should be noted that rGO has a large specific surface area, high electrical conductivity, good thermal stability, and excellent mechanical flexibility, displaying all benefits of 2D morphologies and superb possibilities as a support material. Nonetheless, π - π interactions and van der Waals forces between graphene sheets cause a restacking effect of rGO at higher current densities. This can limit its electrochemical performance, due to reduction in the specific surface area and creation of difficult channels for electrolyte ion transportation.

The cauliflower-like AuNP/rGO-ZnCo₂O₄ (54.1 mA h g⁻¹ at 25 mA cm⁻²)¹³³ (Fig. 11D) was based on the incorporation of AuNPs within rGO nanosheets to prevent the restacking effect. However, rGO nanosheets were coated with flower-like ZnCo₂O₄ in order to increase their specific surface area. Therefore, this material did not work as a support material. The electrode delivered low specific capacity although it presented high cycling stability. In contrast, heterostructured NiCo₂O₄- $ZnCo_2O_4/rGO$ nanosheets $(2176.4 \text{ F g}^{-1} \text{ at 1 A g}^{-1})^{106}$ (Fig. 11E), composed of spherical NiCo₂O₄@ZnCo₂O₄ heterostructures (urchin-like NiCo2O4 and sheetlike ZnCo2O4) that were supported on rGO nanosheets, delivered the highest specific capacitance among all reviewed slurry-cast electrodes. This material afforded 58.2% rate capability after a 20-fold current density increase and 93.8% capacitance retention after 5000 charge/discharge cycles. Not coincidentally, the three best slurry-cast electrodes were those based on NiCo2O4-ZnCo2O4 composites supported onto rGO.

Binder-free electrode materials based on ZnCo₂O₄ and rGO composites have also been studied in recent years. 109,137,139,141,142 ZnCo₂O₄/rGO intertwined sheets on NF (3222 F g⁻¹ at 1 A g⁻¹)¹³⁷ (Fig. 12A) presented specific capacitance superior to other ZiCobased composite materials containing rGO such as ZnCo-layered double hydroxide@rGO/NF (2142.0 F g⁻¹), 145 ZnCo-sulfide-rGO 3D hollow microsphere flowers (1225.1 F g⁻¹)¹⁴⁶ and CoO-ZnO/ rGO/NF (1951.8 F g^{-1}), ¹⁴⁷ but with poor rate capability and cycling stability, retaining only 26.7% and 65% after a 20-fold current density increase and 5000 cycles. This is due to the slow iondiffusion rates induced by the fused porous ultrathin ZnCo2O4 curl nanosheets coated onto the vertically interconnected rGO nanosheets, limiting the penetration of electrolyte. Porous ZnCo₂O₄ nanosheets directly grown on rGO-coated NF (680 F g⁻¹ at 1 A g⁻¹)¹⁴² presented the poorest specific capacitance among all reviewed electrodes, but it is inferred that the



 $\textbf{Fig. 12} \quad \text{SEM images of (A) } ZnCo_2O_4/rGO \text{ intertwined sheets/NF,} \\ ^{137} \text{ (B) sandwich-like } ZnCo_2O_4 \text{ hollow spheres/rGO lamellar film,} \\ ^{139} \text{ (C) heterostructured } \\ ^{137} \text{ (B) } Sndwich-like \\ ^{137} \text{ (B) } Sndwi$ ZnCo₂O₄/N-rGO/NF, ¹⁴¹ and (D and E) MnO₂-decorated ZnCo₂O₄ nanosheets on rGO-doped NF. ¹⁰⁹ (F) TEM image of ZnCo₂O₄/CNT nanoflowers. ¹²⁹ Panel A: Reproduced with permission. 137 Copyright © 2018 Elsevier B.V. All rights reserved. Panel B: Reproduced with permission. 139 Copyright © 2020 Published by Elsevier B.V. Panel C: Reproduced with permission. ¹⁴¹ CC BY-NC 3.0. Royal Society of Chemistry. Panels D and E: Reproduced with permission. 109 CC BY-NC 3.0. Royal Society of Chemistry. Panel F: Reproduced with permission. 209 Copyright © 2019 Elsevier B.V. All rights reserved.

rGO can effectively buffer ZnCo2O4 nanosheets' volume changes through cycling and enhance the electrical conductivity. It can act as bridges for electron transfer, but the rGOcoated NF seems to not actively promote the ion-diffusion rates, exhibiting 88% capacitance retention after just a 5-fold current density increase. Lamellar films of ZnCo2O4/rGO hollow spheres (1075.4 F g^{-1} at 1 A g^{-1})¹³⁹ (Fig. 12B) present a sandwich-like structure. The sandwiched hollow nanospheres can expand the inner-space and minimize the aggregation of rGO, facilitating and accelerating the electrolyte diffusion and increasing the cycling stability. On the other hand, heterostructured ZnCo $_2$ O $_4$ /N-rGO on NF (1600 F g^{-1} at 1 A g^{-1}) 141 (Fig. 12C) features ultrathin and porous honeycomb-like nanosheets and nanofeathers, with a hierarchical double-morphology. These characteristics, respectively, increase the active surface area and hinder the volume change through cycling. The N-doped rGO seems to parallelly orient the growth of ZnCo₂O₄ nanosheets, thus delivering 78.1% of the initial capacitance even after a 30-fold current density increase. Finally, MnO₂decorated ZnCo₂O₄ nanosheets on rGO-doped NF (3405.2 F g⁻¹ at 2 A g⁻¹)¹⁰⁹ (Fig. 12D and E) feature the combined benefits of composites based on MnO2 and rGO. They were electrodeposited onto porous ZnCo2O4 nanosheets and on rGO-coated NF, thus delivering very high specific capacitance and good cycling stability (91.2%, 5000 cycles) but relatively poor rate capability (64.9%, 10-fold increase). In this way, they behave as porous ZnCo₂O₄ nanosheets on rGO-doped NF,¹⁴² because the rGO coating limits the ion-diffusion at higher current densities.

CNTs present all advantages of 1D materials along with the increased conductivity of a carbon material. Therefore, when used as a support and connective material, they provide improved charge and electron transfer pathways. 129,134 A MWCNT/ZnCo₂O₄ slurry-cast electrode (64 mA h $\rm g^{-1}$ at 1 A $\rm g^{-1})^{134}$ presented nearly double the specific capacity of pristine ZnCo2O4 due to its hexagonal nanoplates connected by multiwalled carbon nanotubes, even though it delivered very low specific capacity and rate capability. On the other hand, ZnCo₂O₄/CNT nanoflowers¹²⁹ (Fig. 12F) delivered a high specific capacitance of 1203.8 F g⁻¹ at 1 A g⁻¹, in which CNTs interpenetrate the ZnCo₂O₄ flowers acting as both a conductive additive and a buffer material. This facilitates ion diffusion rates and rapid electron transfer and reduces interior stress and volume expansion during electrochemical reactions, increasing the cycling stability and electrochemical performances of the electrode.

3.1.4. The top 10 highest specific capacitances for electrode materials based on ZnCo₂O₄. The highest specific capacitances among pristine ZnCo₂O₄ and ZnCo₂O₄-based composites as slurry-cast or binder-free electrodes are illustrated in Fig. 13A. The best pristine ZnCo₂O₄-based slurry-cast electrode delivered much lower specific capacitance in comparison to the other electrodes. It is interesting to note that the highest specific capacitances of pristine binder-free and composite slurry-cast electrodes are quite similar, even though each one of these strategies is uniquely effective. Thus, the best way to improve ZnCo₂O₄-based electrodes is to combine the rational design of composites and the production of binder-free electrodes. In fact, among the top 10 electrode materials, 9 of them are composite binder-free electrodes (Fig. 13B). In fact, the highest specific capacitance was achieved by MnO2-decorated ZnCo2O4 nanosheets on rGO-doped NF. The improved specific capacitance was provided by the additional MnO2-decorated electroactive material and the electrical conduction associated with the rGO-doped NF substrate used for the growth of ZnCo₂O₄ nanosheets.

Notwithstanding, there is still a possible limitation to be taken into consideration: in such architectures, the space between the nanostructures plays an important role in the ion-diffusion rates and in the availability of electroactive sites at higher current densities. This is pretty evident in binder-free electrodes based on ZnCo₂O₄ nanowires that can present very high specific capacitance, but low rate-capability. As a result, the best rate-capabilities are achieved by these binder-free

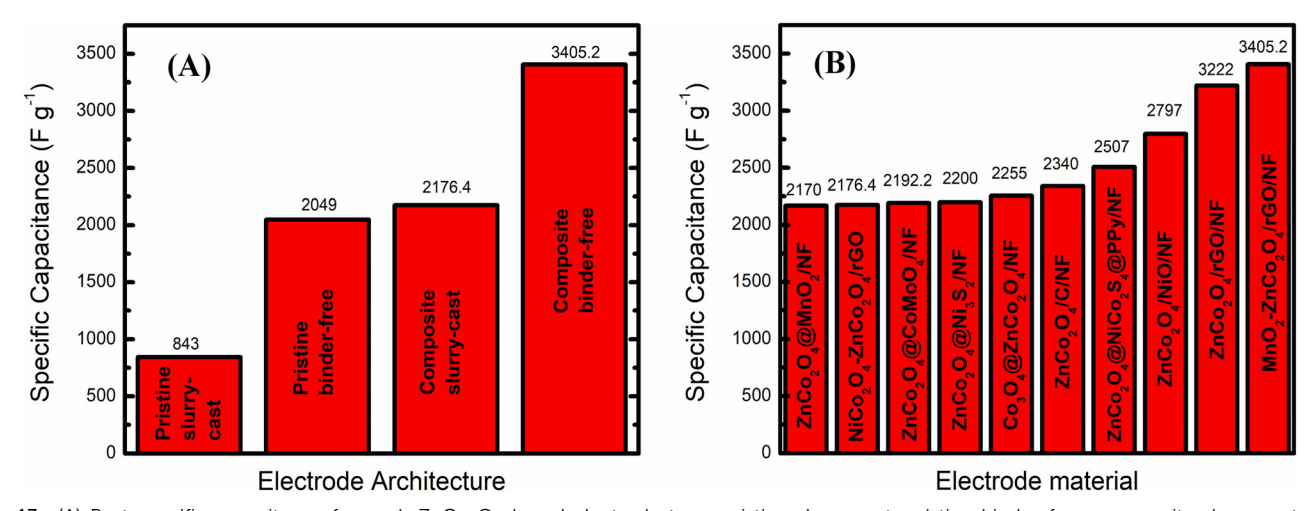


Fig. 13 (A) Best specific capacitance for each ZnCo₂O₄-based electrode type: pristine slurry-cast; pristine binder-free; composite slurry-cast and composite binder-free (ref. 11, 26, 58 and 62, respectively). (B) Top 10 specific capacitances delivered by ZnCo₂O₄-based electrodes (ref. 62, 43, 38, 90, 84, 67, 75, 79, 58 and 89, respectively)

This article is licensed under a Creative Commons Attribution-NonCommercial 3.0 Unported Licence.

Open Access Article. Published on 03 októbra 2022. Downloaded on 9.12.2025 11:08:47.

Energy Advances

electrodes with suitably spaced nanostructures and high avail-

3.2.1. Lithium-ion batteries. Rechargeable Li-ion batteries (LIBs) received extensive investments because of their excellent cyclability, good safety performance, and high-energy density. Since the early 1990s, LIBs have been widely used in portable electronic and electric vehicles. 11 A LiCoO2 cathode and a graphite anode are some of the most well-known commercial LIB material pairings. 148-150 Unfortunately, so far, the traditional intercalation-type material, graphite, generally has suffered from its low theoretical specific capacity (372 mA h g⁻¹) and poor rate performance, which hinders the large-scale application of LIBs. 151 Other potential anode materials, such as spinel-structure mixed transition metal oxides, have emerged as ideal candidates due to their higher lithium storage capacity (500-1500 mA h g⁻¹). 11,152 Among various spinel oxides, ZnCo₂O₄ has captured great attention due to its special lithiation properties, environmental benignity, affordable price, good conductivity, and high theoretical specific capacity $(900 \text{ mA h g}^{-1}).^{153,154}$ Up to now, many types of ZnCo_2O_4 materials with different morphologies, such as nanoribbons,⁸¹ nanoboxes,¹⁵⁵ nanosheets,^{152,156,157} microcubes,¹⁵⁸ nanocubes, 159 nanospheres, 160-164 nanotubes, 165 and nanocages, 166 have been applied in LIBs.

To increase mass transfer and contact between electrodes and electrolyte, Zhang et al. 152 reported nickel foam supported hierarchical ZnCo₂O₄ nanosheets prepared by the solutionbased method. A reversible specific capacity of 773 mA h g⁻¹ at 0.25 A g⁻¹ over 500 cycles was found for the porous ZnCo₂O₄ nanosheets. Song et al. 157 also reported the synthesis of ZnCo₂O₄ nanosheets; when evaluated as an anode material for LIBs, the electrode showed an initial specific capacity of 1979 mA h g^{-1} and a stable discharge capacity of 688 mA g^{-1} at 0.5 A g⁻¹ after 1000 cycles. Another ZnCo₂O₄ nanosheet material reported in the literature delivered a reversible capacity of 1640.8 mA h g⁻¹ at a current density of 100 mA g⁻¹ after 50 cycles. 156

The morphology of the material plays a crucial role in the overall electrochemical performance, and thus, various morphologies have been intensively pursued and well designed. For example, Chen et al. 160 synthesized ZnCo₂O₄ nanospheres with the desired shape via a one-step solution method. The ZnCo₂O₄ nanospheres showed an initial discharge capacity of 1320 mA h g^{-1} at a current density of 100 mA g^{-1} and a capacity retention rate of 76.22% after 50 charge and discharge cycles. Cheng et al. 167 synthesized 1D porous ZnCo₂O₄ tailored cuboids with green natural soybean oil by a micro-emulsion strategy. This material exhibited an initial coulombic efficiency of 80.6% and a specific capacity of 1029.3 mA h g⁻¹ at 1000 mA g⁻¹ over 400 cycles. Lately, Li et al. 153 synthesized 3D mesoporous ZnCo₂O₄ architectures by the ethylene glycol combustion strategy. The average specific capacity of the ZnCo₂O₄ electrode can return to about 778.7 mA h g⁻¹ at a current density of 200 mA g⁻¹ over 50 cycles. 3D hierarchical ZnCo₂O₄ nanocubes prepared by a hydrothermal method delivered a reversible specific capacity of 775 mA h g⁻¹ after 100 cycles at 500 mA g⁻¹. 159

Hollow nanostructures have attracted considerable attention; their unique structure enables a high specific surface area, tunable chemical composition, and short charge transport pathway. Xue et al. 164 developed a universal self-template approach to synthesize multishelled hollow ZnCo₂O₄ spheres (Fig. 14A and B), which displayed a specific capacity of 1020 mA h g^{-1} at 100 mA g^{-1} (Fig. 14C), a cycling durability of 1200 mA h g^{-1} after 200 cycles at 0.1 A g^{-1} and a rate capability of 730 mA h g^{-1} at 5.0 A g^{-1} . Similarly, Deng et al. ¹⁶⁸ proposed a citrate-assisted hydrothermal synthesis to generate hollow ZnCo₂O₄ octahedral particles (Fig. 14D and E). Battery tests demonstrated a specific capacity of 1110 mA h g⁻¹ at 0.2 A g^{-1} (Fig. 14F) and a capacity retention of 60% at 5 A g^{-1} over 60 cycles.

The main electrochemical performances for ZnCo₂O₄ with different morphologies are summarized and listed in Table 6. Hollow porous structures composed of 2D structures of ZnCo₂O₄, such as nanosheets, showed superior electrochemical performance to other nanostructures or microstructures in LIBs, due to the interior hollow structure which can accommodate the huge volume expansion and provide more active lithiation sites; thus, ZnCo2O4 structures exhibit higher capacity and cycling stability than the other materials, and second, the porous structures ensure sufficient contact between active materials and electrolyte. Therefore, it can be concluded that 2D nanostructures of ZnCo2O4 would be considered as an optimum architecture for high-performance ZnCo₂O₄.

Although the theoretical capacity of ZnCo₂O₄ as an anode material is high (900 mA h g⁻¹), 154 tremendous efforts have been paid, in recent years, to increasing the conductivity and overcoming the volume expansion of ZnCo2O4 caused by lithium-ion insertion/extraction, which results in its fast fading of capacity. One strategy is the combination with transition metal oxides such as ZnO/ZnCo₂O₄/Co₃O₄, ¹⁸⁰ ZnCo₂O₄/ Co₃O₄, ¹⁷⁷⁻¹⁷⁹ N-ZnCo₂O₄/CoO, ¹⁸³ ZnCo₂O₄@NiO, ¹⁸⁵ Ni-NiCo₂O₄@ ZnCo₂O₄, ¹⁸¹ and ZnCo₂O₄(a)Fe₂O₃-C, ¹⁸² which can alleviate the problem through the synergy effect of bimetallic oxides.

The construction of hollow and 3D porous structures is another effective strategy, promoting the generation of voids, which can alleviate the structural stress and buffer the volume variation. For example, a novel route to prepare hollow Co₃O₄ nanospheres doped with ZnCo2O4 was demonstrated by Song et al. 179 (Fig. 15A). This nanocomposite shows a specific capacity of 890 mA h g^{-1} at a current density of 0.1 A g^{-1} and displays a similar specific capacity at 1 A g⁻¹ after 120 cycles (Fig. 15B). Guo et al. 177 reported the synthesis of a 3D porous ZnCo₂O₄/Co₃O₄ composite on carbon cloth (Fig. 15C). The asprepared composite exhibits an enhanced lithium storage property of 1350.0 mA h g^{-1} at 0.3 A g^{-1} and a cycling performance of 64% over 105 cycles at 0.3 A g^{-1} (Fig. 15D). Li et al.178 also prepared ZnCo2O4/Co3O4 hierarchical hollow ZnCo₂O₄/Co₃O₄ microspheres via solvothermal synthesis followed by thermal annealing. When used as an anode material

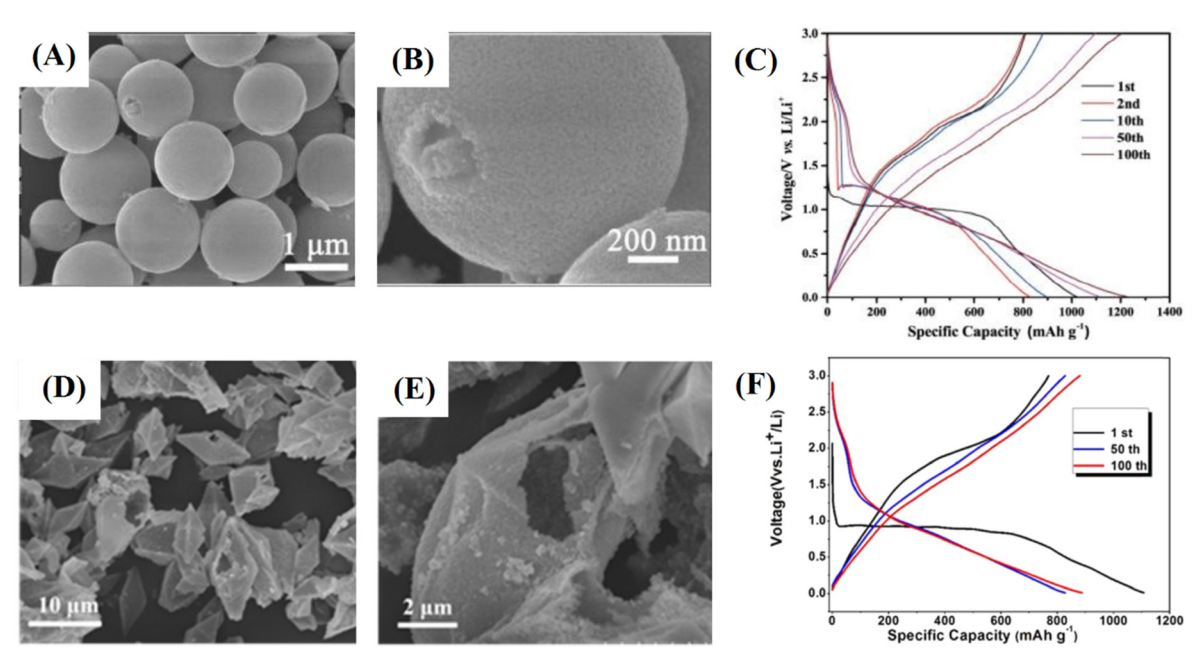


Fig. 14 (A and B) SEM images of ZnCo₂O₄ multishelled hollow spheres at different magnifications. (C) Galvanostatic charge/discharge curves of a $ZnCo_2O_4$ multi-shelled hollow sphere anode at a current density of 100 mA g^{-1} . Reproduced with permission. ¹⁶⁴ Copyright Marketplace TM. Royal Society of Chemistry. (D and E) SEM images of ZnCo₂O₄ hollow structures at different magnifications. (F) Galvanostatic charge/discharge curves of a ZnCo₂O₄ hollow anode at a current density of 0.2 A g⁻¹. Reproduced with permission. Copyright © 2017 Published by Elsevier B.V.

for LIBs, this material exhibits a rate capability of 842 mA h g⁻¹ at a current density of 4 A g⁻¹ and a cycle life of 754 mA h g⁻¹ after 800 cycles at a current density of 2 A g^{-1} . The development of hollow structures based on ZnCo₂O₄/Co₃O₄ composites demonstrated that the hierarchical hollow structure with high porosity relieves the volume expansion and increases the contact area between the electrode and electrolyte, increasing discharge capacity and cycling performance.

Another strategy to solve concerns in terms of lithium diffusion kinetics, electronic transport, volume change, and particle agglomeration is to anchor ZnCo₂O₄ structures onto electrically conductive nanostructured carbon materials. Hence, some carbonaceous materials including carbon nanotubes (CNTs), 129,198,199 reduced graphene oxide (rGO), 187-192 polyaniline (PAN), 210 n-doped carbon layers, 208,222 carbon cloth (CC), 194,195,223 and carbon porous structures 202-204 were used as inert and conductive matrices in ZnCo₂O₄ based anode materials. For instance, binder-free and self-supporting anode materials were prepared based on carbon-coated ZnCo2O4 composites. The lithium storage properties were as follows: a high initial discharge (1951.4 mA h g⁻¹) and good capacity after cycling (88.6.4 mA h g^{-1} over 100 cycles at 200 mA g^{-1}). 209 In addition, Huang et al. 223 prepared a ZnCo2O4@CC nanocomposite with a reversible capacity of 1376 mA h g⁻¹ even after 200 cycles at a current density of 1 A g^{-1} .

Graphene has attracted widespread attention due to its unique properties such as mechanical flexibility, excellent conductivity (1600 S m⁻¹), large specific surface area (2630 m² g⁻¹), and chemical stability.²²⁴⁻²²⁷ The introduction of graphene into ZnCo₂O₄ structures can accommodate serious volume expansion, prevent agglomeration of ZnCo2O4 material over continuous lithiation/delithiation cycles, and, meanwhile, improve the electrical conductivity of the hybrids. 187,228,229 For example, Wang et al.191 prepared interconnected mesoporous ZnCo₂O₄ nanosheets on 3D graphene foam (Fig. 16A), which had a discharge capacity of 1233 mA h g⁻¹ at 500 mA g⁻¹ after 240 cycles (Fig. 16B). Ren et al. 188 fabricated a ZnCo₂O₄@rGO nanocomposite to be used as a LIB anode. The ZnCo₂O₄@rGO electrode exhibited cycling stability (1589 mA h g⁻¹ at 100 mA g^{-1} after 140 cycles) (Fig. 16C). Xie et al. developed a rapid laser-irradiation methodology for the synthesis of oxygenvacancy abundant nano-ZnCo₂O₄/porous rGO hybrids as anodes for LIBs (Fig. 16E). The results showed that the nano-ZnCo₂O₄/ porous rGO has a reversible capacity of ~ 1053 mA h g⁻¹ at $0.05~{\rm A~g}^{-1}$ and a cycling stability of \sim 746 mA h g⁻¹ at 1.0 A g⁻¹ after 250 cycles (Fig. 16D). 192 In these cases, the rGO acts as a conductive substrate for anchoring the ZnCo₂O₄ structure, which increases the electrical conductivity and avoid the structure collapse upon cycling (Fig. 16F).

The combination in the composites, taking full use of the good conductivity and high surface area of carbon materials, efficaciously heightens the undesirable conductivity of ZnCo₂O₄, thereby affording enhanced electrochemical behaviors in LIBs. The carbon coated ZnCo₂O₄ nanocomposites have large surface areas, resulting in better electrolyte wettability and high conductivity, which contribute to cycling stability. This effective approach to fabricating material composites not only has the advantages of all the constituents, but also overcomes the disadvantages of the individual components.

183 184 184 185 186 187 189 190 191 193 194 195 196 197 961 97.3%/1000 cycles 92.3%/300 cycles 76.22%/50 cycles 64.2%/105 cycles 76%/1000 cycles 66%/2000 cycles 99.7%/90 cycles 85%/800 cycles 87%/500 cycles 94%/50 cycles 71%/80 cycles 60%/60 cycles Stability .296.91 (200)/100 mA g⁻¹ $791 (1000)/1 \text{ A g}^{-1}$ $1100 (2000)/4000 \text{ mA g}^{-1}$ 1029.3 (400)/1000 mA g⁻¹ 1005.8 (180)/500 mA g⁻¹ $1107.2 (100)/100 \text{ mA g}^{-1}$ 1640.8 (50)/100 mA g⁻¹ 412 (600)/1200 mA g⁻¹ $1613 (400)/500 \text{ mA g}^{-1}$ $730.5 (200)/800 \text{ mA g}^{-1}$ $1200(200)/0.1 \text{ mA g}^{-1}$ 625 (800)/500 mA g⁻¹ 688 (1000)/5 A g⁻¹ 773 (500)/0.25 A g⁻¹ 779.6 (50)/200 mA g⁻¹ 1063 (50)/200 mA g⁻¹ 910 (300)/1 A g⁻¹ 890 (120)/0.1 A g⁻¹ 1428 (100)/200 mA g⁻ 891.7 (200)/100 mA g 952 $(100)/100 \text{ mA g}^{-1}$ 978 $(500)/1 \text{ A g}^{-1}$ 775 (100)/500 mA g⁻¹ 588 (1000)/1 A g⁻¹ 1025 (200)/500 mA g⁻ 1180 (275)/200 mA g $741 (800)/1000 \text{ mA g}^{-1}$ 997 $(500)/1.0 \text{ A g}^{-1}$ 908.7 (500)/500 mA g 1223 (240)/500 mA_.g⁻ 525 (50)/100 mA g⁻¹ 1140 (200)/0.4 A g⁻¹ 815 (500)/500 mA g⁻ 516 (50)/60 mA g⁻¹ $100)/0.24 \text{ mA cm}^{-2}$ 1422 (80)/200 mA g 481.9 $(105)/0.3 \text{ A g}^-$ 754 $(800)/2 \text{ A g}^{-1}$ $946 (1000)/1 \text{ Åg}^{-1}$ 701 (60)/0.25 A $^{-1}$ 440 (200)/100 mA Reversible capacity 1097.5 (600)/1 A g⁻ 130.4 (1000)/2 A g $\sim 746 (250)/1 \text{ A g}^{-}$ $880 (160)/0.2 \text{ A g}^{-}$ $1375 (200)/1 \text{ A g}^{-}$ 3.01 mA h cm $^{-2}$ 950 (90)/0,1C Nth) mA h g 681 (40)/C/20 Potential window 0.005-3 Li/Li⁺ 0.01-3 Li/Li⁺ $0.01-2.5 \text{ Li/Li}^{+}$ $0.005-3 \text{ Li/Li}^{+}$ 0.01-3 Li/Li⁺ 0.01-3 Li/Li⁺ 0.01-3 Li/Li $0.01-3 \text{ Li/Li}^{+}$ 0.01-3 Li/Li 0.01-3 Li/Li 0.01-3 Li/Li $0.01-3 \text{ Li/Li}^{\dagger}$ $0.01-3 \text{ Li/Li}^{+}$ 0.01–3 Li/Li 0.01-3 Li/Li $0.01-3 \text{ Li/Li}^{\dagger}$ $0.01-3 \text{ Li/Li}^{\dagger}$ $0.02-3 \text{ Li/Li}^{+}$ 0.01-3 Li/Li $0.01-3 \text{ Li/Li}^{+}$ 0.01-3 Li/Li⁺ $0.01-3 \text{ Li/Li}^{+}$ $0.01-3 \text{ Li/Li}^{+}$ $0.01-3 \text{ Li/Li}^{+}$ 0.01-3 Li/Li $0.01-3 \text{ Li/Li}^{+}$ $0.01-3 \text{ Li/Li}^{\dagger}$ $0.01-3 \text{ Li/Li}^{+}$ $0.01-3 \text{ Li/Li}^{\dagger}$ $0.01-3 \text{ Li/Li}^{+}$ $0.01-3 \text{ Li/Li}^{+}$ 0.01-3 Li/Li⁺ $0.01-3 \text{ Li/Li}^{+}$ $0.01-3 \text{ Li/Li}^{\dagger}$ $0.01-3 \text{ Li/Li}^{+}$ $0.01-3 \text{ Li/Li}^{+}$ 0.01-3 Li/Li $0.01-3 \text{ Li/Li}^{+}$ $0.01-3 \text{ Li/Li}^{+}$ $0.01-3 \text{ Li/Li}^{+}$ 0.01-3 Li/Li⁺ $0.01-3 \text{ Li/Li}^{+}$ 0.01-3 Li/Li⁺ $0.01-3 \text{ Li/Li}^{+}$ $0.01-3 \text{ Li/Li}^{+}$ 0.01-3 Li/Li 0.01-3 Li/Li (V vs.) $1179 \text{ mA h cm}^{-3}$ $2.78 \text{ mA h cm}^{-2}$ initial discharge mA h g⁻¹ ~ 1230 1353 1350.01595.8 1097.3 21611710.2 1307.8 1128.0 1398.8 1303.9 1141.7 1947.1 1049 1087 1328 1020 1482 1320 1477 1480 1587 801.5 963.9 1146 1376 1413 1265 1093 1586 2094 297 1567 1051 1541 1501 1385 ZnCo₂O₄@3D graphene film@Ni foams 3D mesoporous ZnCo₂O₄ nanoparticles Multi-shelled hollow ZnCo₂O₄ spheres ZnCo₂O₄ assembled with nanosheets Micro-nanoporous ZnCo2O4 spheres Nanosheathed ZnCo₂O₄ spheroids Yolk-shell ZnCo₂O₄ microspheres 3D Zn_{0.2}Ni_{0.8}Co₂O₄ microspheres Zn_{1-x}Co_xO/ZnCo₂O₄ Yolk-shell ZnCo₂O₄ spheres/rGO ZnCo₂O₄/ZnO/carbon nanotubes Zn defective ZnCO₂O₄ nanorods Zn_xCo_{3-x}O₄ hollow nanoboxes Co₃O₄/ZnCo₂O₄ microspheres Hollow ZnCo₂O₄ octahedrons 3D porous ZnCo₂O₄@NiO/NF 1D porous ZnCo₂O₄ cuboids Yolk-shell ZnCo₂O₄ spheres /olk-shell nanotetrahedrons ZnCo₂O₄ microspheres/rGO Hollow polyhedral ZnCo₂O₄ 3D ZnO/ZnCo₂O₄/Co₃O₄/Cu ZnCo₂O₄ nanoplates on CC rGO@ZnCo2O4 nanosheets 3D ZnCo₂O₄ microspheres 3D porous ZnCo₂O₄/Co₃O₄ Graphene/porous ZnCo₂O₄ Hierarchical micro-sized ZnCo₂O₄ nanosheets/NF Microcube-like ZnCo₂O₄ 3D ZnCo₂O₄ nanocubes ZnCo₂O₄@Fe₂O₃-C N-doped ZnCo₂O₄/CoO $Ni-NiCo_2O_4@ZnCo_2O_4$ ZnCo₂O₄ nanospheres ZnCo₂O₄ nanoribbons ZnCo₂O₄ micro-cubes ZnCo₂O₄ nanosheets ZnCo₂O₄ nanosheets Needle-like ZnCo₂O₄ Nano-ZnCo₂O₄@rGO ZnCo2O4 nanocages ZnCo₂O₄ nanotubes ZnCo₂O₄-graphene C/ZnCo₂O₄/CNTs Co₃O₄/ZnCo₂O₄ ZnCo₂O₄/Co–B ZnCo₂O₄/rGO ZnCo₂O₄@CC $ZnCo_2O_4/CC$ Material Composites with carbon materials Composites with oxides Pristine Li-ion Type

Performances reported for ZnCo₂O₄-based materials for metal ion batteries Table 6

This article is licensed under a Creative Commons Attribution-NonCommercial 3.0 Unported Licence. Open Access Article. Published on 03 októbra 2022. Downloaded on 9.12.2025 11:08:47.

Table 6 (continued)

Try 1553 0.005-3 Li/Li ⁺ 1507 (200)/100 mA g ⁻¹ 1707 (120200 mA g ⁻¹ 1200 (120)/200 mA g ⁻¹ 1200 ma g ⁻¹ 1418.1 0.01-3 Li/Li ⁺ $\sim 760.3 (100)/0.1 C$ 0.01-3 Li/Li ⁺ 1145 (100)/0.1 A g ⁻¹ 1200/30 mA g	Type	Strategy	Material	Initial discharge $(mA h g^{-1})$	Potential window (V ν s.)	Reversible capacity (N th) mA h g^{-1}	Stability	Ref.
			ZnCo ₂ O ₄ @CNTs	2553	0.005-3 Li/Li ⁺	$1507 (200)/100 \text{ mA g}^{-1}$	I	200
ZnCo ₂ O ₄ /ZnO/C 1589 0.005-3 Li/Li ⁺ (622; 61000)/4 Ag ⁻¹ ZnCo ₂ O ₄ /C 1703.7 0.01-3 Li/Li ⁺ (622; 61000)/4 Ag ⁻¹ ZnCo ₂ O ₄ /C 1703.7 0.01-3 Li/Li ⁺ (622; 61000)/4 Ag ⁻¹ ZnCo ₂ O ₄ /C 2.00-3 Li/Li ⁺ (100)/0.1C 1.00.3 Li/Li ⁺ (100)/0.1 Ag ⁻¹ ZnCo ₂ O ₄ (C 2.00-3 Li/Li ⁺ (100)/0.1 Ag ⁻¹ 1.00.3 Li/Li ⁺ (100)/0.1 Ag ⁻¹ ZnCo ₂ O ₄ (BNC 2.00-3 Li/Li ⁺ (100)/0.1 Ag ⁻¹ 1.00.3 Li/Li ⁺ (100)/0.1 Ag ⁻¹ ZnCo ₂ O ₄ (BNC 2.00-3 Li/Li ⁺ (100)/0.1 Ag ⁻¹ 1.00.2 Li/Li ⁺ (100)/0.1 Ag ⁻¹ ZnCo ₂ O ₄ (BNC 2.00-3 Li/Li ⁺ (100)/0.1 Ag ⁻¹ 1.00.2 Li/Li ⁺ (100)/0.1 Ag ⁻¹ ZnCo ₂ O ₄ (BNC 3.15 0.01-3 Li/Li ⁺ (100)/0.1 Ag ⁻¹ ZnCo ₂ O ₄ (BCSA) _A -B 1.656.34 0.01-3 Li/Li ⁺ (100)/0.1 Ag ⁻¹ ZnCo ₂ O ₄ (BCCo ₂ O ₄ nanowires 2.247 0.01-3 Li/Li ⁺ (100)/0.1 Ag ⁻¹ ZnCo ₂ O ₄ (BCCo ₂ O ₄ nanowires 2.247 0.01-3 Li/Li ⁺ (100)/0.0 mAg ⁻¹ ZnCo ₂ O ₄ (BCCo ₂ O ₄ nanowires 2.247 0.01-3 Li/Li ⁺ (100)/0.0 mAg ⁻¹ ZnCo ₂ O ₄ (BCCo ₂ O ₄ nanowires 2.247 0.01-3 Li/Li ⁺ (100)/0.0 mAg ⁻¹ Neckley (100) (100 mAg ⁻¹ marco marco marco mar			ZnCo ₂ O ₄ /CNT microflowers	1300	$0.01-3 \text{ Li/Li}^{+}$	$1200 (120)/200 \text{ mA g}^{-1}$	1	129
$ \begin{array}{cccccccccccccccccccccccccccccccccccc$			$\mathrm{ZnCo_2O_4/ZnO/C}$	1589	$0.005-3 \text{ Li/Li}^{+}$	$800 (400)/1 \mathrm{Ag^{-1}}$	1	201
			ZnCo_2O_4 -C	1521.9	$0.01-3 \text{ Li/Li}^{+}$	$622.5 (1000)/4 \text{ A g}^{-1}$	1	202
$ \begin{array}{cccccccccccccccccccccccccccccccccccc$			$\mathrm{ZnCo_2O_4/C}$	1703.7	$0.01-3 \text{ Li/Li}^{+}$	\sim 760.3 (100)/0.1C	1	203
			ZnCo ₂ O ₄ /C microhydrangea	1418.1	$0.01-3 \text{ Li/Li}^{+}$	$704.4 (1000)/4 \text{ A g}^{-1}$	1	204
Porous ZnCo ₂ O ₄ /C nanofibers 1707 0.01-3 Li/Li ⁺ 1145 (100)/0.1 A g^{-1} 2nCo ₂ O ₄ @NC polyhedrons 1592.1 0.01-3 Li/Li ⁺ 1145 (100)/0.1 A g^{-1} 1082 (300)/0.1 A g^{-1} 2nCo ₂ O ₄ @NC polyhedrons 1592.1 0.01-3 Li/Li ⁺ 146.6 (100)/0.2 A g^{-1} 2nCo ₂ O ₄ @NC Cabon-coated ZnCo ₂ O ₄ nanowires 1551.4 0.01-3 Li/Li ⁺ 787.2 (150)/100 mA g^{-1} 2nCo ₂ O ₄ O ₅ CSF (300)/0.2 A g^{-1} 2nCo ₂ O ₄ O ₅ CSF (300)/0.2 A g^{-1} 2nCo ₂ O ₄ O ₅ CSF (300)/0.2 A g^{-1} 2nCo ₂ O ₄ O ₅ CSF (300)/0.2 manothess 2247 0.01-3 Li/Li ⁺ 778 (100)/100 mA g^{-1} Ni-substituted ZnCo ₂ O ₄ nanoparticles 1312 0.01-3 Li/Li ⁺ 770 (100)/10 mA g^{-1} Ni-substituted ZnCo ₂ O ₄ nanoparticles 1025 0.01-3 Li/Li ⁺ 616 (900)/1 A g^{-1} Ni-doped ZnCo ₂ O ₄ nanowires 2nCo ₂ O ₄ nanowheets 2nCo ₂ O ₄ nanosheets 2nCo ₂ O ₄			ZnCo ₂ O ₄ /C@carbon fibers	733	$0.0-3 \text{ Li/Li}^+$	$463 (100)/50 \text{ mA g}^{-1}$	1	205
$ \begin{array}{cccccccccccccccccccccccccccccccccccc$			Porous ZnCo ₂ O ₄ /C nanofibers	1707	$0.01-3 \text{ Li/Li}^{+}$	$1145(100)/0.1 \text{ A g}^{-1}$	1	206
			ZnCo ₂ O ₄ @NC polyhedrons	1495	$0.01-3 \text{ Li/Li}^{+}$	$1082 (300)/0.1 \text{ A g}^{-1}$	1	207
Carbon-coated ZnCo ₂ O ₄ nanowires 1951.4 0.01-3 Li/Li ⁺ 886.4 (100)/200 mÅ g ⁻¹ PAN-CF/ZnCo ₂ O ₄ anountees 1957.2 0.01-3 Li/Li ⁺ 787.2 (150)/100 mÅ g ⁻¹ 2nCo ₂ O ₄ /GSF (3N ₄ -B) 1636.34 0.01-3 Li/Li ⁺ 778 (100)/100 mÅ g ⁻¹ April carbon/ZnCo ₂ O ₄ nanotubes 2247 0.01-3 Li/Li ⁺ 778 (100)/100 mÅ g ⁻¹ 1312 0.01-3 Li/Li ⁺ 778 (100)/100 mÅ g ⁻¹ 100 co ₂ O ₄ /GSF (2N ₂ O ₂ O ₄ nanoparticles 1312 0.01-3 Li/Li ⁺ 778 (100)/100 mÅ g ⁻¹ 100 co ₂ O ₄ /Micl ₂ -xF _x hydrate 1007 0.01-3 Li/Li ⁺ 700 (1000)/1 A g ⁻¹ 100 co ₂ O ₄ nanoparticles 1005 0.01-3 Li/Li ⁺ 700 (1000)/1 A g ⁻¹ 100 co ₂ O ₄ nanoshetes 2180 0.01-3 Li/Li ⁺ 616 (100)/10 mÅ g ⁻¹ 2nCo ₂ O ₄ nanoshetes 2180 0.01-2.5 Na/Na ⁺ 310 (100)/100 mÅ g ⁻¹ 2nCo ₂ O ₄ nanoshetes 350 0.01-2.5 Na/Na ⁺ 310 (100)/100 mÅ g ⁻¹ 2nCo ₂ O ₄ nanoshetes 210 co ₂ O ₃ spheres/GO 827.7 0.01-3 Na/Na ⁺ 134 (300)/100 mÅ g ⁻¹ 2nCo ₂ O ₃ O ₄ (GO) co ₃ O ₄ (GO) 60 co ₂ O ₃ (GO) 60 co ₃ O ₄ O ₄ O ₅ O ₄ O ₄ O ₄ O ₅ O ₄ O ₅ O ₄ O ₅ O ₄ O ₅ O ₅ O ₄ O ₅			$\mathrm{ZnCo_2O_4@NC}$	1592.1	$0.01-3 \text{ Li/Li}^{+}$	$1146.6 (100)/0.5 \text{ Å g}^{-1}$	1	208
$ \begin{array}{cccccccccccccccccccccccccccccccccccc$			Carbon-coated ZnCo ₂ O ₄ nanowires	1951.4	$0.01-3 \text{ Li/Li}^{+}$	$886.4 (100)/200 \text{ mA g}^{-1}$	1	209
$ \begin{array}{cccccccccccccccccccccccccccccccccccc$			PAN-CF/ZnCo ₂ O ₄	927.2	$0.01-3 \text{ Li/Li}^{+}$	787.2 $(150)/100 \text{ mA g}^{-1}$	1	210
$ \begin{array}{cccccccccccccccccccccccccccccccccccc$			$\mathrm{ZnCo_2O_4@C_3N_4-B}$	1636.34	$0.01-3 \text{ Li/Li}^{+}$	919.76 $(500)/0.2 \text{ A g}^{-1}$	97.8%/1000 cycles	211
$ \begin{array}{cccccccccccccccccccccccccccccccccccc$			${ m ZnCo_2O_4/CSF}$	3164	$0.01-3 \text{ Li/Li}^{+}$	778 $(100)/100 \text{ mA g}^{-1}$		212
$ \begin{array}{cccccccccccccccccccccccccccccccccccc$			Hybrid carbon/ZnCo ₂ O ₄ nanotubes	2247	$0.01-3 \text{ Li/Li}^{+}$	$494 (600)/5 \text{ A g}^{-1}$	75%/600 cycles	213
Ni-substituted ZnCo ₂ O ₄ nanograins 1067 0.01–3 Li/Li [†] 386 (100)/1 A g ⁻¹ N-doped ZnCo ₂ O ₄ nanoparticles 1025 0.01–3 Li/Li [†] 650 (100)/1 C ZnCo ₂ O ₄ @Ag hollow spheres 830 0.01–3 Li/Li [†] 616 (900)/1 A g ⁻¹ ZnCo ₂ O ₄ nanowires ~ 1180 0.01–2.5 Na/Na [†] 70.8 (100)/100 mA g ⁻¹ ZnCo ₂ O ₄ nanosheets 350 0.01–2.5 Na/Na [†] 191.9 (100)/200 mA g ⁻¹ ZnCo ₂ O ₄ nanosheets 800 0.01–3 Na/Na [†] 310 (100)/200 mA g ⁻¹ ZnCo ₂ O ₄ nanosheets 800 0.01–3 Na/Na [†] 463 (60)/1.1 A g ⁻¹ Composites with Yolk–shell ZnCo ₂ O ₄ spheres/rGO 827.7 0.01–3 Na/Na [†] 280 (100)/1.0 nA g ⁻¹ ZnCo ₂ O ₄ @GO 569		Other strategies	$ZnCo_2O_4/NiCl_{2-x}F_x$ hydrate	1312	$0.01-3 \text{ Li/Li}^{+}$	$700(1000)/1~{ m Ag}^{-1}$		214
$ \begin{array}{cccccccccccccccccccccccccccccccccccc$			Ni-substituted ZnCo ₂ O ₄ nanograins	1067	$0.01-3 \text{ Li/Li}^{+}$	$386 (100)/1 \text{ A g}^{-1}$	68%/100 cycles	215
$ \begin{array}{cccccccccccccccccccccccccccccccccccc$			N-doped ZnCo ₂ O ₄ nanoparticles	1025	$0.01-3 \text{ Li/Li}^{+}$	650 (100)/1C	63%/100 cycles	216
$\begin{array}{cccccccccccccccccccccccccccccccccccc$			ZnCo ₂ O ₄ @Ag hollow spheres	830	$0.01-3 \text{ Li/Li}^{+}$	$616 (900)/1 \text{ A g}^{-1}$		217
$ \begin{array}{llllllllllllllllllllllllllllllllllll$	u	Pristine	ZnCo ₂ O ₄ nanowires	~ 1180	$0.01-2.5 \text{ Na/Na}^{+}$	$70.8 (100)/100 \text{ mA g}^{-1}$		218
Zn _x Co ₂ -xO ₄ hollow nanoboxes 350 0.01–3 Na/Na ⁺ 310 (100)/200 mA g ⁻¹ ZnCo ₂ O ₄ nanosheets 415.1 0.01–3 Na/Na ⁺ 330 (100)/100 mA g ⁻¹ ZnCo ₂ O ₄ nanosheets 800 0.01–3 Na/Na ⁺ 463 (60)/0.1 A g ⁻¹ ZnCo ₂ O ₄ spheres/rGO 827.7 0.01–3 Na/Na ⁺ 280 (1000)/1.0 A g ⁻¹ ZnCo ₂ O ₄ grid 200/100 mA g ⁻¹ ZnCo ₂ O ₄ grid 200/100 mA g ⁻¹ ZnCo ₂ O ₄ grid 200/100 mA g ⁻¹ ZnCo ₂ O ₄ grid 200/100 mA g ⁻¹ ZnCo ₂ O ₄ grid 200/100 mA g ⁻¹			$ZnCo_2O_4$ nanosheets	\sim 1150	$0.01-2.5 \text{ Na/Na}^{+}$	$191.9 (100)/100 \mathrm{\ mA\ g}^{-1}$		218
ZnCo ₂ O ₄ nanosheets 415.1 0.01–3 Na/Na ⁺ 3 ZnCo ₂ O ₄ nanosheets 800 0.01–3 Na/Na ⁺ 2 Yolk–shell ZnCo ₂ O ₄ spheres/rGO 827.7 0.01–3 Na/Na ⁺ 2 ZnCo ₂ O ₄ @rGO 601–3 Na/Na ⁺ 2 2 ZnCo ₂ O ₄ (RrGO 569.3 0.01–3 Na/Na ⁺ 1			Zn _x Co _{3-x} O ₄ hollow nanoboxes	350	0.01-3 Na/Na ⁺	$310~(100)/200~{ m mA~g}^{-1}$	90.4%/100 cycles	155
ZnCo ₂ O ₄ nanosheets 800 0.01–3 Na/Na $^+$ Yolk–shell ZnCo ₂ O ₄ spheres/rGO 827.7 0.01–3 Na/Na $^+$ ZnCo ₂ O ₄ @rGO 407 0.01–3 Na/Na $^+$ ZnCo ₂ O ₄ ($^-$ Co ₂ O ₃ ($^-$ Co ₂ O ₃ ($^-$ Co ₃ O ₃ O ₄ CO 569.3 0.01–3 Na/Na $^+$ ZnCo ₂ O ₃ O ₄ CO			ZnCo ₂ O ₄ nanosheets	415.1	$0.01-3 \text{ Na/Na}^{+}$	$330 (100)/100 \text{ mA g}^{-1}$	1	219
Yolk-shell ZnCo ₂ O ₄ spheres/rGO 827.7 0.01–3 Na/Na ⁺ ZnCo ₂ O ₄ @rGO 407 0.01–3 Na/Na ⁺ ZnCo ₂ O ₄ (RO 569.3 0.01–3 N			ZnCo ₂ O ₄ nanosheets	800	$0.01-3 \text{ Na/Na}^+$	$463 (60)/0.1 \mathrm{Ag^{-1}}$	1	219
ZnCo ₂ O ₄ @rGO 407 0.01–3 Na/Na ⁺ ZnCo ₂ O ₄ (RtO 569.3 0.01–3 Na/Na ⁺		Composites with	No2O4 spheres	827.7	$0.01-3 \text{ Na/Na}^{+}$	$280 (1000)/1.0 \text{ A g}^{-1}$	1	187
569.3 0.01–3 Na/Na ⁺		carbon materials	$\mathrm{ZnCo_2O_4}$ (a) rGO	407	$0.01-3 \text{ Na/Na}^+$	$134 (300)/100 \text{ mA g}^{-1}$		220
מינים			$ZnCo_2O_4/rGO$	569.3	0.01-3 Na/Na ⁺	$101.7 (500)/1000 \text{ mA g}^{-1}$	1	221

CC: carbon cloth, CF: carbon fiber, CNTs: carbon nanotubes, CSF: carbonized silk fabric, NC: N-doped carbon, NF: nickel foam, PAN: polyaniline, rGO: reduced graphene oxide.

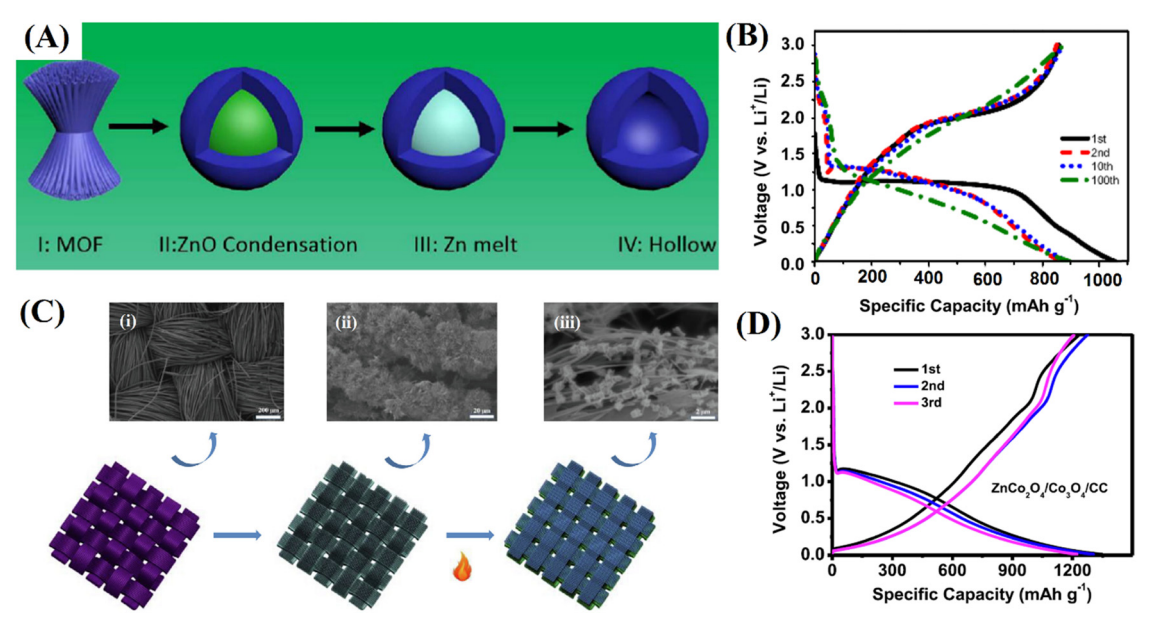


Fig. 15 (A) Schematic representation of the formation process of the hollow structure. (I) ZnCo MOF growth; (II) ZnO condensation to the middle of the pyrolyzed particle; (III) Zn reduction and melt from the middle; and (IV) hollow Co_3O_4 doped with $ZnCo_2O_4$ after losing Zn. (B) Charge/discharge curves of hollow Co₃O₄/ZnCo₂O₄ spheres at 0.1 A g⁻¹. Reproduced with permission.¹⁷⁹ Copyright © 2018 Published by Elsevier B.V. (C) Schematic illustration of discharge curves at a current density of 0.1 A g⁻¹ Reproduced with permission. To Copyright © 2020 Elsevier B.V. All rights reserved.

From the perspective of material application, an energy storage device balances the power supply and demand of large-grid energy storage. Several factors can be addressed to evaluate the performance of an electrode material in a battery cell, such as first discharge, stability, reversible capacity and the potential window. Among the many types of ZnCo₂O₄ materials previously shown, we summarize in Fig. 17 the electrodes with the 10 biggest first discharge. The best one is the ZnCo₂O₄/ carbonized silk fabric (CSF) (3164 mA h g⁻¹); the high initial discharge of this material is endowed by the hydrothermal method that improves the bonding between active materials and the flexible substrate, and avoids capacity reduction from the active substance detaching from the substrate during the charge and discharge cycle; the unique weave structure of the CSF gives it good mechanical flexibility and the 3D network structure of the CSF provides a fast electron transport path to enhance the composite material's energy storage performance.212

Nine out of the top ten anode materials demonstrate the benefits of a nanocomposite based on ZnCo₂O₄/carbon nanomaterials. Use of these nanocomposites was shown to be a remarkable strategy to improve the electrochemical performance of anode electrodes, as the carbon nanomaterials have many great electrochemical abilities, including enhancing the electrical conductivity of the electrode and preventing the volume change and aggregation found with ZnCo₂O₄ electrodes. The second (ZnCo₂O₄@CNTs, 2553 mA h g^{-1}), 200 seventh $(C/ZnCo_2O_4/CNT, 1947.1 \text{ mA h } g^{-1})^{199} \text{ and ninth } (ZnCo_2O_4/CNT, 1947.1 mA h } g^{-1})^{199}$ ZnO/CNT, 1893 mA h g⁻¹)¹⁹⁸ materials with the best performances demonstrate the advantages due to the presence of carbon nanotubes; this can be attributed to the efficient electron transport and CNT network, which could shorten the diffusion pathway of lithium-ions and buffer the volume expansion/constriction, as well as enlarge the surface area for more electrochemically active species.²⁰⁹ Likewise, the tenth $(ZnCo_2O_4@CC, 1886.2 \text{ mA h g}^{-1})$, 196 eighth $(ZnCo_2O_4$ graphene, 1937 mA h g⁻¹), 194 sixth (carbon-coated ZnCo₂O₄ nanowires, 1951.4 mA h g⁻¹), ²⁰⁹ fifth (ZnCo₂O₄@3D graphene film@Ni foam, 2024 mA h g⁻¹)¹⁹¹ and third (hybrid carbon/ ZnCo₂O₄ nanotubes, 2247 mA h g⁻¹)²¹³ best materials demonstrate improved electrochemical performance, which may be assigned to the carbon nanomaterial structure, which can enlarge the electrode-electrolyte contact area, greatly strengthen the electroconductivity and structural stability and improve the energy density.

It's worth highlighting that the second, seventh and tenth best materials mentioned above are based on MOF-derived materials. This strategy of preparation of materials has many advantages; for example, it endows the materials with large specific area, regular porosity, shearing capability and topological diversity, which can demonstrate that the best electrochemical performance is associated with the effects of the preparation method and the electrode architecture.230 The fourth (ZnCo₂O₄ nanoribbons, 2161 mA h g⁻¹)⁸¹ best material had its highlighted role due to its unique morphology, as well as the tenth best materials. In fact, the size of nanostructures of ZnCo₂O₄ provided more active sites, large surface area and shorter diffusion paths for ions and electrons, bringing remarkable enhancement in their electrochemical performance.81,196

In summary, ZnCo₂O₄ with excellent electrochemical performance should have nanostructures or a unique morphology or be associated with a carbon nanomaterial as a nanocomposite.

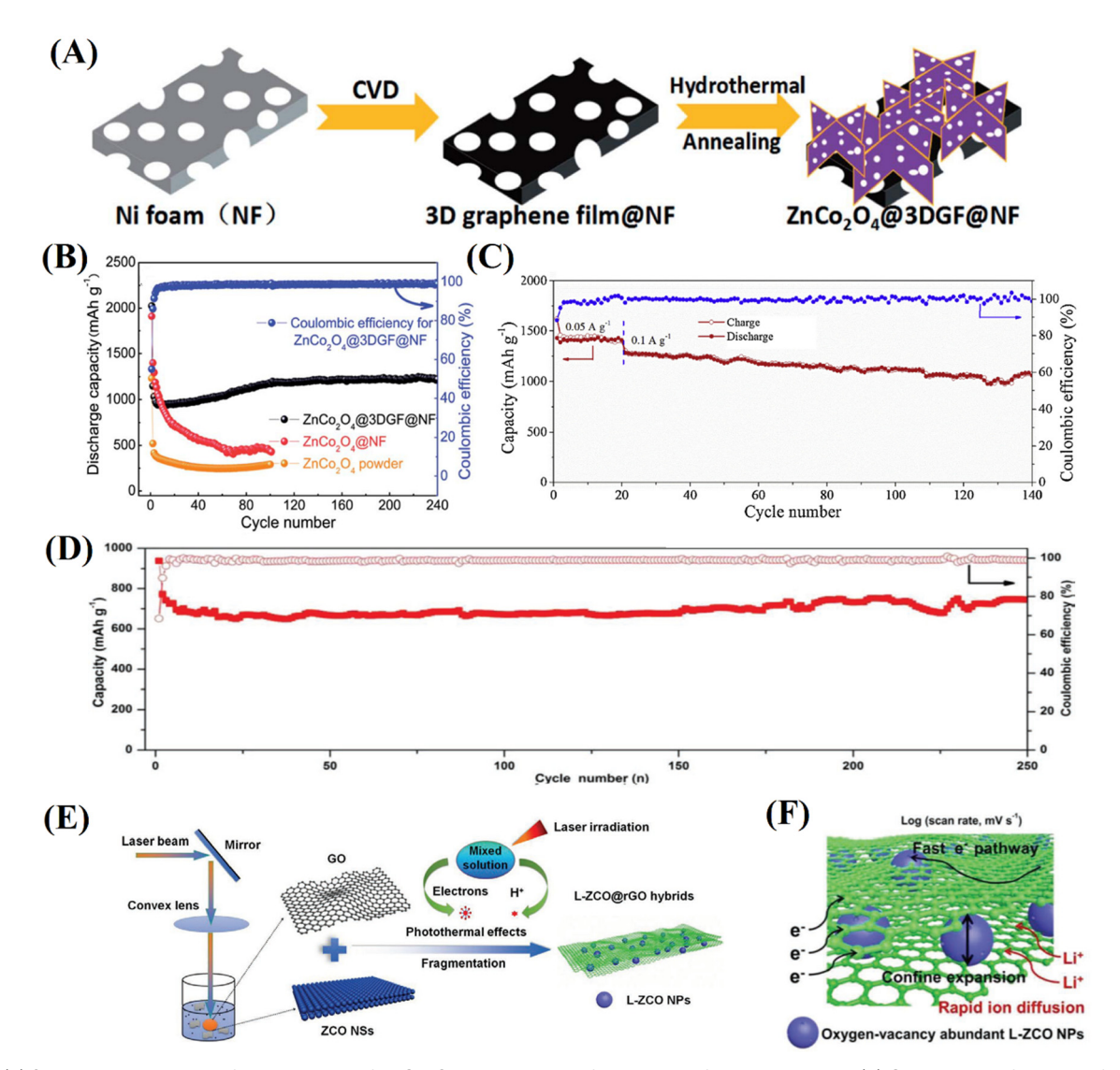


Fig. 16 (A) Schematic illustration of the synthesis of ZnCo₂O₄@3D graphene foam@nickel foam composites. (B) Comparison of cycle performance of the $ZnCo_2O_4$ @3DGF@NF, $ZnCo_2O_4$ @NF, and $ZnCo_2O_4$ powder electrodes at a current density of 500 mA g^{-1} . Reproduced with permission. 191 CC BY-NC 3.0. Royal Society of Chemistry. (C) Cycling capacity of the ZCO@rGO//LiCoO2 full cell at a current density of 100 mA g⁻¹. Reproduced with permission. 188 Copyright $^{\circ}$ 2018 Elsevier Ltd. All rights reserved. (D) Cycling performance and coulombic efficiency data at 1.0 A g $^{-1}$ of L-ZCO@rGO-30. (E) The schematic diagram for the formation of L-ZCO@rGO hybrids. (F) Schematic illustration of the fast electron/ion transfer and rapid electrochemical kinetics of the L-ZCO@rGO-30 electrode. Reproduced with permission. 192 Copyright © 2020 Wiley-VCH Verlag GmbH & Co. KGaA, Weinheim.

These improved electrochemical performance can be attribute to the greater number of electrochemically active sites, the high surface area, a good diffusion length of ions and electrons, and a satisfactory volume expansion from the insertion/extraction of Li ions.

3.2.2. Other metal ion batteries. Sodium-ion batteries (SIBs), as appropriate energy storage systems for large-scale applications, have gained a lot of attention as alternative energy storage technologies to LIBs, due to abundant sodium resources and their low cost. 49,231 As previously reported for LIBs, ZnCo₂O₄based materials are attractive candidates as SIB anode materials due to their low cost, high theoretical specific capacity, high specific surface area, and fast ion-diffusion. 219,220,232 ZnCo₂O₄ nanowires and nanosheets as SIB electrode materials were studied by Zhao and collaborators. 209 They prepared ZnCo2O4 nanosheets and nanowires aiming for electrochemical applications. Results indicated that ZnCo₂O₄ nanosheet and nanowire anodes achieved 191.9 mA h g^{-1} and 70.8 mA h g^{-1} after 100 cycles at 100 mA g^{-1} respectively. Recently, materials obtained by other strategies have been considered for application as anode materials; for example, Yang et al.220 prepared a polyhedron ZnCo2O4 anchored onto rGO nanosheets via the hydrothermal method. This composite electrode displays good cycling performance, with a discharge capacity of 134 mA h g⁻¹ after 300 cycles. To improve capacity over cycles, Zhang et al. 187 designed novel yolk-shell structured ZnCo₂O₄ spheres anchored onto rGO sheets. This unique structure provides superior properties with an initial discharge capacity of 827.7 mA h g^{-1} and a reversible capacity of 280 mA h g^{-1} at 1.0 A g^{-1} after 1000 cycles. Table 6 summarizes the electrochemical performance of electrodes with different materials, coupled with distinct types of anodes based on ZnCo2O4.

Energy Advances Review

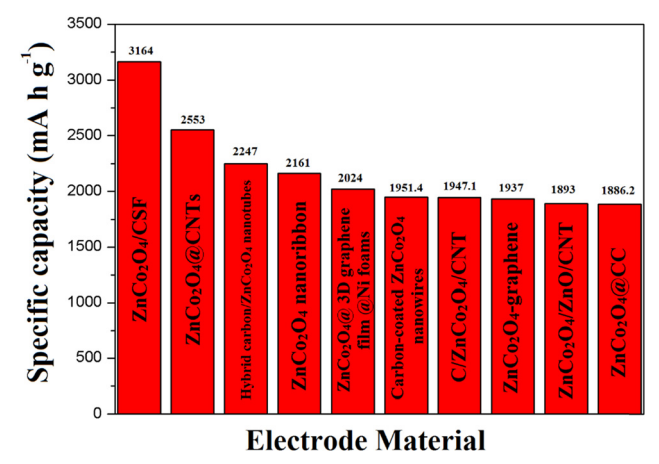


Fig. 17 The ZnCo₂O₄ electrode materials with the top 10 highest first specific capacity in LIBs

In addition to SIBs, Zn-ion and Mg-ion batteries afford some attributes required of an alternative energy storage technology, such as nondendritic formations, Zn and Mg metal anode material delivers a high capacity of 820 mA g⁻¹ and 2205 mA h g⁻¹ respectively, and abundant and non-toxic raw materials. 233,234 Recently, ZnCo₂O₄ structures have been developed as potential cathode materials for these types of batteries. Baby et al.235 reported the synthesis of a ZnMnCoO4 cathode material with the first discharge of 109.4 mA h g⁻¹ in Zn-ion batteries, whereas Shimokawa et al. 236 reported the synthesis of ZnCo₂O₄ used as a cathode material for rechargeable magnesium batteries with a discharge capacity in the first cycle of ~ 100 mA h g⁻¹.

3.2.3. Lithium-sulfur batteries. To replace current LIBs, lithium-sulfur (Li-S) batteries are considered to be the most potential energy storage systems due to the high theoretical specific capacity (1675 mA h g⁻¹) and high specific energy (2600 W h kg⁻¹) of the sulfur cathode. ²³⁷⁻²⁴¹ Owing to their well-defined crystallinity and high porosity, mixed transition metal oxides are regarded as perfect selections for cathode materials, and the interstitial spaces surrounded by the octahedra interconnect into three dimensions, accommodating guest ions, i.e., lithium ions.242-244 To explore the potentiality of ZnCo₂O₄ as a Li-S electrode material, Sun et al. 242 synthesized ZnCo2O4 porous particles anchored on N-doped rGO via the combined procedures of refluxing and hydrothermal treatment. ZnCo₂O₄@N-rGO when used as a cathode material for Li-S achieved 1332 mA h g⁻¹, which was maintained at 720 mA h g⁻¹ after 200 cycles. Meanwhile, Zhang and colleagues²⁴⁵ also constructed a ZnCo₂O₄-based material and researched its Li-S storage behavior. This material showed a specific capacity of 466 mA h g⁻¹ at 0.3C and 413 mA h g⁻¹ at 0.5C after 200 cycles. Yeon et al.243 synthesized a 2D spinel ZnCo₂O₄. When performing the electrochemical measurement, this material presented a high initial discharge of 1292.2 mA h g⁻¹ at 0.1C and a capacity retention of 84% (1C) and 86% (2C) even after 800 cycles.

3.2.4. Metal-air batteries. Metal-air batteries (MABs) such as lithium-air, iron-air, zinc-air, aluminum-air, and magnesium-air

batteries are considered to be the next-generation technology because they use oxygen from the air as the cathode, freeing up more space devoted to energy storage.246-249 The exceptional theoretical energy density of MABs (3505 W h kg⁻¹ for Li-O₂ batteries and 1086 W h kg $^{-1}$ for Zn-air batteries) 237 is based on the oxygen evolution reaction (OER) and oxygen reduction reaction (ORR); in this way, these devices have been studied by several researchers, including oxygen electrode catalysts with special structures for use in rechargeable metal-air batteries. 250 Among the oxygen electrode catalysts, spinel transition metal oxides such as MCo₂O₄ are potential cathode materials due to the abundance of the necessary raw material and the high electrocatalytic activity for the OER and ORR. ZnCo2O4 has been widely studied as a catalytic oxygen electrode material for MABs such as lithium-air batteries^{55,251} and zinc-air batteries.²⁵²⁻²⁵⁵ Kin et al.²⁵¹ fabricated highly mesoporous ZnCo2O4 nanofibers by simple electrospinning and used them as a cathode material in the lithium-oxygen battery. The ZnCo₂O₄ nanofiber electrode displayed excellent electrocatalytic activity and cycling stability (226 cycles with a capacity limit of 1000 mA h g^{-1} at 500 mA g^{-1}). Mai et al.²⁵³ reported a catalyst with ZnCo₂O₄ submicron/nanospheres with Co_xSe_v nanosheets, which exhibited promising catalytic properties towards OER activity with an overpotential of 324 mV at 10 mA cm⁻² in 1 M KOH. In the homemade Zn-air battery test, the cathode showed a small voltage gap (0.98 V at 50 mA cm⁻²), high power density (212.9 mW cm⁻²) (Fig. 18A) and high specific capacity (570.1 mA h g⁻¹). Costa and co-workers²⁵² documented the fabrication of a novel W-Co oxide bifunctional catalyst for the air electrode in Zn-air batteries. The conformal layer of W-Co oxide was transformed into cubic spinel ZnCo2O4 nanoparticles which provided excellent bifunctional catalytic activity and a good performance in the Zn-air battery test with a maximum power density of 216.4 mW cm^{-2} (Fig. 18B).

To improve catalyst performance, composite materials have been synthesized and used as catalysts in both the ORR and OER. Generally, metal oxides combined with carbon materials such as graphene and carbon nanotubes (CNTs) can not only improve the conductivity of the catalyst but also increase the specific surface area and improve electrochemical stability. 254-257 Combining Co/ZnCo2O4 with N-doped carbon microplates interwoven with CNTs, Yan et al. 255 developed a Co/ZnCo₂O₄(a)NC-CNTbased flexible solid-state Zn-air battery with a competitive power density of 151 mW cm⁻² at 50 mA cm⁻² (Fig. 18C), robust flexibility and integrality. Xu et al. 254 prepared ZnCo2O4/CNTs by inserting zinc ions. When used as a cathode material in a rechargeable Zn-air battery, this material exhibits a power density of 249.4 mW cm⁻², and a charge-discharge durability of 240 cycles.

4. ZnCo₂O₄-based electrocatalysts for energy conversion and storage applications

4.1. ORR electrocatalysts in energy storage

As mentioned in the previous topic, both the oxygen reduction and oxygen evolution reactions (ORR/OER) play an important

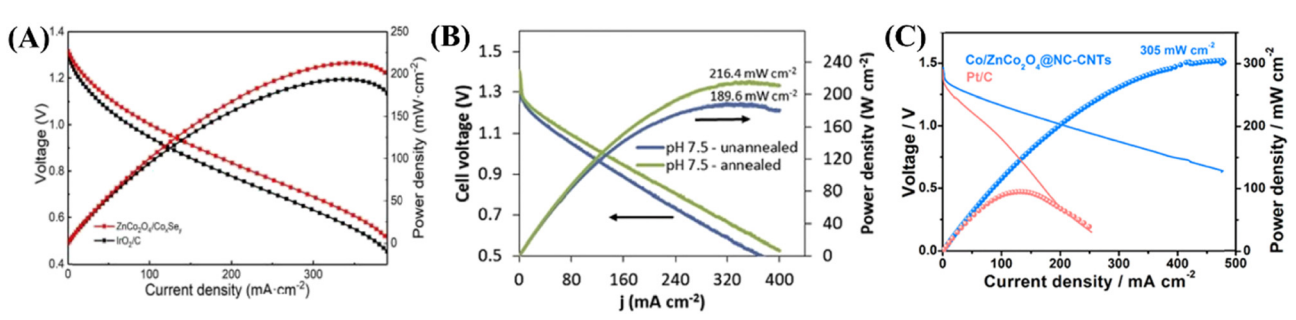


Fig. 18 Discharge polarization curves and the corresponding power density plots of a battery based on (A) ZnCo₂O₄/Co_xSe_y and IrO₂/C (Reproduced with permission.²⁵³ Copyright MarketplaceTM. Royal Society of Chemistry), (B) annealed and unannealed W-Co oxide electrodes (Reproduced with permission. 252 Copyright © 2020 Hydrogen Energy Publications LLC. Published by Elsevier Ltd. All rights reserved) and (C) Pt/C and Co/ZnCo₂O₄@NC-CNTs (Reproduced with permission.²⁵⁵ Copyright © 2020 Elsevier Ltd. All rights reserved).

role in the electrochemical energy conversion process, not only in metal-air rechargeable batteries but also in fuel cells.²⁵⁸ In fact, because of their high associated activation energies, such reactions are usually sluggish and require catalysts to enhance the kinetics.²³⁵ In this sense, great efforts have been directed towards the development of inexpensive, efficient, noble metal-free and stable electrocatalysts for next-generation sustainable energy technologies. 258 Thus, ZnCo₂O₄ and its composites show great potential as electrocatalysts due to their high intrinsic activity, 259 and in many cases exhibit both ORR and OER activity simultaneously.

As shown in Table 7, despite being considered as very promising electrocatalysts, less than two dozen ZnCo₂O₄based materials have been reported in the past 5 years for application in the ORR, indicating that these materials are still to be explored, especially in the design of bifunctional electrocatalysts. However, some improvement strategies for these materials can be highlighted, as a guide for future research. For instance, many catalysts with different morphologies such as nanosheets, 130,260 flower like structures 130 and nearspherical particles²³⁵ have been recently reported.

In one of these studies, Chakrabarty et al. 261 synthesized a flower-like porous ZnCo2O4 microstructure by the one-step solvothermal method, as confirmed by SEM and HRTEM images (Fig. 19A and B). The ZnCo₂O₄ microstructure achieves a nearly 4-electron assisted oxygen reduction ($n \approx 3.4$) with onset and half wave potentials observed at 0.81 V and 0.75 V vs. RHE (Table 7). It is important to highlight that despite the interesting results obtained by designing the morphology of ZnCo₂O₄ nanostructures, better results are clearly improved by the formation of composites, especially by combining them with conductive carbonaceous materials. For example, Chakrabarty et al.²⁶¹ also showed the activity of electrocatalysts predated by the simultaneous growth of ZnCo2O4 and reduction of GO (Fig. 19D), achieving a more positive ORR onset potential (0.95 V vs. RHE) with higher cathodic peak current density compared to $ZnCo_2O_4$ and $n \approx 3.95$, demonstrating that the presence of a conductive matrix is essential in the design of high-performance electrocatalysts. Furthermore, the bifunctional electroactivity of the rGO-ZnCo2O4 and ZnCo2O4 was determined from the potential difference (ΔE) between the OER $(E_{OER}, \text{ at } 10 \text{ mA cm}^{-2}) \text{ and ORR } (E_{ORR}, \text{ at } -3 \text{ mA cm}^{-2}).$ The ΔE for rGO-ZnCo₂O₄ was 0.679 V vs. RHE (Fig. 19C), which is less than that obtained using ZnCo₂O₄ (0.944 V vs. RHE), demonstrating the synergistic effect achieved by increasing the catalytic surface area and efficient electron transfer through the RGO sheet in the composite catalyst.²⁶¹

Employing a similar strategy, Yan and coworkers²⁵⁵ reported the preparation of a 3D bifunctional oxygen electrocatalyst based on Co/ZnCo₂O₄ nanoparticles derived from CoZn-ZIF-L sandwiched in leaf-like nitrogen-doped carbon microplates interwoven with carbon nanotubes (Co/ZnCo₂O₄@NC-CNTs, Fig. 20A), as confirmed by the SEM images in Fig. 20B and C and TEM images in Fig. 20D and E. As shown in Table 7, the Co/ZnCo₂O₄@NC-CNT material is among the best bifunctional electrocatalysts as revealed by its excellent onset potential of 1.01 V, $E_{1/2}$ of 0.90 V, Tafel slope of 91 mV dec⁻¹, limiting current density of 4.6 mA cm $^{-2}$ for the ORR and small ΔE of 0.70 V for ORR/OER activities. The excellent activity of this composite is due to the large amount of metal- N_x and Co^{3+} active sites as well as the interwoven CNTs on the surfaces of the carbon microplates which are beneficial to the charge transfer in the ORR/OER processes.²⁵⁵

4.2. Water-splitting electrocatalysts for energy conversion (OER and HER)

Electrochemical water-splitting has been considered as a promising method to obtain H2 and O2 through the hydrogen evolution reaction (HER) and the oxygen evolution reaction (OER), respectively. However, the production of H₂ is limited by the sluggish OER kinetics at the anode due to the multielectron transfer coupled with protons, which leads to high overpotentials.264 Benchmark catalysts such as RuO2 and IrO2 have been used in the water-splitting process to overcome this issue. Nevertheless, due to the scarcity and high cost of these noble metals, their commercial implementation has been unfeasible.265 In this sense, it is necessary to search for new electrode materials with low cost, which are not scarce, besides they have a superior electrochemical behavior.

In recent years, cobaltite spinel oxides $M_xCo_{3-x}O_4$ (where M = Ni, Mn, Zn, and Fe) have been used as electrode materials for efficient water oxidation. 61,266,267 Among these electrode

Catalytic activity parameters of recently reported ORR ZnCo₂O₄-based electrocatalysts Table 7

Average $ \begin{array}{ccccccccccccccccccccccccccccccccccc$	12 0.1 M KOH 130	- 1 M KOH 261 - 0.1 M KOH 235		$^{2.77}_{\sim 96\%}$ 0.1 M KOH 262	1.94 h — 0.1 M KOH 235	2000 cycles 0.1 M KOH 254		CVS 87% 0.1 M KOH 255	0.1 M KOH 0.1 M KOH	0.1 M KOH 0.1 M KOH 0.1 M KOH	0.1 M KOH 0.1 M KOH 0.1 M KOH 1 M KOH	0.1 M KOH 0.1 M KOH 0.1 M KOH 1 M KOH 0.1 M KOH	0.1 M KOH 0.1 M KOH 0.1 M KOH 1 M KOH 6 0.1 M KOH
Average electron transfer c^{-1}) number	4.1	3.05–3.4 3.99	3.77-3.95	~ 3.5	3.99	3.89		4.0	4.0	4.0	4.0	4.0 3.7-3.95 3.41	4.0 — 3.7–3.95 3.41
$egin{array}{ll} { m nt} & { m Tafel} \ { m y} & { m slope} \ { m m}^{-1}) & ({ m mV de} \ \end{array}$			I	I	I	I		91	91	91	91	91	91
OER – Current density RHE) (mA cm		2.97	5.6	I	5.22	5.72		4.6	4.6	4.24			
Overpotential Overpotential ΔE , $E_{\rm OER}$ Current $E_{\rm ORR}$ at -3 mA $E_{\rm OER}$ at 10 mA $E_{\rm ORR}$ density cm ⁻¹ (V) (V $\nu_{\rm S}$. RHE) (mA cm ⁻²		0.944	I	I	I			0.70^c	0.70°	0.70¢	0.70°	0.70°	0.70°
Overpotential Overpotential ΔE , $E_{\rm ORR}$ at -3 mA $E_{\rm OER}$ at 10 mA $E_{\rm ORR}$ cm $^{-1}$ (V) $v_{\rm S}$.	0.34	0.41	I	I	I	0.49		0.37	0.37	0.37	0.37	0.37	0.37
		969.0	I	I	I	I			1 1				
$E_{ m ORR}$ onset Half wave potential potential Substrate (V vs. RHE) (V vs. RHE)	1	$\begin{array}{c} 0.75 \\ 0.62^b \end{array}$	I	0.68	0.74^b	0.76	0	0.90	0.90	06:0	0.90	$\begin{array}{cccccccccccccccccccccccccccccccccccc$	$\begin{array}{cccccccccccccccccccccccccccccccccccc$
$E_{ m ORR}$ onset Half potential potential $(V vs. RHE)$ $(V vs. RHE)$	1	$\begin{array}{c} 0.81 \\ 0.83^b \end{array}$	0.8	0.77	0.94^b	0.97	5	1.01	1.01	10.1	1.01	$\begin{array}{c} \\ \\ 0.95 \\ 0.14^a \end{array}$	$\begin{array}{cccccccccccccccccccccccccccccccccccc$
	GCE	GCE	GCE	GCE	GCE	GCE	GCE	1	GCE	GCE	GCE GCE GCE	GCE GCE GCE GCE	GCE GCE GCE GCE
Incorporated material or atom			4 S	ı	Mn	CNTs	NC-CNTs		MC	MC Graphene	MC Graphene RGO	MC Graphene RGO ZnO + C	MC Graphene RGO ZnO + C
ORR catalysts	ZnCo ₂ O ₄ ultrathin	nanosheets Flower like ZnCo ₂ O ₄ Near-spherical	particles of ZnCo ₂ O ₄ ZnCo ₂ O ₄ nanosheets	${ m ZnCo_2O_4~LFs}$	Near-spherical	$ZnCo_2O_4$ -CNTS	Co/ZnCo ₂ O ₂ (a)	\$) # 1 7 1 1 1 1 1 1 1 1 1 1 1 1 1 1 1 1 1	NC-CNTs ZnCo ₂ O ₄ -MC	NC-CNTs ZnCo ₂ O ₄ -MC ZnCo ₂ O ₄ -graphene	NC-CNTS ZnCo ₂ O ₄ -MC ZnCo ₂ O ₄ -graphene rGO-ZnCo ₂ O ₄	NC-CNTS ZnCo ₂ O ₄ -MC ZnCo ₅ O ₄ -graphene rGO-ZnCo ₂ O ₄ ZnO/ZnCo ₂ O ₄ /C	NC-CNTs ZnCo ₂ O ₄ -MC ZnCo ₂ O ₄ -graphene rGO-ZnCo ₂ O ₄ ZnO/ZnCo ₂ O ₄ /C

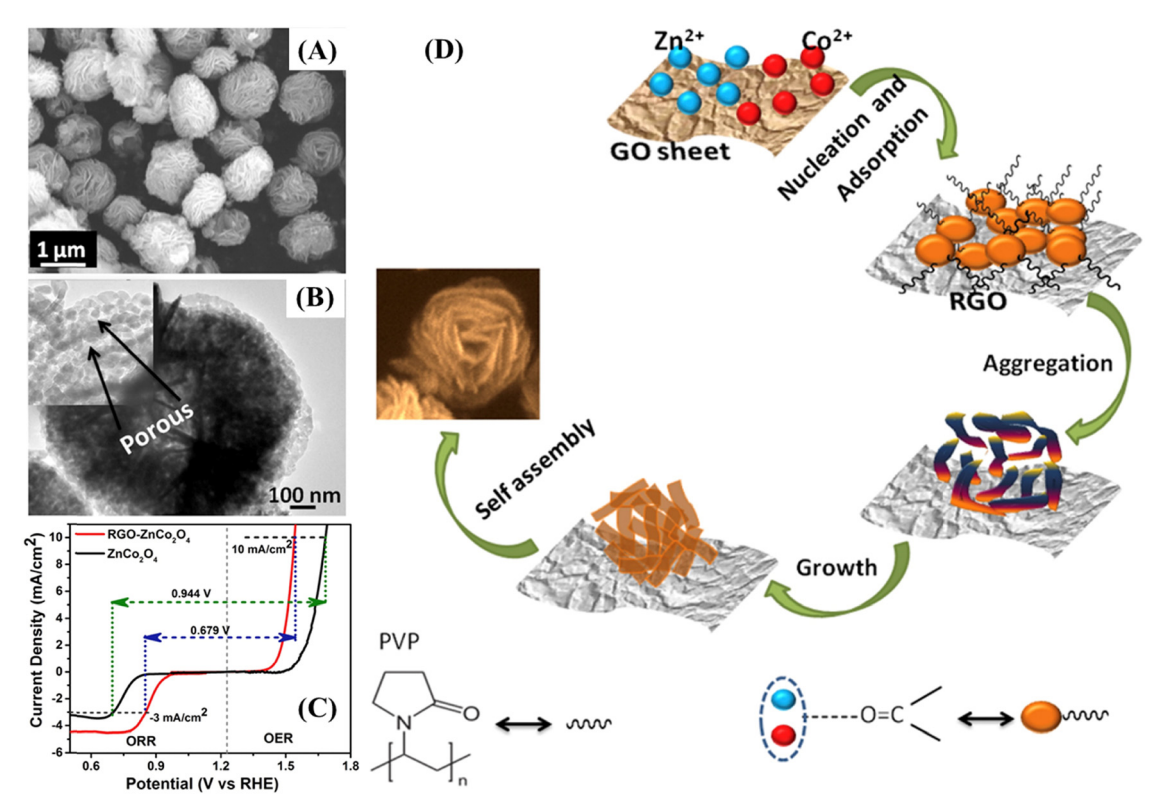


Fig. 19 (A) SEM image of ZnCo₂O₄ microspheres and (B) TEM images of a ZnCo₂O₄ microsphere. The inset of (B) shows the magnified portion of the image that shows the porous structure. (C) Oxygen electrode activities of both the catalysts within the range of potential for the ORR and OER in O2saturated 1 M KOH electrolyte at 1200 rpm. (D) Growth mechanism of rGO-ZnCo₂O₄ flower-like microstructures. Reproduced with permission.²⁶¹ Copyright © 2018 Hydrogen Energy Publications LLC. Published by Elsevier Ltd. All rights reserved.

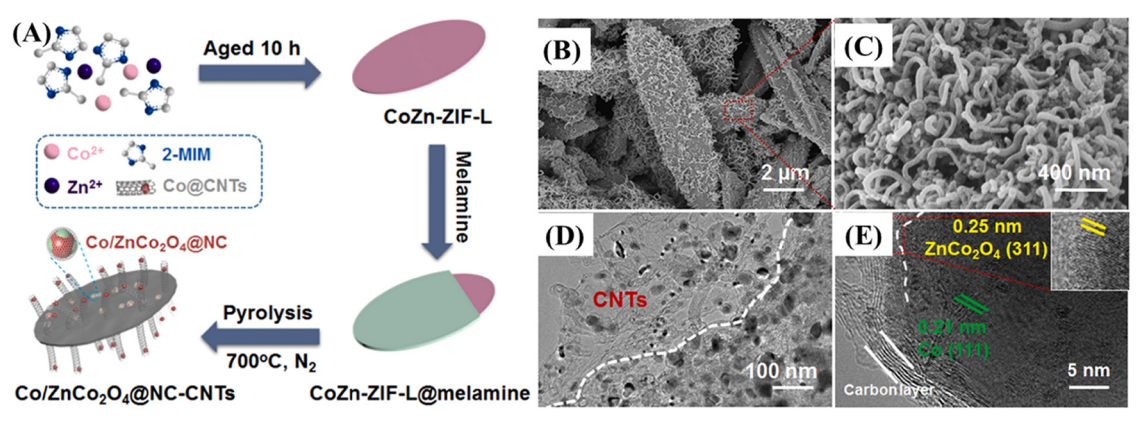


Fig. 20 (A) Schematic synthesis process of the Co/ZnCo₂O₄@NC-CNT electrocatalyst. (B and C) SEM images, (D) TEM image, and (E) HRTEM image of the as-prepared Co/ZnCo₂O₄@NC-CNTs. Reproduced with permission. ²⁵⁵ Copyright © 2020 Elsevier Ltd. All rights reserved.

materials, ZnCo₂O₄ has drawn attention due to its rich redox chemistry, which has led to enhanced electrochemical performance. Indeed, ZnCo₂O₄ presents a better catalytic activity for the OER when compared to other cobaltite spinel oxides, ²⁶⁸ and the reason for this lies in how Zn²⁺ ions replace Co ions in the Co₃O₄ spinel structure.

In the Co₃O₄ spinel structure, Co²⁺ and Co³⁺ ions are found, respectively, in the tetrahedral and octahedral sites. Kim and colleagues²⁶⁹ demonstrated that Zn²⁺, when inserted into the Co₃O₄ spinel structure to form ZnCo₂O₄, only replaces Co²⁺ found in the tetrahedral interstices, leaving Co³⁺ (highly active species for the OER) unchanged in the octahedral sites. Nevertheless, other metal ions like Ni and Mn, when inserted into Co₃O₄ to form NiCo₂O₄ and MnCo₂O₄, respectively, can suppress the catalytic activity for the OER, 261 due to occupation of tetrahedral and octahedral sites in the Co₃O₄ spinel structure. In addition, M. Harada, F. Kotegawa, & M. Kuwa¹⁶ demonstrated that the active sites are controlled by the balance of **Energy Advances** Review

 M^{3+}/M^{2+} cation distribution in O_h and T_d sites and by the bond strength between M and oxygen atoms at the electrocatalyst surface before and after the exposure to OER conditions, where the catalytic activity of the OER decreases in the order of $ZnCo_2O_4 > NiCo_2O_4 > FeCo_2O_4 > Co_3O_4 > MnCo_2O_4$

In this sense, ZnCo₂O₄ has been used as an electrode material for the OER and has shown good results. For instance, Bao et al. 130 prepared ZnCo₂O₄ ultrathin nanosheets by thermal treatment of ZnCo-LDH (where LDH = layered double hydroxide). The electrode material was deposited on a GCE (glassy carbon electrode) and tested for OER performance in KOH 1.0 mol L⁻¹. The as-prepared ZnCo₂O₄ ultrathin nanosheet presented an overpotential of 340 mV at 10 mA cm⁻², and a Tafel slope of 38 mV dec⁻¹, compared to RuO₂ (33 mV dec⁻¹). The authors attributed these results to the large surface area of ZnCo₂O₄ ultrathin nanosheets that provides more exposed active sites on the surface, easing the catalytic reaction. Moreover, Xiang and colleagues²⁷⁰ synthesized ZnCo₂O₄ nanosheets with abundant oxygen vacancies (OV), named OV-ZnCo₂O₄, through the hydrothermal method and NaBH4 reduction process. The results showed that the presence of oxygen vacancies in ZnCo₂O₄ was beneficial for the OER. In fact, OV-ZnCo2O4 achieved an overpotential of 324 mV at 10 mA cm⁻², while pristine ZnCo₂O₄ showed an overpotential of 427 mV at the same current density. The catalytic kinetics for the OER also was evaluated and OV-ZnCo₂O₄ presented a Tafel slope of 56.9 mV dec⁻¹, which is lower than that of pristine ZnCo₂O₄ (74.4 mV dec⁻¹).

Although the studies aforementioned seem to be encouraging, the electrochemical performance of ZnCo₂O₄ is still restricted by its poor electronic conductivity, which leads to suppression of electrocatalytic activity towards the OER. Thus, most works reported in the literature presented ZnCo₂O₄ combined with other compounds, especially with conductive polymers and conductive carbon-based materials to enhance its electronic conductivity, resulting in a better catalytic activity for the OER, as can be seen in Table 8.

For instance, Tomboc et al. 274 prepared ZnCo2O4 nanoparticles with a nanocactus morphology in the presence of polyvinylpyrrolidone (PVP) (here denoted as PVP-ZnCo₂O₄) using a one-step hydrothermal method followed by calcination treatment. The authors demonstrated that in the presence of PVP the electrocatalytic activity of ZnCo₂O₄ was enhanced when compared to ZnCo2O4 without PVP. Indeed, PVP-ZnCo2O4 exhibited an overpotential of 282 mV at 10 mA cm⁻², while ZnCo₂O₄ without PVP showed an overpotential of 343 mV. PVP-ZnCo₂O₄ also presented an overpotential lower than PVP-NiCo₂O₄ (298 mV), synthesized under the same conditions.

Recently, Zhao and colleagues²⁷⁵ electropolymerized polypyrrole (PPy) on ZnCo₂O₄ nanowires under a constant potential of 0.9 V for 60, 100, 200 and 300 s, and the electrodes were denoted as ZnCo₂O₄@PPy-60, ZnCo₂O₄@PPy-100, ZnCo₂O₄@ PPy-200, and ZnCo₂O₄@PPy-300, respectively. The SEM image of ZnCo₂O₄@PPy-200 in Fig. 21B reveals that nanowires were coated by a thin layer of PPy, in comparison to ZnCo2O4 (Fig. 21A), and from the TEM images in Fig. 21C and D it is possible to observe that nanowires are composed of many nanoparticles. In addition, ZnCo₂O₄@PPy-200 presented a surface area of 56 m² g⁻¹ higher than pristine ZnCo₂O₄ (39 m² g⁻¹).

Table 8 ZnCo₂O₄-based OER and HER catalysts and their main electrocatalytic parameters

	Catalyst	Preparation method	Overpotential at 10 mA cm ⁻² ($E \eta_{10}$) (mV νs . RHE)	Tafel slope (mV dec ⁻¹)	Stability (h)	pH conditions (mol L ⁻¹)	Ref.
OER	ZnCo ₂ O ₄	Sol-gel method	650	51	_	KOH 0.1	271
	ZnCo ₂ O ₄ nanosheets	Thermal treatment of Zn-Co LDH	340	38	_	KOH 1.0	130
	MOF-derived ZnCo ₂ O ₄	Calcination process	389	61.8	2	KOH 1.0	272
	OV-ZnCo ₂ O ₄	Hydrothermal method	324	56.9	30	KOH 0.1	270
	m-ZnCo ₂ O ₄	Calcination process	300	54	_	KOH 1.0	273
	PVP-ZnCo ₂ O ₄ NPs	Hydrothermal method	282	79.9	24	KOH 1.0	274
	ZnCo ₂ O ₄ @PPy-200	Hydrothermal and electrochemical deposition	254	60.77	42	KOH 1.0	275
	ZnCo ₂ O ₄ -CNTs	Hydrothermal method	490	_	_	KOH 0.1	254
	ZnCo ₂ O ₄ @C-MWCNTs	Calcination process	327	65	25	KOH 1.0	276
	ZnCo ₂ O ₄ @NC/CT	Carbonization-oxidation process	196.4	61.3	45	KOH 1.0	138
	rGO-ZnCo ₂ O ₄	Solvothermal method	300	59.2	12	KOH 1.0	261
	Co/ZnCo ₂ O ₄ @NC-CNTs	Pyrolysis treatment	370	64	30	KOH 1.0	255
	$ZnCo_2O_4$ @Ni(OH) ₂ - 2.0	Hydrothermal method	280.2^{a}	64.62	17	KOH 1.0	277
	ZnCo ₂ O ₄ @ZnCo-LDHs	Hydrolysis	375	73	_	KOH 1.0	278
	ZnCo ₂ O ₄ @NiFe-LDH	Hydrothermal method	249	96.7	20	KOH 1.0	279
	ZnCo ₂ O ₄ /FeOOH HPs	Thermal treatment of ZnCo/ZIFs	299	69	15	KOH 1.0	280
	ZnCo ₂ O ₄ /Au/CNTs	Hydrothermal method	440	46.2	_	KOH 1.0	281
	ZnCo ₂ O ₄ /Co _x Se _v	Solvothermal method	324	79.3	50	KOH 1.0	253
	C/ZnCo ₂ O ₄ /ZnO	Annealing	279	72	24	KOH 1.0	282
HER	Co ₂ P/CoO/ZnCo ₂ O ₄	Hydrothermal followed by phosphorization process	112	62	24	KOH 1.0	283
	ZnCo ₂ O ₄ @PPy-50	Hydrothermal and electrochemical deposition	133	62.4	_	KOH 1.0	57
	ZnCo ₂ O ₄ @PPy-200	Hydrothermal and electrochemical deposition	183.52	60.77	22	KOH 1.0	275

HPs = hollow polyhedrons; ZIFs = zeolitic imidazolate frameworks. ^a At 50 mA cm⁻².

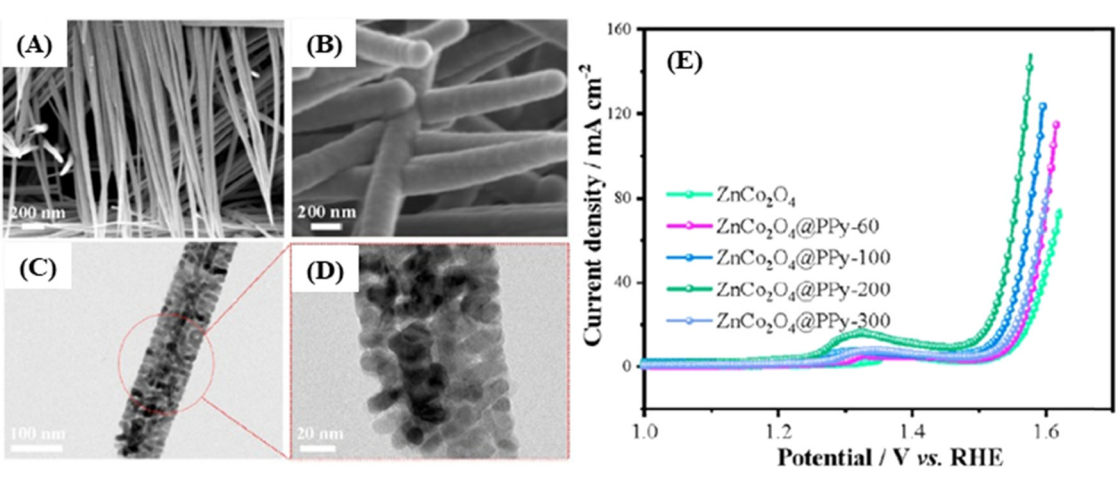


Fig. 21 SEM images of $ZnCo_2O_4$ (A) and $ZnCo_2O_4$ (PPy-200 (B). TEM images of $ZnCo_2O_4$ (PPy-200 (C and D). Linear sweep voltammetry at 2 mV s⁻¹ for ZnCo₂O₄ and ZnCo₂O₄@PPy samples (E). Reproduced with permission. ²⁷⁵ Copyright © 2021 Elsevier Ltd. All rights reserved.

Among these samples, ZnCo₂O₄@PPy-200 exhibited a lower overpotential (250 mV) at 10 mV cm⁻² (Fig. 21E) and a lower Tafel slope (60.77 mV dec⁻¹). Chronoamperometric studies were performed to evaluate the durability and stability of the ZnCo₂O₄@PPy-200 electrode, and even after 42 hours the catalyst remained steady, revealing its excellent stability.

In addition to conductive polymers, carbon-based materials (carbon nanotubes and graphene) have been widely used with cobaltite spinel oxides to improve their electronic conductivity, 284,285 thus providing a conducting platform. Furthermore, these materials, when combined, present a synergistic effect in the OER owing to their high surface area, providing more electrocatalytically active sites for charge transport between the electrode/electrolyte interface. For instance, Yan and coauthors²⁵⁵ reported the synthesis of Co/ZnCo₂O₄ from a MOF (CoZn-ZIF-L) sandwiched in N-doped carbon interconnected with carbon nanotubes (denoted Co/ZnCo2O4@NC-CNTs) as an electrode material for OER activity. The composite presented an overpotential of 370 mV at a current density of 10 mA cm⁻² and a low Tafel slope of 64 mV dec⁻¹. Similarly, Liu et al.²⁷⁶ embedded two different MOFs (metal-organic frameworks) ZIF-8 and ZIF-67 into MWCNTs (multi-walled carbon nanotubes) and obtained ZnCo2O4@C-MWCNTs by the calcination process. The electrode material exhibited a low overpotential of 327 mV at 10 mA cm⁻² and a Tafel slope of 65 mV dec⁻¹. In addition, the electrocatalytic activity of ZnCo2O4@C-MWCNTs remained unchanged, even after 25 hours of tests, demonstrating the reliability of the material.

In the same way, Kong et al., 138 using a ZnCo MOF, prepared an electrode material based on zinc-cobalt oxide nanoflakes@N-doped carbon hollow nanowall arrays anchored onto carbon textile (ZnCo₂O₄@NC/CT). The SEM images of ZnCo₂O₄@ NC/CT show that the compound grown vertically on a carbon textile electrode (Fig. 22A) and holes can be observed in its structure (Fig. 22B), caused by cation exchange between Co²⁺ and Zn²⁺. Furthermore, the hollow structure is confirmed through the contrast between the shell and core (hollow), as can be seen in Fig. 22C. The electrode exhibited an outstanding low overpotential of 196.4 mV at 10 mV cm⁻², a low Tafel slope of 61.3 mV dec⁻¹, and a long-term durability of 45 hours (Fig. 22D). The authors attributed the excellent results to (i) the decreased resistance at the interface between the substrate and the electrode material due to the direct growth of N-doped carbon nanowalls on the substrate surface, leading to improvement of the ion/electron transfer rates and (ii) the easy penetration of electrolyte, leading to faster faradaic reactions and ion diffusion rates, thanks to the high surface area of the porous structure of the ZnCo₂O₄ nanoflake shell, as shown in Fig. 22E and F.

Graphene has also been combined with spinel oxides to improve the electrocatalytic activity for the OER. 284,286,287 To enhance the catalytic activity of ZnCo₂O₄ towards the OER, Chakabarty et al. 261 prepared a ZnCo₂O₄ grafted onto reduced graphene oxide (rGO) sheet through the solvothermal method. The SEM and TEM images in Fig. 19A and B revealed that the structure of the ZnCo₂O₄ microsphere is highly porous, as well as composed of several nanoparticles with an average size of 10 nm. The highly porous structure of ZnCo₂O₄ was maintained in the rGO-ZnCo₂O₄, as shown in Fig. 19B. The rGO-ZnCo₂O₄ composite presented the lowest overpotential at 10 mA cm⁻² for the OER (300 mV) when compared to rGO (510 mV), ZnCo₂O₄ (410 mV), and benchmark IrO₂ (340 mV), or a rGO/ ZnCo-layered double hydroxide composite (onset overpotential ~330 mV). Moreover, rGO-ZnCo₂O₄ presented high stability and the current density remained stable from the beginning to the end of the measurement (12 h), differently from ZnCo₂O₄ that presented a decrease of current density, caused by gas bubble formation. In addition, the electrocatalytic activity of rGO-ZnCo2O4 towards the OER was evaluated by SECM measurement. It is possible to observe that a small current density is detected from 1.4 V, indicating the beginning of the OER process. As the potential increases to 1.45 V and 1.5 V the current density also increases.

In addition to carbon-based materials, other compounds such as LDH and oxides have been associated with ZnCo2O4, as

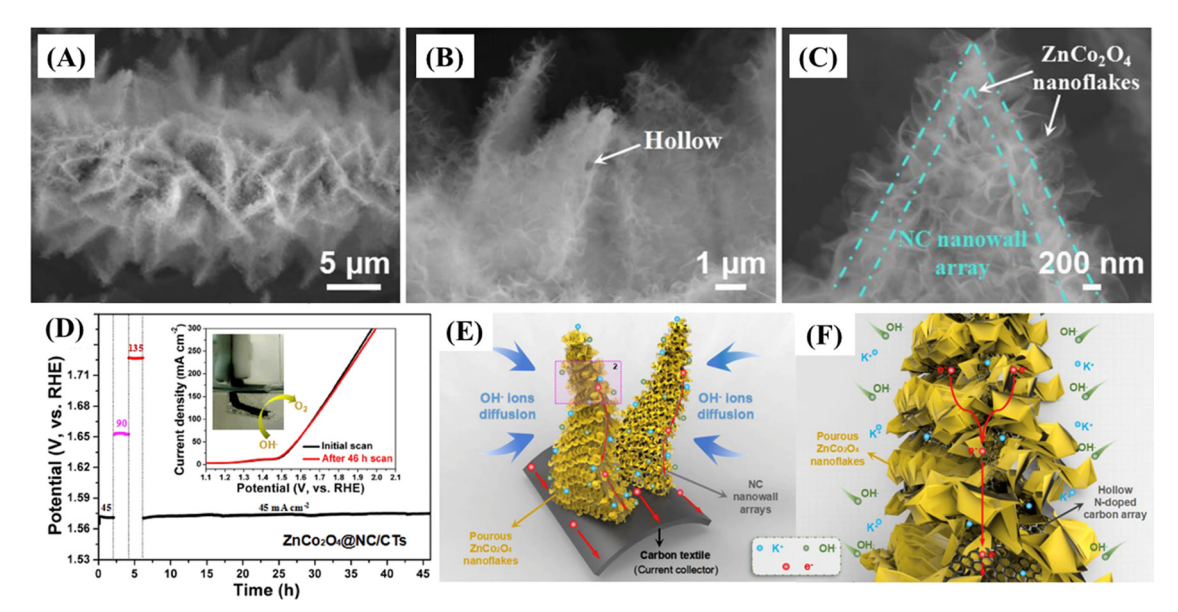


Fig. 22 (A-C) SEM images of $ZnCo_2O_4@NC/CT$. (D) Stability measurements of $ZnCo_2O_4@NC/CT$ at different current densities and (E and F) schematic illustration of the ZnCo₂O₄@NC/CT electrode. Reproduced with permission.¹³⁸ Copyright © 2019 Published by Elsevier B.V.

can be seen in Table 8. For instance, Pan et al. 278 reported the synthesis of ZnCo₂O₄(a)ZnCo-LDH yolk-shell nanospheres. The electrode material exhibited an overpotential of 375 mV at 10 mA cm⁻² and a Tafel slope of 73 mV dec⁻¹. Its electrochemical performance was attributed to the large surface area, the synergistic effect between ZnCo₂O₄ and ZnCo-LDH, and the interconnection among the nanosheets which consisted of the nanospheres, causing the reduction of the transportation path of electrolyte ions. Que et al. 279 obtained a core-shell structure of ZnCo2O4@NiFe-LHD that presented an overpotential of 249 mV at 10 mA cm⁻². The authors explained that the low overpotential achieved by the electrode material was due to the synergistic effect between core@shell structure components. Xiong et al. 282 prepared a C/ZnCo₂O₄/ZnO material, combining two strategies (preparation of MOF-derived ZnCo₂O₄ and the formation of a hierarchical core@shell structure). As a consequence, the electrode material required 279 mV overpotential to reach 10 mA cm⁻² current density. Besides, the electrocatalyst did not present significant degradation after a 24 h stability test.

Possible strategies and tendencies in the preparation of electrode materials based on ZnCo2O4 for OER catalysis can be seen in Fig. 23, where the electrocatalysts are summarized according to their low overpotential ($\eta_{10} \leq 300 \text{ mV}$). Analyzing the electrode materials displayed in Fig. 23 we figured out that three of the nine electrocatalysts based on ZnCo₂O₄ are MOF derivatives, and one of them presented the best electrochemical performance for OER catalysis among the electrocatalysts reported. In fact, ZnCo2O4@NC/CT, C/ZnCo2O4/ZnO and ZnCo₂O₄/FeOOH HPs exhibited an overpotential of 196.4, 279 and 299 mV, respectively. The best electrocatalyst ZnCo₂O₄@ NC/CT presented an overpotential of ~ 102 mV lower than the seventh electrocatalyst also based on MOF-derivative ZnCo₂O₄/ FeOOH HPs (299 mV). Although both of them were designed

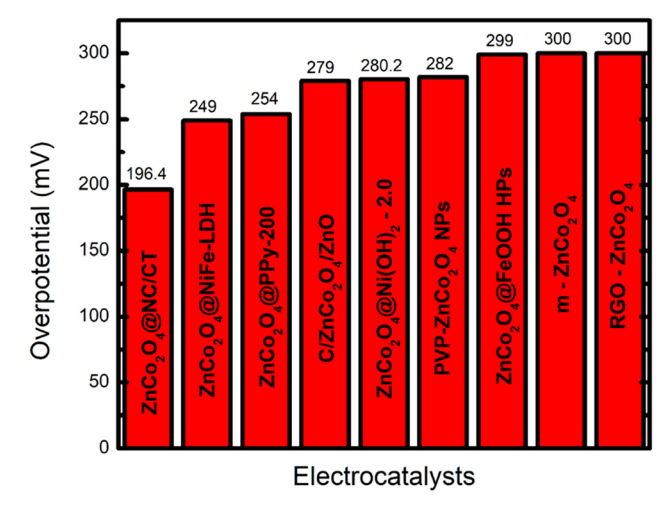


Fig. 23 The top 9 electrocatalysts based on ZnCo₂O₄ for the OER that presented an overpotential \leq 300 mV ($\eta_{10} \leq$ 300 mV).

from the MOF, the former was combined with a carbon material that enhanced the electronic conductivity of the electrode. However, the rGO-ZnCo₂O₄ electrocatalyst occupied the eighth position along with m-ZnCo₂O₄ and both of them presented an overpotential of 300 mV.

Among the electrode materials displayed in Fig. 23, it can be noticed that the combination of ZnCo2O4 with conductivity polymers can also be a good strategy to improve the electrochemical performance of the electrocatalyst. Indeed, intermediate overpotential values were reached for ZnCo₂O₄@PPy-200 (254 mV) and PVP-ZnCo₂O₄ NPs (282 mV) electrodes, occupying, respectively, the third and sixth positions.

The design of hierarchical structures as core@shell providing a shortened ion/electron transport pathways and a large surface area with a large number of electrocatalytic sites exposed, favoring

faradaic reactions, seems to be another interesting strategy to improve the electrochemical performance for OER catalysis. Thus, it can be highlighted that the electrocatalyst based on ZnCo₂O₄(a) NiFe-LDH presented the second-best electrochemical performance with an overpotential of 249 mV, and the synergistic effect between the core and shell materials in the structure contributed to the excellent result. It is noteworthy that the chosen shell material also was fundamental to achieving the results. In fact, recent studies have shown that NiFe-LDH and ternary NiFe-LDH derivatives are promising electrode materials for the OER catalysis.²⁸⁹ The fifth position was occupied by the electrocatalyst ZnCo₂O₄(aNi(OH)₂ – 2.0, presenting an overpotential of 280.2 mV, where the presence of Ni(OH)₂ as a shell material improved the electrochemical performance of the electrode materials, since the Ni(OH)₂ nanosheets made transporting electrons/ions easier. In fact, the overpotential value for the ZnCo₂O₄(a)Ni(OH)₂ is much smaller than those of many other pristine materials such as NiO (310 mV), ²⁹⁰ ZnO (340 mV)²⁹¹ and Ni(OH)₂ (340 mV). ²⁹²

Although many works using ZnCo₂O₄ as an electrode material for the catalysis of OER processes have been reported, few articles using the same material were found in the literature for HER electrocatalysis, as can be seen in Table 8. The main reason for this is that the production of high-purity hydrogen from the water-splitting method²⁹³ still is restricted by the sluggish kinetics of the OER.264

Among these works, we can highlight that reported by Zhang and colleagues²⁸³ where zinc cobalt oxide/phosphide (Co₂P/ CoO/ZnCo₂O₄) hollow submicron boxes were obtained and used as an electrode material for the HER. The electrocatalyst showed an overpotential of 112 mV at -10 mA cm⁻² current density; for comparison purposes the commercial Pt/C electrode also was tested and presented an overpotential of 19 mV at the same current density. Furthermore, the electrode materials exhibited a Tafel slope of 62 mV dec⁻¹, indicating that the reaction pathway obeys the Volmer-Heyrovsky mechanism with a fast Volmer step for the HER.

5. Conclusion and outlook

The morphology of ZnCo₂O₄ has a huge impact on its electrochemical performance, and can be improved by means of a rational design. The specific capacitance, electrocatalytic activity, rate-capability and cycling stability of ZnCo₂O₄-based electrodes heavily depend on ZnCo₂O₄ mechanical properties. Bulkier microand nanoparticles usually have low specific surface area (even lower if they are not porous or having at least rough surfaces), heavily suffering from the strain effects throughout the chargedischarge cycling, and high internal electrical resistance due to low surface area-to-volume ratios.

The design of 1D and 2D morphologies, along with hollow and/or porous structures, can partially overcome these limitations, specially aligned with suitable spaces between these 1D and 2D structures. 1D and 2D structures present increased specific surface areas, promoting electrolyte diffusion and electroactive site availability; greatly reduced one or more dimensions, providing shortened electron transfer pathways and alleviating the strain effects caused by volume changes; and in the case of electrocatalysts the high porosity and pore sizes, enhancing specific surface area and facilitating electrolyte adsorption and product release (e.g., O_2 in the OER and H_2 in the HER).

In fact, for supercapacitive applications, 1D structures can deliver high specific capacitances at lower current densities, owing to their unidimensional electron pathways and high specific surface area, which enhances the electroactive site availability. However, usually at higher current densities the electrolyte diffusion is hindered due to the entanglement of such 1D structures, which reduces the area for electrolyte penetration within the structure, limiting the electroactive site availability and cyclability. This effect can also be observed in 2D structures, which, even being the most commonly synthesized and being known for their high specific capacitance, can present strain effects caused by volume changes if the space between the structures is not suitable for fast electrolyte diffusion at higher current densities. Thus, it is extremely beneficial to engineering electrodes based on ZnCo₂O₄ with wide-open 1D or 2D nanostructures, which, along with all the benefits of such structures, facilitates the electrolyte diffusion even at higher current densities and further alleviates the strain effects of continuous charge-discharge cycling processes.

As for electrocatalytic applications, similarly to supercapacitive applications, it is interesting to synthesize wide-open and porous nanostructures. 1D nanostructures usually present unsuitable specific surface area, pore sizes and porosity for efficient electrolyte adsorption and product desorption, hindering the electrocatalyst performance of such structures, especially in comparison to 2D structured nanoparticles. 2D nanostructures commonly present the most optimal mesoporous and microporous sizes and volumes for the promotion of electrocatalytic activity, which can be even further enhanced according to the spaces between such structures by the facilitation of electrolyte penetration and enhancement of electroactive site availability.

Additionally, the electrochemical performance of ZnCo₂O₄based electrodes can be even more improved by the incorporation of composites and/or binder-free electrode production, along with the morphology control. The use of slurry-cast electrodes with binders that can significantly reduce the electronic conductivity, limiting the availability of active materials, and hindering the ion-diffusion. It can also increase the mass density as "dead-mass" and reduce the material integrity through cycling. So, binder-free electrodes should be preferred to circumvent all the above-mentioned downsides. ZnCo2O4 composites can be produced with highly electrically conductive and/or electrochemically active carbonaceous and other transition metal materials, such as oxides, hydroxides and sulfides, as both support and coating components. They can provide bigger specific surface area, faster electron transfer, and short and more efficient ion-diffusion paths. In addition to the more active sites and richer redox reactions, the overall stability is greatly improved. One can also morphologically orient the growth of ZnCo₂O₄ when it is used as a support material.

The strategies for synthesis and application of pristine ZnCo₂O₄ and its composites in LIBs, SIBs, Li-S batteries and metal-air batteries are summed up. Although ZnCo2O4 has been applied in energy storage and has proved to be a promising electrode material, there are a few challenges to mention, e.g., its poor electrical conductivity, slow lithium diffusion and short cycling life. This is associated with the volume expansion during the lithium insertion and extraction process. Many prospective strategies should be developed for the application of ZnCo₂O₄ electrode materials, and we hope that this review article will facilitate further studies and advancements in this area.

Improving the conductivity is always a key issue in the development of electrode materials based on ZnCo₂O₄. Generally synthesis of electrode materials with nanoscale dimension ZnCo₂O₄ has already been proven to be effective for obtaining high-power density, high-energy density, better stability and other admirable electrochemical performances. Nanostructured ZnCo2O4 composites with conductive materials such as polymers and carbon were also demonstrated to improve their electrochemical performance. These strategies can effectively enhance the conductivity and alleviate the volume change of ZnCo₂O₄ electrode materials. Therefore, ZnCo₂O₄ has been gaining more and more attention in the field of energy storage in recent years.

For application as electrocatalysts in energy technologies, ZnCo₂O₄ and its composites show great potential due to their high intrinsic activity. In many cases they can exhibit bifunctionalities, encompassing both ORR and OER activity. In fact, it is important to highlight that the main strategies employed in electrode materials for the ORR consisted of the design of new catalysts with different morphologies, and the formation of composites with conducting nanocarbons, such as carbon nanotubes and graphene.

Similarly, although ZnCo₂O₄ exhibits an overpotential close to 300 mV as an electrode material for OER catalysis, it is limited by its poor conductivity. For this reason, ZnCo₂O₄-based OER electrocatalysts have been combined with conducting carbon materials and polymers, as well as with compounds such as metal oxides/hydroxides. Curiously, among the top 9 $(\eta_{10} \leq 300 \text{ mV})$ electrode materials for OER catalysis, three electrocatalysts are based on MOF-derivatives. Deriving ZnCo₂O₄ electrodes using the MOF strategies can be interesting, since the main features will be preserved, such as a high porous structure and large surface area.²⁹⁴ They will improve the electrochemical performance of the electrocatalyst. The design of the electrode material is fundamental for obtaining a good electrochemical performance. For instance, hierarchical core@shell structures can yield excellent results because of their large surface area, while the exposed electrocatalytic sites can improve the faradaic reaction, and shorten the ion/electron transport pathway. In fact, the regulation strategies for improving the electrocatalytic performance of ZnCo₂O₄-based electrodes follow trends also reported in other $works^{6,289,295}$ and can be summarized mainly as: (a) reducing electrical resistance using conductive supports and (b) increasing active sites by

nanostructuration, morphology engineering and porous structure construction.²⁷

Despite the important advances in the design of new materials based on ZnCo₂O₄ aforementioned, many challenges still need to be overcome regarding a full exploration and implementation in practical/real application in electrochemical energy storage and conversion. For instance, currently it is mandatory the development of devices that are able to withstand high current density with long-term cycling stability, aiming to reduce the charge time, e.g., devices that can provide high energy density at a high-power density during the long-term charge/discharge cycling process. However, the excellent performances generally reported in the literature, especially in studies using three-electrode systems, and even in two-electrode devices, may not fully represent a real application, since on a laboratory scale it usually takes 2-3 mg cm⁻² of the electrode material, but commercially always demands high mass loading (>10 mg cm⁻²). In this sense, the design and manufacture of more robust devices with greater thickness and mass loading should be further studied.

In fact, we are convinced that much research needs to be done to further improve electrochemical and electrocatalytic materials based on ZnCo2O4, where site engineering and a conductivity optimization approach should be used in the quest for ideal electrode materials.27 For instance, the incorporation (or metal-ion doping) of third and fourth metal ions³ or the development of high entropy materials²⁹⁶ can be decisive for improving energy storage and for electrocatalytic activity. 289 In fact, these strategies can also help in the challenge of minimizing the use of Co, which are pushing a new trend of emerging low-Co (and Co-free) materials as next-generation electrode materials for energy applications.²⁹⁷ In addition, the research should seek to increase the conductivity and porosity of ZnCo₂O₄/carbon composites as strategies for manufacturing electrodes with high mass loading for real application. From this perspective, the preparation of ZnCo2O4/carbon derived from MOFs should be studied more deeply, especially those derived from the zeolitic imidazolate framework (ZIF-67, ZIF-8, ZIF-67 + ZIF-8, etc.). In fact, MOF-derived composites have been regarded as excellent new functional electrode materials for many applications, exhibiting exceptional conductivity, stability, porous/hollow structures with tunable shapes, and tailored compositions and electrochemical activity, overcoming the relatively low conductivity and missing chemical and/or structural robustness of precursor MOFs. 13,294,298 Therefore, these are some future directions for the development of ZnCo2O4 based materials for their commercial/real applications towards a more sustainable society.

Conflicts of interest

There are no conflicts to declare.

Acknowledgements

This work was supported by the São Paulo Research Foundation (FAPESP 2018/21489-1, 2017/13137-5, 2014/50867-3 and

2013/24725-4) and the National Council for Scientific and Technological Development (CNPq 401581/2016-0, 408222/ 2016-6, 442599/2019-6, 311847/2018-8), in addition to the fellowships granted to J. M. G. (FAPESP 2018/16896-7), M. I. S. (CAPES 141853/2015-8) and M. N. T. S. (CAPES 88882.429165/ 2019.01). The Grupo de Materiais Inorgânicos do Triângulo (GMIT) research group was supported by FAPEMIG (APQ-00330-14), Brazilian Institute of Science and Technology (INCT) in Carbon Nanomaterials.

References

- 1 S. Liu, L. Hu, X. Xu, A. A. Al-Ghamdi and X. Fang, Nickel Cobaltite Nanostructures for Photoelectric and Catalytic Applications, Small, 2015, 11, 4267-4283.
- 2 J. M. Gonçalves, A. Kumar, M. I. da Silva, H. E. Toma, P. R. Martins, K. Araki, M. Bertotti and L. Angnes, Nanoporous Gold-Based Materials for Electrochemical Energy Storage and Conversion, Energy Technol., 2021, 9, 2000927.
- 3 J. M. Gonçalves, M. I. da Silva, H. E. Toma, L. Angnes, P. R. Martins and K. Araki, Trimetallic oxides/hydroxides as hybrid supercapacitor electrode materials: a review, J. Mater. Chem. A, 2020, 8, 10534-10570.
- 4 S. J. Uke, V. P. Akhare, D. R. Bambole, A. B. Bodade and G. N. Chaudhari, Recent Advancements in the Cobalt Oxides, Manganese Oxides, and Their Composite As an Electrode Material for Supercapacitor: A Review, Front. Mater., 2017, 4, 21.
- 5 J. G. Ruiz-Montoya, V. L. Quispe-Garrido, J. C. Calderón Gómez, A. M. Baena Moncada and J. M. Gonçalves, Recent Progress and Prospects on Supercapacitor Materials based on Metal Oxide or Hydroxide/Biomass-Derived Carbon Composites, Sustainable Energy Fuels, 2021, 5, 5332–5365.
- 6 J. M. Gonçalves, D. P. Rocha, M. N. T. Silva, P. Roberto Martins, E. Nossol, L. Angnes, C. S. Rout and R. A. Abarza Munoz, Feasible strategies to promote the sensing performances of spinel MCo₂O₄ (M = Ni, Fe, Mn, Cu and Zn) based electrochemical sensors: A review, J. Mater. Chem. C, 2021, 9, 7852-7887.
- 7 Y. Li, X. Han, T. Yi, Y. He and X. Li, Review and prospect of NiCo₂O₄-based composite materials for supercapacitor electrodes, J. Energy Chem., 2019, 31, 54-78.
- 8 J. M. Gonçalves, M. N. T. Silva, K. K. Naik, P. R. Martins, D. P. Rocha, E. Nossol, R. A. A. Munoz, L. Angnes and C. S. Rout, Multifunctional spinel MnCo₂O₄ based materials for energy storage and conversion: a review on emerging trends, recent developments and future perspectives, J. Mater. Chem. A, 2021, 9, 3095-3124.
- 9 X. Zhao, L. Mao, Q. Cheng, J. Li, F. Liao, G. Yang, L. Xie, C. Zhao and L. Chen, Two-dimensional Spinel Structured Co-based Materials for High Performance Supercapacitors: A Critical Review, Chem. Eng. J., 2020, 387, 124081.
- 10 J. P. Cheng, W. D. Wang, X. C. Wang and F. Liu, Recent research of core-shell structured composites with NiCo2O4 as scaffolds for electrochemical capacitors, Chem. Eng. J., 2020, 393, 124747.

- 11 X. Han, X. Gui, T.-F. Yi, Y. Li and C. Yue, Recent progress of NiCo2O4-based anodes for high-performance lithiumion batteries, Curr. Opin. Solid State Mater. Sci., 2018, 22, 109-126.
- 12 R. Kumar, NiCo₂O₄ Nano-/Microstructures as High-Performance Biosensors: A Review, Nano-Micro Lett., 2020, 12, 122.
- 13 R. Wu, J. Sun, C. Xu and H. Chen, MgCo₂O₄-based electrode materials for electrochemical energy storage and conversion: a comprehensive review, Sustainable Energy Fuels, 2021, 5, 4807-4829.
- 14 J. Sun, C. Xu and H. Chen, A review on the synthesis of CuCo₂O₄-based electrode materials and their applications in supercapacitors, J. Materiomics, 2021, 7, 98-126.
- 15 H. Gao, S. Liu, Y. Li, E. Conte and Y. Cao, A Critical Review of Spinel Structured Iron Cobalt Oxides Based Materials for Electrochemical Energy Storage and Conversion, Energies, 2017, 10(11), 1787, DOI: 10.3390/en10111787.
- 16 M. Harada, F. Kotegawa and M. Kuwa, Structural Changes of Spinel MCo₂O₄ (M = Mn, Fe, Co, Ni, and Zn) Electrocatalysts during the Oxygen Evolution Reaction Investigated by In Situ X-ray Absorption Spectroscopy, ACS Appl. Energy Mater., 2022, 5, 278-294.
- 17 S. Gedi, R. Manne, G. Manjula, L. V. Reddy, C. P. Reddy, N. Marraiki, W. K. Kim, K. Mallikarjuna and M. S. Pratap, Reddy, Tunability of the self-assemblies of porous polygonlike zinc cobaltite architectures using mixed solvents for high-performance supercapacitors, I. Phys. Chem. Solids, 2022, 163, 110587.
- 18 J. A. Rajesh and K.-S. Ahn, Facile Hydrothermal Synthesis and Supercapacitor Performance of Mesoporous Necklace-Type ZnCo₂O₄ Nanowires, Catalysts, 2021, 11(12), 1516, DOI: 10.3390/catal11121516.
- 19 S.-H. Lee, J. H. Kim and J.-R. Yoon, Laser Scribed Graphene Cathode for Next Generation of High Performance Hybrid Supercapacitors, Sci. Rep., 2018, 8, 8179.
- 20 N.-T. Suen, S.-F. Hung, Q. Quan, N. Zhang, Y.-J. Xu and H. M. Chen, Electrocatalysis for the oxygen evolution reaction: recent development and future perspectives, Chem. Soc. Rev., 2017, 46, 337-365.
- 21 M. Bohra, V. Alman and R. Arras, Nanostructured ZnFe₂O₄: An Exotic Energy Material, Nanomaterials, 2021, 11(5), 1286, DOI: 10.3390/nano11051286.
- 22 L. Sun, Q. Luo, Z. Dai and F. Ma, Material libraries for electrocatalytic overall water splitting, Coord. Chem. Rev., 2021, 444, 214049.
- 23 J. M. Gonçalves, P. R. Martins, K. Araki and L. Angnes, Recent progress in water splitting and hybrid supercapacitors based on nickel-vanadium layered double hydroxides, J. Energy Chem., 2021, 57, 496-515.
- 24 Y. Wang, X. Huang and Z. Wei, Recent developments in the use of single-atom catalysts for water splitting, Chin. J. Catal., 2021, 42, 1269-1286.
- 25 P. Chen, J. Ye, H. Wang, L. Ouyang and M. Zhu, Recent progress of transition metal carbides/nitrides for electrocatalytic water splitting, J. Alloys Compd., 2021, 883, 160833.

- 26 Y. Yan, T. He, B. Zhao, K. Qi, H. Liu and B. Y. Xia, Metal/ covalent-organic frameworks-based electrocatalysts for water splitting, J. Mater. Chem. A, 2018, 6, 15905-15926.
- 27 J. M. Gonçalves, T. A. Matias, K. C. F. Toledo and K. Araki, in Advances in Inorganic Chemistry, ed. R. V. Eldik and C. Hubbard, Elsevier, 2019, vol. 74, p. 63.
- 28 M. Tahir, L. Pan, F. Idrees, X. Zhang, L. Wang, J.-J. Zou and Z. L. Wang, Electrocatalytic oxygen evolution reaction for energy conversion and storage: A comprehensive review, Nano Energy, 2017, 37, 136-157.
- 29 A. Chakraborty, S. Kunnikuruvan, S. Kumar, B. Markovsky, D. Aurbach, M. Dixit and D. T. Major, Layered Cathode Materials for Lithium-Ion Batteries: Review of Computational Studies on $\text{LiNi}_{1-x-y}\text{Co}_x\text{Mn}_y\text{O}_2$ and $\text{LiNi}_{1-x-y}\text{Co}_x\text{Al}_y\text{O}_2$, Chem. Mater., 2020, 32, 915-952.
- 30 M. Winter and R. J. Brodd, What Are Batteries, Fuel Cells, and Supercapacitors?, Chem. Rev., 2004, 104, 4245-4270.
- 31 C. Zou, L. Zhang, X. Hu, Z. Wang, T. Wik and M. Pecht, A review of fractional-order techniques applied to lithiumion batteries, lead-acid batteries, and supercapacitors, J. Power Sources, 2018, 390, 286-296.
- 32 Y. Gogotsi and R. M. Penner, Energy Storage in Nanomaterials - Capacitive, Pseudocapacitive, or Battery-like?, ACS Nano, 2018, 12, 2081-2083.
- 33 J. Cherusseri, D. Pandey and J. Thomas, Symmetric, Asymmetric, and Battery-Type Supercapacitors Using Two-Dimensional Nanomaterials and Composites, Batteries Supercaps, 2020, 3, 860-875.
- 34 N. R. Chodankar, H. D. Pham, A. K. Nanjundan, J. F. S. Fernando, K. Jayaramulu, D. Golberg, Y.-K. Han and D. P. Dubal, True Meaning of Pseudocapacitors and Their Performance Metrics: Asymmetric versus Hybrid Supercapacitors, Small, 2020, 16, 2002806.
- 35 J. M. Gonçalves, M. I. da Silva, M. Hasheminejad, H. E. Toma, K. Araki, P. R. Martins and L. Angnes, Recent Progress in Core@Shell Sulfide Electrode Materials for Advanced Supercapacitor Devices, Batteries Supercaps, 2021, 4, 1397.
- 36 R. Wang, M. Yao and Z. Niu, Smart supercapacitors from materials to devices, InfoMat, 2020, 2, 113-125.
- 37 M. D. Stoller, S. A. Stoller, N. Quarles, J. W. Suk, S. Murali, Y. Zhu, X. Zhu and R. S. Ruoff, Using coin cells for ultracapacitor electrode material testing, J. Appl. Electrochem., 2011, 41, 681.
- 38 M. Yu and X. Feng, Thin-Film Electrode-Based Supercapacitors, Joule, 2019, 3, 338-360.
- 39 D. Chen, K. Jiang, T. Huang and G. Shen, Recent Advances in Fiber Supercapacitors: Materials, Device Configurations, and Applications, Adv. Mater., 2020, 32, 1901806.
- 40 F. Bu, W. Zhou, Y. Xu, Y. Du, C. Guan and W. Huang, Recent developments of advanced micro-supercapacitors: design, fabrication and applications, npj Flexible Electron., 2020, 4, 31.
- 41 V. Augustyn, P. Simon and B. Dunn, Pseudocapacitive oxide materials for high-rate electrochemical energy storage, Energy Environ. Sci., 2014, 7, 1597-1614.

42 D. P. Chatterjee and A. K. Nandi, A review on the recent advances in hybrid supercapacitors, J. Mater. Chem. A, 2021, 9, 15880-15918.

- 43 D. P. Dubal, O. Ayyad, V. Ruiz and P. Gómez-Romero, Hybrid energy storage: the merging of battery and supercapacitor chemistries, Chem. Soc. Rev., 2015, 44, 1777-1790.
- 44 D. Qian, C. Ma, K. L. More, Y. S. Meng and M. Chi, Advanced analytical electron microscopy for lithium-ion batteries, NPG Asia Mater., 2015, 7, e193.
- 45 H. Cheng, J. G. Shapter, Y. Li and G. Gao, Recent progress of advanced anode materials of lithium-ion batteries, J. Energy Chem., 2021, 57, 451-468.
- 46 Y. Han, Y. Lei, J. Ni, Y. Zhang, Z. Geng, P. Ming, C. Zhang, X. Tian, J.-L. Shi, Y.-G. Guo and Q. Xiao, Single-Crystalline Cathodes for Advanced Li-Ion Batteries: Progress and Challenges, Small, 2022, 2107048.
- 47 Y. Lu, Q. Zhang and J. Chen, Recent progress on lithiumion batteries with high electrochemical performance, Sci. China: Chem., 2019, 62, 533-548.
- 48 J. M. Tarascon and M. Armand, Issues and challenges facing rechargeable lithium batteries, Nature, 2001, 414, 359-367.
- 49 S.-W. Kim, D.-H. Seo, X. Ma, G. Ceder and K. Kang, Electrode Materials for Rechargeable Sodium-Ion Batteries: Potential Alternatives to Current Lithium-Ion Batteries, Adv. Energy Mater., 2012, 2, 710-721.
- 50 Y. Li and J. Lu, Metal-Air Batteries: Will They Be the Future Electrochemical Energy Storage Device of Choice?, ACS Energy Lett., 2017, 2, 1370-1377.
- 51 H.-F. Wang and Q. Xu, Materials Design for Rechargeable Metal-Air Batteries, Matter, 2019, 1, 565-595.
- 52 K. Yoo, S. Banerjee, J. Kim and P. Dutta, A Review of Lithium-Air Battery Modeling Studies, Energies, 2017, 10, 1748.
- 53 Y. Huang, Y. Wang, C. Tang, J. Wang, Q. Zhang, Y. Wang and J. Zhang, Atomic Modulation and Structure Design of Carbons for Bifunctional Electrocatalysis in Metal-Air Batteries, Adv. Mater., 2019, 31, 1803800.
- 54 Z. Ma, X. Yuan, L. Li, Z.-F. Ma, D. P. Wilkinson, L. Zhang and J. Zhang, A review of cathode materials and structures for rechargeable lithium-air batteries, Energy Environ. Sci., 2015, 8, 2144-2198.
- 55 K. Song, B. Yang, Z. Li, Y. Lv, Y. Yu, L. Yuan, X. Shen and X. Hu, Direct synthesis of ACo_2O_4 (A = Ni, Cu, Fe, Zn) nanowires on carbon cloth as an oxygen electrode catalyst for rechargeable lithium-oxygen batteries, Appl. Surf. Sci., 2020, 529, 147064.
- 56 T. Ramachandran and F. Hamed, Electrochemical performance of plate-like zinc cobaltite electrode material for supercapacitor applications, J. Phys. Chem. Solids, 2018, **121**, 93-101.
- 57 X. Liu, Q. Li, Y. Qin and Y. Jiang, Constructing high-performance electrode materials using core-shell ZnCo₂O₄@PPy nanowires for hybrid batteries and water splitting, RSC Adv., 2020, 10, 28324-28331.
- 58 D. Yu, Z. Zhang, Y. n Meng, Y. Teng, Y. Wu, X. Zhang, Q. Sun, W. Tong, X. Zhao and X. Liu, The synthesis of hierarchical ZnCo₂O₄@MnO₂ core-shell nanosheet arrays

- on Ni foam for high-performance all-solid-state asymmetric supercapacitors, Inorg. Chem. Front., 2018, 5, 597-604.
- 59 L. Merabet, K. Rida and N. Boukmouche, Sol-gel synthesis, characterization, and supercapacitor applications of MCo₂O₄ (M = Ni, Mn, Cu, Zn) cobaltite spinels, Ceram. Int., 2018, 44, 11265-11273.
- 60 K. Prasad, G. Rajasekhara Reddy, M. Rajesh, P. R. Babu, G. Shanmugam, N. J. Sushma, M. S. Pratap Reddy and B. Deva, Electrochemical Performance of 2D-Hierarchical Sheet-Like ZnCo₂O₄ Microstructures for Supercapacitor Applications, Crystals, 2020, 10, 566, DOI: 10.3390/cryst10070566.
- 61 D. M. Alqahtani, C. Zequine, C. K. Ranaweera, K. Siam, P. K. Kahol, T. P. Poudel, S. R. Mishra and R. K. Gupta, Effect of metal ion substitution on electrochemical properties of cobalt oxide, J. Alloys Compd., 2019, 771, 951-959.
- 62 Y. Shang, T. Xie, C. Ma, L. Su, Y. Gai, J. Liu and L. Gong, Synthesis of hollow ZnCo₂O₄ microspheres with enhanced electrochemical performance for asymmetric supercapacitor, Electrochim. Acta, 2018, 286, 103-113.
- 63 B. Saravanakumar, G. Ravi, R. Yuvakkumar, V. Ganesh, S. Ravichandran, M. Thambidurai and A. Sakunthala, Hydrothermal synthesis and electrochemical properties of ZnCo₂O₄ microspheres, *Ionics*, 2019, 25, 353-360.
- 64 H. Chen, J. Wang, X. Han, F. Liao, Y. Zhang, X. Han and C. Xu, Simple growth of mesoporous zinc cobaltite urchinlike microstructures towards high-performance electrochemical capacitors, Ceram. Int., 2019, 45, 4059-4066.
- 65 H. Chen, J. Wang, X. Han, F. Liao, Y. Zhang, L. Gao and C. Xu, Facile synthesis of mesoporous ZnCo₂O₄ hierarchical microspheres and their excellent supercapacitor performance, Ceram. Int., 2019, 45, 8577-8584.
- 66 R. R. Gutturu, T. V. M. Sreekanth, R. Rajavaram, D. P. R. Borelli, G. R. Dillip, P. C. Nagajyothi and J. Shim, Effect of reaction time and PVP contents on morphologies of hierarchical 3D flower-like ZnCo₂O₄ microstructures for energy storage devices, Int. J. Energy Res., 2020, 44, 11233-11247.
- 67 J. Bhagwan, Sk. Khaja Hussain and J. S. Yu, Aqueous asymmetric supercapacitors based on ZnCo2O4 nanoparticles via facile combustion method, J. Alloys Compd., 2020, 815, 152456.
- 68 Y. Shang, T. Xie, Y. Gai, L. Su, L. Gong, H. Lv and F. Dong, Self-assembled hierarchical peony-like ZnCo₂O₄ for highperformance asymmetric supercapacitors, Electrochim. Acta, 2017, 253, 281-290.
- 69 M. Priya, V. K. Premkumar, P. Vasantharani and G. Sivakumar, Structural and electrochemical properties of ZnCo₂O₄ nanoparticles synthesized by hydrothermal method, Vacuum, 2019, 167, 307-312.
- 70 D. Song, J. Zhu, J. Li, T. Pu, B. Huang, C. Zhao, L. Xie and L. Chen, Free-standing Two-dimensional Mesoporous ZnCo₂O₄ Thin Sheets Consisting of 3D Ultrathin Nanoflake Array Frameworks for High Performance Asymmetric Supercapacitor, Electrochim. Acta, 2017, 257, 455-464.
- 71 A. J. C. Mary and A. C. Bose, Surfactant assisted ZnCo₂O₄ nanomaterial for supercapacitor application, Appl. Surf. Sci., 2018, 449, 105-112.

- 72 J. Zhu, D. Song, T. Pu, J. Li, B. Huang, W. Wang, C. Zhao, L. Xie and L. Chen, Two-dimensional porous ZnCo₂O₄ thin sheets assembled by 3D nanoflake array with enhanced performance for aqueous asymmetric supercapacitor, Chem. Eng. J., 2018, 336, 679-689.
- 73 X. Xiao, G. Wang, M. Zhang, Z. Wang, R. Zhao and Y. Wang, Electrochemical performance of mesoporous ZnCo₂O₄ nanosheets as an electrode material for supercapacitor, Ionics, 2018, 24, 2435-2443.
- 74 P. Sivakumar, P. Nakhanivej, C. J. Raj and H. S. Park, 3D flower-like oxygen-deficient non-stoichiometry zinc cobaltite for high performance hybrid supercapacitors, Int. J. Energy Res., 2021, 45, 10832-10842.
- 75 A. J. C. Mary, S. Thilagavathi and A. C. Bose, Influence of different synthesis approach on ZnCo₂O₄ nanomaterial and its supercapacitor behavior, AIP Conf. Proc., 2018, 1942, 140042,
- 76 D. He, Y. Gao, Y. Yao, L. Wu, J. Zhang, Z.-H. Huang and M.-X. Wang, Asymmetric Supercapacitors Based on Hierarchically Nanoporous Carbon and ZnCo2O4 From a Single Biometallic Metal-Organic Frameworks (Zn/Co-MOF), Front. Chem., 2020, 8, 719.
- 77 S. Zhao, X. Yu, H. Chen, K. Tao, Y. Hu and L. Han, Zeolitic imidazolate framework derived ZnCo2O4 hollow tubular nanofibers for long-life supercapacitors, RSC Adv., 2020, 10, 13922-13928.
- 78 X. Wu, L. Meng, Q. Wang, W. Zhang and Y. Wang, Highly flexible and large areal/volumetric capacitances for asymmetric supercapacitor based on ZnCo2O4 nanorods arrays and polypyrrole on carbon cloth as binder-free electrodes, Mater Lett., 2019, 234, 1-4.
- 79 G. P. Kamble, A. A. Kashale, S. S. Kolekar, I. W. P. Chen, B. R. Sathe and A. V. Ghule, Reflux temperature-dependent zinc cobaltite nanostructures for asymmetric supercapacitors, J. Mater. Sci.: Mater. Electron., 2021, 32, 5859-5869.
- 80 M. S. Javed, A. J. Khan, S. Asim, S. S. A. Shah, T. Najam, S. H. Siyalg, M. F. Tahir, Z. Zhao and W. Mai, Insights to pseudocapacitive charge storage of binary metal-oxide nanobelts decorated activated carbon cloth for highly-flexible hybrid-supercapacitors, J. Energy Storage, 2020, 31, 101602.
- 81 Z. Zhang, X. Zhang, Y. Feng, X. Wang, Q. Sun, D. Yu, W. Tong, X. Zhao and X. Liu, Fabrication of porous ZnCo₂O₄ nanoribbon arrays on nickel foam for highperformance supercapacitors and lithium-ion batteries, Electrochim. Acta, 2018, 260, 823-829.
- 82 G. Rajeshkhanna and G. Ranga, Rao, High energy density symmetric capacitor using zinc cobaltate flowers grown in situ on Ni foam, *Electrochim. Acta*, 2018, **261**, 265–274.
- 83 G. J. H. Lim, X. Liu, C. Guan and J. Wang, Co/Zn bimetallic oxides derived from metal organic frameworks for high performance electrochemical energy storage, Electrochim. Acta, 2018, 291, 177-187.
- 84 B. Saravanakumar, T. H. Ko and B.-S. Kim, Rational design of binder-free ZnCo₂O₄ and Fe₂O₃ decorated porous 3D Ni as high-performance electrodes for asymmetric supercapacitor, Ceram. Int., 2018, 44, 10635-10645.

- 85 Y. zhou, L. Chen, Y. Jiao, Z. Li and Y. Gao, Controllable fabrication of ZnCo₂O₄ ultra-thin curved sheets on Ni foam for high-performance asymmetric supercapacitors, Electrochim. Acta, 2019, 299, 388-394.
- 86 X. Li, M. Zhang, L. Wu, Q. Fu and H. Gao, Annealing temperature dependent ZnCo₂O₄ nanosheet arrays supported on Ni foam for high-performance asymmetric supercapacitor, J. Alloys Compd., 2019, 773, 367-375.
- 87 M. S. Javed, N. Shaheen, S. Hussain, J. Li, S. S. A. Shah, Y. Abbas, M. A. Ahmad, R. Raza and W. Mai, An ultra-high energy density flexible asymmetric supercapacitor based on hierarchical fabric decorated with 2D bimetallic oxide nanosheets and MOF-derived porous carbon polyhedra, J. Mater. Chem. A, 2019, 7, 946-957.
- 88 W. Wang, L. Chen, J. Qi, Y. Sui, Y. He, Q. Meng, F. Wei and Z. Sun, All-solid-state asymmetric supercapacitor based on N-doped activated carbon derived from polyvinylidene fluoride and ZnCo₂O₄ nanosheet arrays, J. Mater. Sci.: Mater. Electron., 2018, 29, 2120-2130.
- 89 M. Saghafi, S. A. Hosseini, S. Zangeneh, A. H. Moghanian and S. Mohajerzadeh, Ternary nanostructured MZnCo oxides (M = Al, Mg, Cu, Fe, Ni) prepared by hydrothermal method as excellent charge storage devices, Ionics, 2020, 26, 1491-1505.
- 90 Y. A. Kumar, K. D. Kumar and H.-J. Kim, Reagents assisted ZnCo₂O₄ nanomaterial for supercapacitor application, Electrochim. Acta, 2020, 330, 135261.
- 91 C. Du, E. Han, L. Sun, S. Qiao and L. Li, Template agent for assisting in the synthesis of ZnCo₂O₄ on Ni foam for highperformance supercapacitors, Ionics, 2020, 26, 383-391.
- 92 L. Cheng, M. Xu, Q. Zhang, G. Li, J. Chen and Y. Lou, NH₄F assisted and morphology-controlled fabrication of ZnCo₂O₄ nanostructures on Ni-foam for enhanced energy storage devices, J. Alloys Compd., 2019, 781, 245-254.
- 93 M. Saghafi and S. Zangeneh, Zn-Co oxide electrodes with excellent capacitive behavior for using supercapacitor application, Curr. Appl. Phys., 2019, 19, 745-755.
- 94 G. P. Kamble, A. A. Kashale, S. S. Dhanayat, S. S. Kolekar and A. V. Ghule, Binder-free synthesis of high-quality nanocrystalline ZnCo2O4 thin film electrodes for supercapacitor application, Bull. Mater. Sci., 2019, 42, 272.
- 95 D. Xie, R.-j Zhong, D. Ren, L.-y Tuo, G.-h Song and F. Hu, Self-assembled ZnCo₂O₄ micro-urchins as highperformance electrode materials for energy storage device, J. Mater. Sci.: Mater. Electron., 2019, 30, 6439-6447.
- 96 S. Wang, Y. Teng, X. Liu, D. Yu, Y. n Meng, Y. Wu, S. Sun, X. Zhao and X. Liu, Facile synthesis of mesoporous ZnCo₂O₄ nanowire arrays and nanosheet arrays directly grown on nickel foam for high-performance supercapacitors, Inorg. Chem. Commun., 2019, 101, 16-22.
- 97 H. Yu, H. Zhao, Y. Wu, B. Chen and J. Sun, Electrospun ZnCo₂O₄/C composite nanofibers with superior electrochemical performance for supercapacitor, J. Phys. Chem. Solids, 2020, 140, 109385.
- 98 H. Li, L. Wang, Y. Guan, Y. Su, J. Mu, H. Che, A. Liu and Z. Guo, Facile solvothermal synthesis of ZnCo₂O₄/MnO₂

- nanosheets composite with enhanced electrochemical properties as supercapacitor electrodes, Appl. Phys. A: Mater. Sci. Process., 2018, 124, 485.
- 99 J. Sun, S. Li, X. Han, F. Liao, Y. Zhang, L. Gao, H. Chen and C. Xu, Rapid hydrothermal synthesis of snowflake-like ZnCo₂O₄/ZnO mesoporous microstructures with excellent electrochemical performances, Ceram. Int., 2019, 45, 12243-12250.
- 100 H. M. Shaikh, N. Siva Kumar and A. Mahmood, Synthesis of carbon nanoparticles/zinc oxide/zinc cobalt oxide composite and its electrochemical properties, Ceram. Int., 2020, 46, 18096-18100.
- 101 N. S. Kumar, V. R. Minnam Reddy, M. Asif, M. Boumaza and K. Mallikarjuna, Reaction time dependent in situ synthesized and morphology altered chrysanthemum to marigold -flower like zinc cobaltite and zinc oxide composite for energy storage devices, J. Taiwan Inst. Chem. Eng., 2020, 116, 92-100.
- 102 C. Huang, C. Hao, Z. Ye, S. Zhou, X. Wang, L. Zhu and J. Wu, In situ growth of ZIF-8-derived ternary ZnO/ ZnCo₂O₄/NiO for high performance asymmetric supercapacitors, Nanoscale, 2019, 11, 10114-10128.
- 103 L. Wang, Y. Guan, X. Zhao, J. Mu, H. Che, H. Li and Z. Guo, ZnCo₂O₄@MnCo₂O₄ heterojunction structured nanosheets for high-performance supercapacitor, J. Mater. Sci.: Mater. Electron., 2018, 29, 5782-5790.
- 104 A. J. Christina Mary, C. I. Sathish, P. S. Murphin Kumar, A. Vinu and A. C. Bose, Fabrication of hybrid supercapacitor device based on NiCo2O4@ZnCo2O4 and the biomassderived N-doped activated carbon with a honeycomb structure, Electrochim. Acta, 2020, 342, 136062.
- 105 S. Zhou, C. Hao, J. Wang, X. Wang and H. Gao, Metalorganic framework templated synthesis of porous NiCo₂O₄/ZnCo₂O₄/Co₃O₄ hollow polyhedral nanocages and their enhanced pseudocapacitive properties, Chem. Eng. J., 2018, 351, 74-84.
- 106 A. J. C. Mary, C. I. Sathish, A. Vinu and A. C. Bose, Electrochemical Performance of rGO/NiCo2O4@ZnCo2O4 Ternary Composite Material and the Fabrication of an all-Solid-State Supercapacitor Device, Energy Fuels, 2020, 34, 10131-10141.
- 107 Y. Huang, X. Feng, C. Li, Y. Li, X. Chen, X. Gao, C. Chen, Z. Guang and P. Liu, Construction of hydrangea-like ZnCo₂O₄/ Ni₃V₂O₈ hierarchical nanostructures for asymmetric all-solidstate supercapacitors, Ceram. Int., 2019, 45, 15451-15457.
- 108 V. S. Kumbhar and D.-H. Kim, Hierarchical coating of MnO2 nanosheets on ZnCo2O4 nanoflakes for enhanced electrochemical performance of asymmetric supercapacitors, Electrochim. Acta, 2018, 271, 284-296.
- 109 W. Cong, R. Miao, B. Tao and F. Miao, MnO₂/ZnCo₂O₄ with binder-free arrays on nickel foam loaded with graphene as a high performance electrode for advanced asymmetric supercapacitors, RSC Adv., 2019, 9, 32889-32897.
- 110 B. D. Boruah and A. Misra, Voltage Generation in Optically Sensitive Supercapacitor for Enhanced Performance, ACS Appl. Energy Mater., 2019, 2, 278-286.

111 T.-F. Yi, Y.-M. Li, J.-Z. Wu, Y. Xie and S. Luo, Hierarchical mesoporous flower-like ZnCo2O4@NiO nanoflakes grown on nickel foam as high-performance electrodes for supercapacitors, Electrochim. Acta, 2018, 284, 128-141.

- 112 Y. Tong, X. Cheng, D. Qi, B. Chi and W. Zhang, Hybrid ZnCo₂O₄@Co₃S₄ Nanowires for High-Performance Asymmetric Supercapacitors, J. Nanoelectron. Optoelectron., 2020, 15, 1552-1558.
- 113 X. Wang, P. Wu, Z. Zhao, L. Sun, Q. Deng, Z. Yin and X. Chen, Construction of flower-like ZnCo₂S₄/ZnCo₂O₄ arrays on Ni foam for high-performance asymmetric supercapacitors, J. Mater. Sci.: Mater. Electron., 2020, 31, 4895-4904.
- 114 J. Zhao, H. Li, C. Li, Q. Zhang, J. Sun, X. Wang, J. Guo, L. Xie, J. Xie, B. He, Z. Zhou, C. Lu, W. Lu, G. Zhu and Y. Yao, MOF for template-directed growth of well-oriented nanowire hybrid arrays on carbon nanotube fibers for wearable electronics integrated with triboelectric nanogenerators, Nano Energy, 2018, 45, 420-431.
- 115 X. Jia, X. Wu and B. Liu, Formation of ZnCo₂O₄@MnO₂ core-shell electrode materials for hybrid supercapacitor, Dalton Trans., 2018, 47, 15506-15511.
- 116 D. S. Patil, A. M. Teli, W. J. Choi, S. A. Pawar, J. C. Shin and H. J. Kim, An all chemical route to design a hybrid batterytype supercapacitor based on ZnCo2O4/CdS composite nanostructures, Curr. Appl. Phys., 2020, 20, 1416-1423.
- 117 D. Yang, Y. Wang, Q. Wang, W. Wang, T. Wei and Y. Sun, Preparation and supercapacitive properties of hierarchical ZnCo₂O₄@Ni₃S₂ core/shell nanowire arrays on Ni foam, Mater. Lett., 2018, 213, 222-226.
- 118 H. Xuan, H. Li, J. Gao, Y. Guan, Z. Xie, X. Liang, H. Li, P. Han and Y. Wu, Construction of hierarchical core-shell ZnCo₂O₄@Ni-Co-S nanosheets with a microsphere structure on nickel foam for high-performance asymmetric supercapacitors, Appl. Surf. Sci., 2020, 513, 145893.
- 119 Y. n Meng, D. Yu, Y. Teng, H. Qi, X. Liu, Y. Wu, X. Zhao and X. Liu, Coating of the NiMoO₄ nanosheets on differentmorphology ZnCo2O4 nanoarrays on Ni foam and their application in battery-supercapacitor hybrid devices, J. Energy Storage, 2020, 29, 101195.
- 120 J. Wang, S. Wang, Y. Tian, X. Jin and J. Dong, 3D heterogeneous ZnCo₂O₄@NiMoO₄ nanoarrays grown on Ni foam as a binder-free electrode for high-performance energy storage, J. Energy Storage, 2020, 32, 101899.
- 121 C. Chen, S. Wang, X. Luo, W. Gao, G. Huang, Y. Zeng and Z. Zhu, Reduced ZnCo₂O₄@NiMoO₄·H₂O heterostructure electrodes with modulating oxygen vacancies for enhanced aqueous asymmetric supercapacitors, J. Power Sources, 2019, 409, 112-122.
- 122 Y. n Meng, D. Yu, Y. Teng, X. Liu and X. Liu, A highperformance electrode based on the ZnCo2O4@CoMoO4 core-shell nanosheet arrays on nickel foam and their application in battery-supercapacitor hybrid device, Electrochim. Acta, 2020, 347, 136278.
- 123 L. Xie, Y. Liu, H. Bai, C. Li, B. Mao, L. Sun and W. Shi, Coreshell structured ZnCo2O4@ZnWO4 nanowire arrays on

- nickel foam for advanced asymmetric supercapacitors, J. Colloid Interface Sci., 2018, 531, 64-73.
- 124 L. Ma, Z. Chang, L. Guo, T. Li, G. Li and K. Wang, Stringlike core-shell ZnCo2O4@NiWO4 nanowire/nanosheet arrays on Ni foam for binder-free supercapacitor electrodes, Ionics, 2020, 26, 2537-2547.
- 125 Y. Anil Kumar, S. Sambasivam, S. Ahmed Hira, K. Zeb, W. Uddin, T. N. V. Krishna, K. Dasha Kumar, I. M. Obaidat and H.-J. Kim, Boosting the energy density of highly efficient flexible hybrid supercapacitors via selective integration of hierarchical nanostructured energy materials, Electrochim. Acta, 2020, 364, 137318.
- 126 X. Han, Y. Yang, J.-J. Zhou, Q. Ma, K. Tao and L. Han, Metal-Organic Framework Templated 3D Hierarchical ZnCo₂O₄(aNi(OH)₂ Core-Shell Nanosheet Arrays for High-Performance Supercapacitors, Chem. - Eur. J., 2018, 24, 18106-18114.
- 127 X. Bai, D. Cao and H. Zhang, Constructing ZnCo₂O₄@LDH Core-Shell hierarchical structure for high performance supercapacitor electrodes, Ceram. Int., 2019, 45, 14943-14952.
- 128 M. Li, W. Yang, Y. Huang and Y. Yu, Hierarchical mesoporous Co₃O₄@ZnCo₂O₄ hybrid nanowire arrays supported on Ni foam for high-performance asymmetric supercapacitors, Sci. China Mater., 2018, 61, 1167-1176.
- 129 L. Wu, L. Sun, X. Li, Q. Zhang, H. Si, Y. Zhang, K. Wang and Y. Zhang, Mesoporous ZnCo2O4-CNT microflowers as bifunctional material for supercapacitive and lithium energy storage, Appl. Surf. Sci., 2020, 506, 144964.
- 130 J. Bao, Z. Wang, W. Liu, L. Xu, F. Lei, J. Xie, Y. Zhao, Y. Huang, M. Guan and H. Li, ZnCo₂O₄ ultrathin nanosheets towards the high performance of flexible supercapacitors and bifunctional electrocatalysis, J. Alloys Compd., 2018, 764, 565-573.
- 131 A. Kathalingam, S. Ramesh, H. M. Yadav, J.-H. Choi, H. S. Kim and H.-S. Kim, Nanosheet-like ZnCo₂O₄@nitrogen doped graphene oxide/polyaniline composite for supercapacitor application: Effect of polyaniline incorporation, J. Alloys Compd., 2020, 830, 154734.
- 132 X. Wei, H. Wu and L. Li, 3D N-doped carbon continuous network supported P-doped ZnCo₂O₄ nanosheets with rich oxygen vacancies for high-performance asymmetric pseudocapacitor, J. Alloys Compd., 2021, 861, 158544.
- 133 S. J. Patil, D. P. Dubal and D.-W. Lee, Gold nanoparticles decorated rGO-ZnCo2O4 nanocomposite: A promising positive electrode for high performance hybrid supercapacitors, Chem. Eng. J., 2020, 379, 122211.
- 134 J. Bhagwan, G. Nagaraju, B. Ramulu and J. S. Yu, Promotive Effect of MWCNT on ZnCo₂O₄ Hexagonal Plates and Their Application in Aqueous Asymmetric Supercapacitor, J. Electrochem. Soc., 2019, 166, A217-A224.
- 135 M. Sharma and A. Gaur, Designing of Carbon Nitride Supported ZnCo₂O₄ Hybrid Electrode for High-Performance Energy Storage Applications, Sci. Rep., 2020, 10, 2035.
- 136 V. Shanmugavalli, O. V. Saravanan, K. Vishista and R. Saravanan, A study of charge density distribution and

Energy Advances

- enhanced electrochemical properties of zinc cobaltite/ polyaniline nanocomposite for supercapacitor application, Ionics, 2019, 25, 4393-4408.
- 137 Z. Gao, L. Zhang, J. Chang, Z. Wang, D. Wu, F. Xu, Y. Guo and K. Jiang, ZnCo₂O₄-reduced graphene oxide composite with balanced capacitive performance in asymmetric supercapacitors, Appl. Surf. Sci., 2018, 442, 138-147.
- 138 D. Kong, Y. Wang, S. Huang, J. Hu, Y. V. Lim, B. Liu, S. Fan, Y. Shi and H. Y. Yang, 3D self-branched zinc-cobalt Oxide@N-doped carbon hollow nanowall arrays for highperformance asymmetric supercapacitors and oxygen electrocatalysis, Energy Storage Mater., 2019, 23, 653-663.
- 139 M. Yan, F. Jiang, Y. Liu, L. Sun, H. Bai, F. Zhu and W. Shi, Flexible mixed metal oxide hollow spheres/RGO hybrid lamellar films for high performance supercapacitors, Colloids Surf., A, 2021, 612, 125902.
- 140 A. Asghari, S. H. Kazemi and M. Khanmohammadi, Facile and binder-free synthesis of N-doped carbon/ZnCo₂O₄ hybrid nanostructures on nickel foam for high-performance solid-state asymmetric supercapacitor, J. Mater. Sci.: Mater. Electron., 2020, 31, 4354-4363.
- 141 Z. Wang, S. Lu, G. He, A. Lv, Y. Shen and W. Xu, In situ construction of dual-morphology ZnCo2O4 for highperformance asymmetric supercapacitors, Nanoscale Adv., 2019, 1, 3086-3094.
- 142 J. Qi, J. Mao, A. Zhang, L. Jiang, Y. Sui, Y. He, Q. Meng, F. Wei and X. Zhang, Facile synthesis of mesoporous ZnCo₂O₄ nanosheet arrays grown on rGO as binder-free electrode for high-performance asymmetric supercapacitor, J. Mater. Sci., 2018, 53, 16074-16085.
- 143 Y. Lu, L. Wang, M. Chen, Y. Wu, G. Liu, P. Qi, M. Fu, H. Wu and Y. Tang, Rationally designed hierarchical ZnCo₂O₄/C core-shell nanowire arrays for high performance and stable supercapacitors, J. Alloys Compd., 2021, 876, 160037.
- 144 J. Zhu, Y. Wang, X. Zhang and W. Cai, MOF-derived ZnCo₂O₄@NiCo₂S₄@PPy core-shell nanosheets on Ni foam for high-performance supercapacitors, Nanotechnology, 2021, 32, 145404.
- 145 J. Gao, H. Xuan, Y. Xu, T. Liang, X. Han, J. Yang, P. Han, D. Wang and Y. Du, Interconnected network of zinc-cobalt layered double hydroxide stick onto rGO/nickel foam for high performance asymmetric supercapacitors, Electrochim. Acta, 2018, 286, 92-102.
- 146 P. Chen, C. Yang, P. Gao, X. Chen, Y.-J. Cheng, J. Liu and K. Guo, Distinctive Formation of Bifunctional ZnCoS-rGO 3D Hollow Microsphere Flowers with Excellent Energy Storage Performances, Chem. Mater., 2022, 34, 5896-5911.
- 147 M. Xu, M. Sun, S. u Rehman, K. Ge, X. Hu, H. Ding, J. Liu and H. Bi, One-pot synthesis of CoO-ZnO/rGO supported on Ni foam for high-performance hybrid supercapacitor with greatly enhanced cycling stability, Chin. Chem. Lett., 2021, 32, 2027-2032.
- 148 J. B. Goodenough and K.-S. Park, The Li-Ion Rechargeable Battery: A Perspective, J. Am. Chem. Soc., 2013, 135, 1167-1176.

- 149 X. Liu, J.-Q. Huang, Q. Zhang and L. Mai, Nanostructured Metal Oxides and Sulfides for Lithium-Sulfur Batteries, Adv. Mater., 2017, 29, 1601759.
- 150 B. Xu, D. Qian, Z. Wang and Y. S. Meng, Recent progress in cathode materials research for advanced lithium ion batteries, Mater. Sci. Eng., R, 2012, 73, 51-65.
- 151 S. Goriparti, E. Miele, F. De Angelis, E. Di Fabrizio, R. Proietti Zaccaria and C. Capiglia, Review on recent progress of nanostructured anode materials for Li-ion batteries, J. Power Sources, 2014, 257, 421-443.
- 152 J. Zhang, R. Chu, Y. Chen, H. Jiang, Y. Zhang, N. M. Huang and H. Guo, In-situ grown hierarchical ZnCo2O4 nanosheets on nickel foam as binder-free anode for lithium ion batteries, Ceram. Int., 2018, 44, 16219-16226.
- 153 Z. Li, D. Wang, A. Gu, W. Wei, H. Lv, Z. Lou and Q. Zhou, Ethylene glycol combustion strategy towards 3D mesoporous ZnCo₂O₄ as anodes for Li-ion batteries, Solid State Ionics, 2020, 356, 115461.
- 154 R. A. Adams, V. G. Pol and A. Varma, Tailored Solution Combustion Synthesis of High Performance ZnCo₂O₄ Anode Materials for Lithium-Ion Batteries, Ind. Eng. Chem. Res., 2017, 56, 7173-7183.
- 155 M. Wang, Y. Huang, Y. Zhu, N. Zhang, J. Zhang, X. Qin and H. Zhang, Synthesis of porous Zn_xCo_{3-x}O₄ hollow nanoboxes derived from metal-organic frameworks for lithium and sodium storage, Electrochim. Acta, 2020, 335, 135694.
- 156 J. Du, Y. Tang, Y. Wang, P. Shi, J. Fan, Q. Xu and Y. Min, A MOF-derived method to construct well-arranged porous nanosheets for lithium ion batteries, Dalton Trans., 2018, 47, 7571-7577.
- 157 Y. Song, M. Zhao, Z. Pan, L. Jiang, Y. Jiang, B. Fu, J. Xu and L. Hu, Thermal transformation of ZnCo_{1.5}(OH)_{4.5}Cl_{0.5}· 0.45H₂O into hexagonal ZnCo₂O₄ nanosheets for highperformance secondary ion batteries, J. Alloys Compd., 2019, 783, 455-459.
- 158 H. Xu, Y. Zhang, X. Song, X. Kong, T. Ma and H. Wang, Synthesis of porous ZnCo₂O₄ micro-cube with large tap density and its application in anode for lithium-ion battery, J. Alloys Compd., 2020, 821, 153289.
- 159 L. Wang, M. Zhen, F. Hu, H. Wang, H. Jia and M. Wei, Construction of three-dimensional ZnCo₂O₄ hierarchical nanocubes for enhanced lithium storage performances, Mater. Lett., 2021, 286, 129231.
- 160 Z. Chen, F. Chen, Y. Wang and Y. Jiang, Facile template-free one-pot fabrication of ZnCo2O4 nanospheres for advanced lithium storage capability, Ionics, 2017, 23, 3323-3328.
- 161 J. Deng, X. Yu, X. Qin, B. Li and F. Kang, Carbon spheretemplated synthesis of porous yolk-shell ZnCo₂O₄ spheres for high-performance lithium storage, J. Alloys Compd., 2019, 780, 65-71.
- 162 Y. Gu, Y. Xuan, H. Zhang, X. Deng, Y. Sun and L. Wang, A facile route to prepare mixed transition metal oxide yolkshell microspheres for enhanced lithium storage, Dalton Trans., 2019, 48, 10604-10609.
- 163 H. Liu and Q. Hu, Novel secondary assembled micro/nano porous spheres ZnCo2O4 with superior electrochemical

performances as lithium ion anode material, Nanotechnology, 2018, 29, 325603.

- 164 D. Xue, F. Xue, X. Lin, F. Zong, J. Zhang and Q. Li, Coordination polymer derived general synthesis of multishelled hollow metal oxides for lithium-ion batteries, Nanoscale, 2019, 11, 17478-17484.
- 165 H. Liu, X. Wang, H. Xu, J. Wang, Q. Ma, W. Yu, Y. Yang, X. Dong, G. Liu and Y. Zhao, Controllable synthesis of nanostructured ZnCo₂O₄ as high-performance anode materials for lithium-ion batteries, RSC Adv., 2018, 8, 39377-39383.
- 166 B. Liu, H. Liu, M. Liang, L. Liu, Z. Lv, H. Zhou and H. Guo, Controlled synthesis of hollow octahedral ZnCo2O4 nanocages assembled from ultrathin 2D nanosheets for enhanced lithium storage, Nanoscale, 2017, 9, 17174-17180.
- 167 S. Cheng, Q. Ru, P. Liu, H. Yan, Z. Shi, X. Hou, S. Su, L. Zhao and F. Chi-Chung, Ling, Micro-emulsion strategy used to prepare soybean oil-tailored 1D porous ZnCo₂O₄ cuboid morphology providing a durable performance of the anodes of lithium ion batteries, J. Alloys Compd., 2019, 809, 151703.
- 168 J. Deng, X. Yu, X. Qin, B. Liu, Y.-B. He, B. Li and F. Kang, Controlled synthesis of anisotropic hollow ZnCo₂O₄ octahedrons for high-performance lithium storage, Energy Storage Mater., 2018, 11, 184-190.
- 169 L. Zhang and S. Zhu, Hollow polyhedral ZnCo₂O₄ anode materials for lithium-ion batteries, Mater. Lett., 2019, 236, 337-341.
- 170 H. Du, K. Huang, W. Dong and B. Geng, A general gelatinassisted strategy to hierarchical porous transition metal oxides with excellent lithium-ion storage, Electrochim. Acta, 2018, 279, 66-73.
- 171 J. Liu, Y. Xuan, D. G. D. Galpaya, Y. Gu, Z. Lin, S. Zhang, C. Yan, S. Feng and L. Wang, A high-volumetric-capacity and high-areal-capacity ZnCo2O4 anode for Li-ion batteries enabled by a robust biopolymer binder, J. Mater. Chem. A, 2018, 6, 19455-19462.
- 172 M.-H. Jung, The two-dimensional to three-dimensional transition structures of ZnCo2O4 for the application of lithium-ion batteries, Appl. Surf. Sci., 2018, 427, 293-301.
- 173 C. R. Mariappan, V. Kumar, R. Azmi, L. Esmezjan, S. Indris, M. Bruns and H. Ehrenberg, High electrochemical performance of 3D highly porous Zn_{0.2}Ni_{0.8}Co₂O₄ microspheres as an electrode material for electrochemical energy storage, CrystEngComm, 2018, 20, 2159-2168.
- 174 Y. Mo, J. Liu, S. Wang, M. Xiao, S. Ren, D. Han and Y. Meng, Low-Carbon and Nanosheathed ZnCo₂O₄ Spheroids with Porous Architecture for Boosted Lithium Storage Properties, Research, 2019, 2019, 1354829.
- 175 D. Darbar, M. R. Anilkumar, V. Rajagopalan, I. Bhattacharya, H. I. Elim, T. Ramakrishnappa, F. I. Ezema, R. Jose and M. V. Reddy, Studies on spinel cobaltites, MCo₂O₄ (M = Mn, Zn, Fe, Ni and Co) and their functional properties, Ceram. Int., 2018, 44, 4630-4639.
- 176 M. Carbone, Zn defective ZnCo₂O₄ nanorods as high capacity anode for lithium ion batteries, J. Electroanal. Chem., 2018, 815, 151-157.

- 177 S. Guo, J. Liu, Q. Zhang and H. Wang, 3D porous ZnCo₂O₄/ Co₃O₄ composite grown on carbon cloth as highperformance anode material for lithium-ion battery, Mater. Lett., 2020, 267, 127549.
- 178 F. Li, M. Zheng, Y. You, D. Jiang, H. Yuan, Z. Zhai, W. Zhang, L. Ma and W. Shen, Hierarchical Hollow Bimetal Oxide Microspheres Synthesized through a Recrystallization Mechanism for High-Performance Lithium-Ion Batteries, ChemElectroChem, 2020, 7, 3468-3477.
- 179 W. Song, K. Ji, A. Aguadero, P. R. Shearing, D. J. L. Brett, F. Xie and D. J. Riley, Co₃O₄ hollow nanospheres doped with ZnCo2O4 via thermal vapor mechanism for fast lithium storage, Energy Storage Mater., 2018, 14, 324-334.
- 180 H. Mao, P. Shen, G. Yang, L. Zhao, X. Qiu, H. Wang and Q. Jiang, 3D highly oriented metal foam: a competitive selfsupporting anode for high-performance lithium-ion batteries, J. Mater. Sci., 2020, 55, 11462-11476.
- 181 H. Xin, D. Li, L. Shi, M. Ji, Y. Lin, J. Yu, B. Yang, C. Li and C. Zhu, A simple approach to fabricate of Ni-NiCo₂O₄(a) ZnCo₂O₄ yolk-shell nano-tetrahedron composite as highperformance anode material for lithium-ion batteries, Chem. Eng. J., 2018, 341, 601-609.
- 182 L. Wang and Q. Yang, ZnCo₂O₄ nanoflakes loaded on a Cusupported Fe₂O₃-C network as an integrated lithium-ion battery anode, J. Alloys Compd., 2019, 792, 750-758.
- 183 X. Deng, S. Li, J. Wang, D. Nan, J. Dong and J. Liu, Nitrogen-doped zinc/cobalt mixed oxide micro-/nanospheres for high-rate lithium-ion battery anode, I. Mater. Res., 2019, 34, 3204-3211.
- 184 J. Deng, X. Yu, X. Qin, D. Zhou, L. Zhang, H. Duan, F. Kang, B. Li and G. Wang, Co-B Nanoflakes as Multifunctional Bridges in ZnCo2O4 Micro-/Nanospheres for Superior Lithium Storage with Boosted Kinetics and Stability, Adv. Energy Mater., 2019, 9, 1803612.
- 185 L. Zhang, S. Zhu, X. Li, H. Fang, L. Wang, Y. Song and X. Jia, 3D porous ZnCo2O4@NiO on nickel foam as advanced electrodes for lithium storage, Ionics, 2020, 26, 2157-2164.
- 186 J. Yu, Y. Wang, L. Mou, D. Fang, S. Chen and S. Zhang, Nature-Inspired 2D-Mosaic 3D-Gradient Mesoporous Framework: Bimetal Oxide Dual-Composite Strategy toward Ultrastable and High-Capacity Lithium Storage, ACS Nano, 2018, 12, 2035-2047.
- 187 Z. Zhang, Y. Huang, X. Liu, X. Wang and P. Liu, Yolk-shell structured ZnCo2O4 spheres anchored on reduced graphene oxide with enhance lithium/sodium storage performance, Electrochim. Acta, 2020, 342, 136104.
- 188 H. Ren, W. Wang, S. Woo Joo, Y. Sun and C. Gu, Preparation of ZnCo₂O₄@reduced graphene oxide nanocomposite for high-capacity Li-ion battery anodes, Mater. Res. Bull., 2019, 111, 34-42.
- 189 Q. Feng, Y. Du, S. Liang and H. Li, Reduced graphene oxide supported quasi-two-dimensional ZnCo2O4 nanosheets for lithium ion batteries with high electrochemical stability, Nanotechnology, 2019, 31, 045402.
- 190 Q. Ru, Z. Wang, S. Cheng, P. Liu, X. Hou, S. Su and F. C.-C. Ling, Self Assembled Rice Ball-Like ZnCo₂O₄ Inlaid on rGO

- as Flexible Anodes with High Lithium Storage Capability and Superior Cycling Stability, Energy Technol., 2018, 6, 1899-1903.
- 191 X. Wang, Q. Chen, P. Zhao and M. Wang, Synthesis of interconnected mesoporous ZnCo2O4 nanosheets on a 3D graphene foam as a binder-free anode for high-performance Li-ion batteries, RSC Adv., 2018, 8, 33717-33727.
- 192 L. Li, Z. Xie, G. Jiang, Y. Wang, B. Cao and C. Yuan, Efficient Laser-Induced Construction of Oxygen-Vacancy Abundant Nano-ZnCo₂O₄/Porous Reduced Graphene Oxide Hybrids toward Exceptional Capacitive Lithium Storage, Small, 2020, 16, 2001526.
- 193 H. Cao, X. Zhou, W. Deng, Z. Ma, Y. Liu and Z. Liu, Layer structured graphene/porous ZnCo2O4 composite film for high performance flexible lithium-ion batteries, Chem. Eng. J., 2018, 343, 654-661.
- 194 Y. Yang, Z. Li, S. Xu, Y. Tang, C.-S. Lee and W. Zhang, Hierarchically nanostructured ZnCo₂O₄ particles in 3D graphene networks for high-rate and long-life lithium ion batteries, Mater. Today Energy, 2019, 12, 46-52.
- 195 Z. Zhao, G. Tian, V. Trouillet, L. Zhu, J. Zhu, A. Missiul, E. Welter and S. Dsoke, In Operando analysis of the charge storage mechanism in a conversion ZnCo2O4 anode and the application in flexible Li-ion batteries, Inorg. Chem. Front., 2019, 6, 1861-1872.
- 196 T. Huang, Z. Lou, Y. Lu, R. Li, Y. Jiang, G. Shen and D. Chen, Metal-Organic-Framework-Derived MCo₂O₄ (M = Mn and Zn) Nanosheet Arrays on Carbon Cloth as Integrated Anodes for Energy Storage Applications, ChemElectroChem, 2019, 6, 5836-5843.
- 197 T. Liu, W. Wang, M. Yi, Q. Chen, C. Xu, D. Cai and H. Zhan, Metal-organic framework derived porous ternary ZnCo₂O₄ nanoplate arrays grown on carbon cloth as binder-free electrodes for lithium-ion batteries, Chem. Eng. J., 2018, 354, 454-462.
- 198 P. Huang, M. Zhang, J. Kang, H. Feng, Q. Su, G. Du, Y. Yu and B. Xu, Rapid microwave-irradiation synthesis of ZnCo2O4/ZnO nanocrystals/carbon nanotubes composite as anodes for high-performance lithium-ion battery, J. Mater. Sci., 2018, 54, 4154-4167.
- 199 Y. Wang, X. Zhu, D. Liu, H. Tang, G. Luo, K. Tu, Z. Xie, J. Lei, J. Li, X. Li and D. Qu, Synthesis of MOF-74-derived carbon/ZnCo2O4 nanoparticles@CNT-nest hybrid material and its application in lithium ion batteries, J. Appl. Electrochem., 2019, 49, 1103-1112.
- 200 X. Tang, M. Liang, Y. Zhang, W. Sun and Y. Wang, Ultrafine ternary metal oxide particles with carbon nanotubes: a metalorganic-framework-based approach and superior lithiumstorage performance, Dalton Trans., 2019, 48, 4413-4419.
- 201 H. Liang, J. Wu, M. Wang, H. Fan and Y. Zhang, Pseudocapacitance-dominated high-performance and stable lithiumion batteries from MOF-derived spinel ZnCo2O4/ZnO/C heterostructure anode, Dalton Trans., 2020, 49, 13311-13316.
- 202 C. Ding, W. Xu, X. Zeng, M. Wang, W. Wang and Z. Qing, Citrate-directed hydrothermal synthesis of ZnCo2O4-incarbon porous microspheres for highly reliable lithiumion batteries, Ionics, 2019, 26, 703-710.

- 203 L. Wang, D. Li, J. Zhang, C. Song, H. Xin and X. Qin, Porous flower-like ZnCo₂O₄ and ZnCo₂O₄@C composite: a facile controllable synthesis and enhanced electrochemical performance, Ionics, 2020, 26, 4479-4487.
- 204 C. Ding, W. Xu, M. Wang, X. Zeng and W. Wang, Microstructure controlled ZnCo2O4/C microhydrangea nanocomposites as highly reliable anodes for lithium-ion batteries, Int. J. Energy Res., 2019, 44, 977-987.
- 205 H. Li, S. Wang, M. Feng, J. Yang and B. Zhang, MOFderived ZnCo2O4/C wrapped on carbon fiber as anode materials for structural lithium-ion batteries, Chin. Chem. Lett., 2019, 30, 529-532.
- 206 Z. Dai, Z. Long, R. Li, C. Shi, H. Qiao, K. Wang and K. Liu, Metal-Organic Framework-Structured Porous ZnCo2O4/C Composite Nanofibers for High-Rate Lithium-Ion Batteries, ACS Appl. Energy Mater., 2020, 3, 12378-12384.
- 207 R. Sun, Z. Qin, Z. Li, H. Fan and S. Lu, Binary zinc-cobalt metal-organic framework derived mesoporous ZnCo₂O₄@NC polyhedron as a high-performance lithium-ion battery anode, Dalton Trans., 2020, 49, 14237-14242.
- 208 X. Wu, M. Zeng, L. Wang and J. Li, CTAB-assisted synthesis of ZnCo₂O₄ nanoparticles embedded in N-doped carbon as superior anode materials for lithium-ion battery, J. Alloys Compd., 2019, 780, 897-906.
- 209 W. Zhao, Z. Shi, Y. Qi and J. Cheng, The Carbon-Coated ZnCo₂O₄ Nanowire Arrays Pyrolyzed from PVA for Enhancing Lithium Storage Capacity, Processes, 2020, 8, 1501.
- 210 O. Han, X. Zhang, W. Zhang, Y. Li and Z. Zhang, Preparation of multifunctional structural P-CF@ZnCo2O4 composites used as structural anode materials, J. Alloys Compd., 2020, 842, 155743.
- 211 H. Xiao, G. Ma, J. Tan, S. Ru, Z. Ai and C. Wang, Threedimensional hierarchical ZnCo₂O₄@C₃N₄-B nanoflowers as high-performance anode materials for lithium-ion batteries, RSC Adv., 2020, 10, 32609-32615.
- 212 P. Pan, Y. Hu, K. Wu, Z. Cheng, Z. Shen, L. Jiang, J. Mao, C. Ni, Y. Ge and Z. Wang, Growth of ZnCo₂O₄ nanocubes on flexible biochar substrate derived from natural silk waste fabric for lithium-ion battery anode, J. Alloys Compd., 2020, 814, 152306.
- 213 H. Li, L. Lv, W. Wang, X. Huang and D. Chen, A network of porous carbon/ZnCo2O4 nanotubes derived from shellhybridized worm-like micelles for lithium storage, J. Mater. Chem. A, 2019, 7, 22642-22649.
- 214 J. Deng, X. Yu, J. Tang, L. Zhang, K. Zhang, S. Lin and B. Li, Highly reversible lithium storage in a conversion-type $ZnCo_2O_4$ anode promoted by $NiCl_{2-x}F_x$ hydrate, *J. Mater.* Chem. A, 2020, 8, 2356-2363.
- 215 A. Ghaffar, G. Ali, S. Zawar, M. Hasan, G. M. Mustafa, S. Atiq and S. M. Ramay, Electrochemical performance of Li+ insertion/extraction in Ni-substituted ZnCo₂O₄ as an emerging highly efficient anode material, RSC Adv., 2020, **10**, 28550–28559.
- 216 C. Liu, B.-H. Chen, W.-R. Liu and J.-G. Duh, Synthesis and theoretical calculations of N-doped ZnCo2O4 anode for lithium-ion anode via gradient pressure-induced processes

and theoretical calculations, J. Alloys Compd., 2019, 797, 978-985.

- 217 W.-T. Koo, H.-Y. Jang, C. Kim, J.-W. Jung, J. Y. Cheong and I.-D. Kim, MOF derived ZnCo₂O₄ porous hollow spheres functionalized with Ag nanoparticles for a long-cycle and high-capacity lithium ion battery anode, J. Mater. Chem. A, 2017, 5, 22717-22725.
- 218 W. Zhao, Y. Qi, J. Dong, J. Xu, P. Wu and C. Zhang, New insights into the structure-property relation in ZnCo₂O₄ nanowire and nanosheet arrays, J. Alloys Compd., 2020, 817, 152692.
- 219 X. Cao, Y. Yang and A. Li, Facile Synthesis of Porous ZnCo(2)O(4) Nanosheets and the Superior Electrochemical Properties for Sodium Ion Batteries, Nanomaterials, 2018, 8(6), 377, DOI: 10.3390/nano8060377.
- 220 X. Yang, P. Wang, Y. Tang, C. Peng, Y. Lai, J. Li and Z. Zhang, Bimetallic ZIF-derived polyhedron ZnCo₂O₄ anchored on the reduced graphene oxide as an anode for sodium-ion battery, Ionics, 2019, 25, 2945-2950.
- 221 J. Xu, B. Yan, H. Maleki Kheimeh Sari, Y. Hao, D. Xiong, S. Dou, W. Liu, H. Kou, D. Li and X. Li, Mesoporous ZnCo₂O₄/rGO nanocomposites enhancing sodium storage, Nanotechnology, 2019, 30, 234005.
- 222 J. Liu, J. Wu, C. Zhou, P. Zhang, S. Guo, S. Li, Y. Yang, K. Li, L. Chen and M. Wang, Single-phase ZnCo₂O₄ derived ZnO-CoO mesoporous microspheres encapsulated by nitrogendoped carbon shell as anode for high-performance lithium-ion batteries, J. Alloys Compd., 2020, 825, 153951.
- 223 T. Huang, Z. Lou, Y. Lu, R. Li, Y. Jiang, G. Shen and D. Chen, Metal-Organic-Framework-Derived MCo₂O₄ (M = Mn and Zn) Nanosheet Arrays on Carbon Cloth as Integrated Anodes for Energy Storage Applications, ChemElectroChem, 2019, 6, 5836-5843.
- 224 A. K. Geim and K. S. Novoselov, The rise of graphene, Nat. mater., 2007, 6, 183-191.
- 225 C. N. Rao, A. K. Sood, K. S. Subrahmanyam and A. Govindaraj, Graphene: the new two-dimensional nanomaterial, Angew. Chem., Int. Ed., 2009, 48, 7752-7777.
- 226 C. N. Rao, K. S. Subrahmanyam, H. S. Ramakrishna Matte, B. Abdulhakeem, A. Govindaraj, B. Das, P. Kumar, A. Ghosh and D. J. Late, A study of the synthetic methods and properties of graphenes, Sci. Technol. Adv. Mater., 2010, 11, 054502.
- 227 C.-H. Park, F. Giustino, C. D. Spataru, M. L. Cohen and S. G. Louie, Angle-Resolved Photoemission Spectra of Graphene from First-Principles Calculations, Nano Lett., 2009, 9, 4234-4239.
- 228 S. Sahoo, S.-H. Bae, Y.-S. Lee, J.-M. Lee, J.-M. Ahn, C.-G. Kim and I.-K. Oh, Defect-engineered mesoporous ternary nanoarchitecture of zinc-cobalt-oxide/nitrogen-doped graphene as anode material in lithium ion batteries, Carbon, 2015, 94, 455-463.
- 229 X. Song, X. Li, Z. Bai, B. Yan, D. Xiong, L. Lin, H. Zhao, D. Li and Y. Shao, Rationally-designed configuration of directly-coated Ni₃S₂/Ni electrode by RGO providing superior sodium storage, Carbon, 2018, 133, 14-22.

- 230 J. M. Gonçalves, P. R. Martins, M. I. da Silva, J. G. Ruiz-Montoya, L. V. Quispe-Garrido and A. Lucio, in Handbook of Energy Materials, ed. R. Gupta, Springer Nature Singapore, Singapore, 2022, pp. 1-46, DOI: 10.1007/978-981-16-4480-1 19-1.
- 231 N. Yabuuchi, K. Kubota, M. Dahbi and S. Komaba, Research Development on Sodium-Ion Batteries, Chem. Rev., 2014, 114, 11636-11682.
- 232 C. Yuan, H. B. Wu, Y. Xie and X. W. Lou, Mixed Transition-Metal Oxides: Design, Synthesis, and Energy-Related Applications, Angew. Chem., Int. Ed., 2014, 53, 1488-1504.
- 233 J. Muldoon, C. B. Bucur and T. Gregory, Quest for Nonaqueous Multivalent Secondary Batteries: Magnesium and Beyond, Chem. Rev., 2014, 114, 11683-11720.
- 234 C. Pan, R. Zhang, R. G. Nuzzo and A. A. Gewirth, ZnNixMnxCo_{2-2x}O₄ Spinel as a High-Voltage and High-Capacity Cathode Material for Nonaqueous Zn-Ion Batteries, Adv. Energy Mater., 2018, 8, 1800589.
- 235 A. Baby, B. Senthilkumar and P. Barpanda, Low-Cost Rapid Template-Free Synthesis of Nanoscale Zinc Spinels for Energy Storage and Electrocatalytic Applications, ACS Appl. Energy Mater., 2019, 2, 3211-3219.
- 236 K. Shimokawa, T. Atsumi, M. Harada, R. E. Ward, M. Nakayama, Y. Kumagai, F. Oba, N. L. Okamoto, K. Kanamura and T. Ichitsubo, Zinc-based spinel cathode materials for magnesium rechargeable batteries: toward the reversible spinel-rocksalt transition, J. Mater. Chem. A, 2019, 7, 12225-12235.
- 237 P. G. Bruce, S. A. Freunberger, L. J. Hardwick and J. M. Tarascon, Li-O₂ and Li-S batteries with high energy storage, Nat. Mater., 2011, 11, 19-29.
- 238 M. Du, Q. Li, Y. Zhao, C.-S. Liu and H. Pang, A review of electrochemical energy storage behaviors based on pristine metal-organic frameworks and their composites, Coord. Chem. Rev., 2020, 416, 213341.
- 239 X. Ji, K. T. Lee and L. F. Nazar, A highly ordered nanostructured carbon-sulphur cathode for lithium-sulphur batteries, Nat. Mater., 2009, 8, 500-506.
- 240 M. Yan, W.-P. Wang, Y.-X. Yin, L.-J. Wan and Y.-G. Guo, Interfacial design for lithium-sulfur batteries: From liquid to solid, *EnergyChem*, 2019, **1**, 100002.
- 241 G. Zhou, Y. Zhao and A. Manthiram, Dual-Confined Flexible Sulfur Cathodes Encapsulated in Nitrogen-Doped Double-Shelled Hollow Carbon Spheres and Wrapped with Graphene for Li-S Batteries, Adv. Energy Mater., 2015, 5, 1402263.
- 242 Q. Sun, B. Xi, J.-Y. Li, H. Mao, X. Ma, J. Liang, J. Feng and S. Xiong, Nitrogen-Doped Graphene-Supported Mixed Transition-Metal Oxide Porous Particles to Confine Polysulfides for Lithium-Sulfur Batteries, Adv. Energy Mater., 2018, 8, 1800595.
- 243 J. S. Yeon, T. H. Park, Y. H. Ko, P. Sivakumar, J. S. Kim, Y. Kim and H. S. Park, 2D spinel ZnCo₂O₄ microsheetcoated functional separator for promoted redox kinetics and inhibited polysulfide dissolution, J. Energy Chem., 2021, 55, 468-475.

- 244 F. Wu, J. Bai, J. Feng and S. Xiong, Porous mixed metal oxides: design, formation mechanism, and application in lithium-ion batteries, Nanoscale, 2015, 7, 17211-17230.
- 245 H. Zhang, J. Liu, X. Lin, Y. Zhong, J. Ren, Z. Wang, T. Han and J. Li, A metal organic foam-derived zinc cobalt sulfide with improved binding energies towards polysulfides for lithium-sulfur batteries, Ceram. Int., 2020, 46, 14056-14063.
- 246 M. A. Rahman, X. Wang and C. Wen, High Energy Density Metal-Air Batteries: A Review, J. Electrochem. Soc., 2013, 160, A1759-A1771.
- 247 Q. Wang, L. Shang, R. Shi, X. Zhang, G. I. N. Waterhouse, L.-Z. Wu, C.-H. Tung and T. Zhang, 3D carbon nanoframe scaffold-immobilized Ni₃FeN nanoparticle electrocatalysts for rechargeable zinc-air batteries' cathodes, Nano Energy, 2017, 40, 382-389.
- 248 M. Dong, X. Liu, L. Jiang, Z. Zhu, Y. Shu, S. Chen, Y. Dou, P. Liu, H. Yin and H. Zhao, Cobalt-doped Mn₃O₄ nanocrystals embedded in graphene nanosheets as a highperformance bifunctional oxygen electrocatalyst for rechargeable Zn-Air batteries, Green Energy Environ., 2020, 5, 499-505.
- 249 Q. Wang, L. Shang, R. Shi, X. Zhang, Y. Zhao, G. I. N. Waterhouse, L.-Z. Wu, C.-H. Tung and T. Zhang, NiFe Layered Double Hydroxide Nanoparticles on Co,N-Codoped Carbon Nanoframes as Efficient Bifunctional Catalysts for Rechargeable Zinc-Air Batteries, Adv. Energy Mater., 2017, 7, 1700467.
- 250 Y. Huang, Y. Wang, C. Tang, J. Wang, Q. Zhang, Y. Wang and J. Zhang, Atomic Modulation and Structure Design of Carbons for Bifunctional Electrocatalysis in Metal-Air Batteries, Adv. Mater., 2019, 31, 1803800.
- 251 J.-C. Kim, G.-H. Lee, S. Lee, S.-I. Oh, Y. Kang and D.-W. Kim, Tailored Porous ZnCo₂O₄ Nanofibrous Electrocatalysts for Lithium-Oxygen Batteries, Adv. Mater. Interfaces, 2018, 5, 1701234.
- 252 J. M. Costa, M. P. Clark, A. F. de Almeida Neto and D. G. Ivey, In-situ transformation of electrodeposited W-Co oxide to ZnCo₂O₄ nanoparticles as an effective bifunctional catalysts in Zn-air batteries, Int. J. Hydrogen Energy, 2020, 45, 16122-16132.
- 253 Z. Mai, W. Duan, K. Wang, Z. Tang and S. Chen, Integrat-ZnCo₂O₄ submicro/nanospheres with CoxSey nanosheets for the oxygen evolution reaction and zincair batteries, Sustainable Energy Fuels, 2020, 4, 2184-2191.
- 254 N. Xu, Q. Nie, J. Liu, H. Huang, J. Qiao and X.-D. Zhou, Insert Zn²⁺ in Tetrahedral Sites of Bi-metal Zn-Co Spinel Oxides with High Oxygen Catalytic Performance for Liquid and Flexible Zinc-Air Batteries, J. Electrochem. Soc., 2020, 167, 050512.
- 255 L. Yan, Z. Xu, W. Hu, J. Ning, Y. Zhong and Y. Hu, Formation of sandwiched leaf-like CNTs-Co/ZnCo2O4@ NC-CNTs nanohybrids for high-power-density rechargeable Zn-air batteries, Nano Energy, 2021, 82, 105710.
- 256 Y.-P. Deng, Y. Jiang, D. Luo, J. Fu, R. Liang, S. Cheng, Z. Bai, Y. Liu, W. Lei, L. Yang, J. Zhu and Z. Chen, Hierarchical Porous Double-Shelled Electrocatalyst with

- Tailored Lattice Alkalinity toward Bifunctional Oxygen Reactions for Metal-Air Batteries, ACS Energy Lett., 2017, 2, 2706-2712.
- 257 W. Yan, X. Cao, J. Tian, C. Jin, K. Ke and R. Yang, Nitrogen/ sulfur dual-doped 3D reduced graphene oxide networkssupported CoFe₂O₄ with enhanced electrocatalytic activities for oxygen reduction and evolution reactions, Carbon, 2016, 99, 195-202.
- 258 T.-W. Chen, P. Kalimuthu, G. Anushya, S.-M. Chen, R. Ramachandran, V. Mariyappan and D. C. Muthumala, High-Efficiency of Bi-Functional-Based Perovskite Nanocomposite for Oxygen Evolution and Oxygen Reduction Reaction: An Overview, Materials, 2021, 14, 2976, DOI: 10.3390/ma14112976.
- 259 J. H. Li, M. Y. Liu, Y. Li, L. Yuan, P. Zhang, Z. Cai, H. Chen and J. L. Zou, ZIF-8@ZIF-67-derived ZnCo2O4@nitrogendoped carbon/carbon nanotubes wrapped by a carbon layer: a stable oxygen reduction catalyst with a competitive strength in acid media, Mater. Today Energy, 2021, 19, 100574.
- 260 N. Tao, J. Liu, B. Wang, C. Liang, S. Lin, Y. Du, D. Fan, H. Yang, Y. Wang and K. Huang, Hydrothermal twodimensionalisation to porous ZnCo2O4 nanosheets nonplatinum ORR catalyst, Micro Nano Lett., 2019, 14, 665-668.
- 261 S. Chakrabarty, A. Mukherjee, W.-N. Su and S. Basu, Improved bi-functional ORR and OER catalytic activity of reduced graphene oxide supported ZnCo₂O₄ microsphere, Int. J. Hydrogen Energy, 2019, 44, 1565-1578.
- 262 T. V. M. Sreekanth, P. C. Nagajyothi, K. C. Devarayapalli, J. Shim and K. Yoo, Lilac flower-shaped ZnCo₂O₄ electrocatalyst for efficient methanol oxidation and oxygen reduction reactions in an alkaline medium, CrystEng-Comm, 2020, 22, 2849-2858.
- 263 Y. Liu, H. Jiang, J. Hao, Y. Liu, H. Shen, W. Li and J. Li, Metal-Organic Framework-Derived Reduced Graphene Oxide-Supported ZnO/ZnCo2O4/C Hollow Nanocages as Cathode Catalysts for Aluminum-O2 Batteries, ACS Appl. Mater. Interfaces, 2017, 9, 31841-31852.
- 264 Y. Zheng, Y. Jiao, Y. Zhu, Q. Cai, A. Vasileff, L. H. Li, Y. Han, Y. Chen and S.-Z. Qiao, Molecule-Level g-C₃N₄ Coordinated Transition Metals as a New Class of Electrocatalysts for Oxygen Electrode Reactions, J. Am. Chem. Soc., 2017, 139, 3336-3339.
- 265 Y. P. Zhu, T. Y. Ma, M. Jaroniec and S. Z. Qiao, Self-Templating Synthesis of Hollow Co₃O₄ Microtube Arrays for Highly Efficient Water Electrolysis, Angew. Chem., Int. Ed., 2017, 56, 1324-1328.
- 266 J. Béjar, L. Álvarez-Contreras, J. Ledesma-García, N. Arjona and L. G. Arriaga, Electrocatalytic evaluation of Co₃O₄ and NiCo2O4 rosettes-like hierarchical spinel as bifunctional materials for oxygen evolution (OER) and reduction (ORR) reactions in alkaline media, J. Electroanal. Chem., 2019, 847, 113190.
- 267 J. Ge, W. Zhang, J. Tu, T. Xia, S. Chen and G. Xie, Suppressed Jahn-Teller Distortion in MnCo2O4@Ni2P Heterostructures to Promote the Overall Water Splitting, Small, 2020, 16, 2001856.

268 Y. Tan, C. Wu, H. Lin, J. Li, B. Chi, J. Pu and L. Jian, Insight the effect of surface Co cations on the electrocatalytic oxygen evolution properties of cobaltite spinels, Electrochim. Acta, 2014, 121, 183-187.

- 269 T. W. Kim, M. A. Woo, M. Regis and K.-S. Choi, Electrochemical Synthesis of Spinel Type ZnCo₂O₄ Electrodes for Use as Oxygen Evolution Reaction Catalysts, J. Phys. Chem. Lett., 2014, 5, 2370-2374.
- 270 K. Xiang, D. Wu, Y. Fan, W. You, D. Zhang, J.-L. Luo and X.-Z. Fu, Enhancing bifunctional electrodes of oxygen vacancy abundant ZnCo2O4 nanosheets for supercapacitor and oxygen evolution, Chem. Eng. J., 2021, 425, 130583.
- 271 S. Sun, Y. Sun, Y. Zhou, J. Shen, D. Mandler, R. Neumann and Z. J. Xu, Switch of the Rate-Determining Step of Water Oxidation by Spin-Selected Electron Transfer in Spinel Oxides, Chem. Mater., 2019, 31, 8106-8111.
- 272 D. Zhang, Z. Wang, J. Li, C. Hu, X. Zhang, B. Jiang, Z. Cao, J. Zhang and R. Zhang, MOF-derived ZnCo₂O₄ porous micro-rice with enhanced electro-catalytic activity for the oxygen evolution reaction and glucose oxidation, RSC Adv., 2020, 10, 9063-9069.
- 273 A. Amirzhanova, N. Akmanşen, I. Karakaya and Ö. Dag, Mesoporous MnCo₂O₄, NiCo₂O₄, and ZnCo₂O₄ Thin-Film Electrodes as Electrocatalysts for the Oxygen Evolution Reaction in Alkaline Solutions, ACS Appl. Energy Mater., 2021, 4, 2769-2785.
- 274 G. M. Tomboc, F. O. Agyemang and H. Kim, Improved electrocatalytic oxygen evolution reaction properties using PVP modified direct growth Co-based metal oxides electrocatalysts on nickel foam, Electrochim. Acta, 2018, 263, 362-372.
- 275 D. Zhao, M. Dai, H. Liu, X. Zhu and X. Wu, PPy film anchored on ZnCo₂O₄ nanowires facilitating efficient bifunctional electrocatalysis, Mater. Today Energy, 2021, 20, 100637.
- 276 J. Liu, Y. Xie, Y. Nan, G. Gou, X. Li, Y. Fang, X. Wang, Y. Tang, H. Yang and J. Ma, ZnCo₂O₄ nanoparticles derived from dual-metal-organic-frameworks embedded in Multiwalled Carbon Nanotubes: a favorable electrocatalyst for the water splitting, Electrochim. Acta, 2017, 257, 233-242.
- 277 M. Dai, H. Liu, D. Zhao, X. Zhu, A. Umar, H. Algarni and X. Wu, Ni Foam Substrates Modified with a ZnCo₂O₄ Nanowire-Coated Ni(OH)2 Nanosheet Electrode for Hybrid Capacitors and Electrocatalysts, ACS Appl. Nano Mater., 2021, 4, 5461-5468.
- 278 J. Pan, F. Wang, L. Zhang, S. Song and H. Zhang, Clean synthesis of ZnCo₂O₄@ZnCo-LDHs yolk-shell nanospheres composed of ultra-thin nanosheets with enhanced electrocatalytic properties, Inorg. Chem. Front., 2019, 6, 220-225.
- 279 R. Que, S. Liu, Y. Yang and Y. Pan, High catalytic performance of core-shell structure ZnCo2O4@NiFe LDH for oxygen evolution reaction, Mater. Lett., 2021, 298, 129982.
- 280 Z. Yu, Y. Bai, N. Zhang, W. Yang, J. Ma, Z. Wang, W. Sun, J. Qiao and K. Sun, Metal-organic framework-derived heterostructured ZnCo2O4@FeOOH hollow polyhedrons for

- oxygen evolution reaction, J. Alloys Compd., 2020, 832, 155067.
- 281 H. Cheng, C.-Y. Su, Z.-Y. Tan, S.-Z. Tai and Z.-Q. Liu, Interacting ZnCo2O4 and Au nanodots on carbon nanotubes as highly efficient water oxidation electrocatalyst, J. Power Sources, 2017, 357, 1-10.
- 282 T. Xiong, Z. Tan, Y. Mi, Q. Huang, Y. Tan, X. Yin and F. Hu, On-site generated metal organic framework-deriving core/ shell ZnCo₂O₄/ZnO nanoarray for better water oxidation, Nanotechnology, 2019, 30, 495405.
- 283 C. Zhang, Y. Pan, C. Ouyang, X. Li, X. Quan, Z. Hong and M. Zhi, Template-Free Synthesis of Zinc Cobalt Oxides/ Phosphides (Co₂P/CoO/ZnCo₂O₄) Hollow Sub-Micron Boxes as Hydrogen Evolution Reaction Catalysts, ChemistrySelect, 2021, 6, 1685-1691.
- 284 S. Debata, S. Patra, S. Banerjee, R. Madhuri and P. K. Sharma, Controlled hydrothermal synthesis of graphene supported NiCo₂O₄ coral-like nanostructures: An efficient electrocatalyst for overall water splitting, Appl. Surf. Sci., 2018, 449, 203-212.
- 285 C. Shenghai, S. Liping, K. Fanhao, H. Lihua and Z. Hui, Carbon-coated MnCo2O4 nanowire as bifunctional oxygen catalysts for rechargeable Zn-air batteries, J. Power Sources, 2019, 430, 25-31.
- 286 X. Jia, S. Gao, T. Liu, D. Li, P. Tang and Y. Feng, Controllable Synthesis and Bi-functional Electrocatalytic Performance towards Oxygen Electrode Reactions of Co₃O₄/N-RGO Composites, Electrochim. Acta, 2017, 226, 104-112.
- 287 A. Rebekah, S. Anantharaj, C. Viswanthan and N. Ponpandian, Zn-substituted MnCo₂O₄ nanostructure anchored over rGO for boosting the electrocatalytic performance towards methanol oxidation and oxygen evolution reaction (OER), Int. J. Hydrogen Energy, 2020, 45, 14713-14727.
- 288 D. Tang, Y. Han, W. Ji, S. Qiao, X. Zhou, R. Liu, X. Han, H. Huang, Y. Liu and Z. Kang, A high-performance reduced graphene oxide/ZnCo layered double hydroxide electrocatalyst for efficient water oxidation, Dalton Trans., 2014, 43, 15119-15125.
- 289 J. M. Gonçalves, P. R. Martins, L. Angnes and K. Araki, Recent advances in ternary layered double hydroxide electrocatalysts for the oxygen evolution reaction, New J. Chem., 2020, 44, 9981-9997.
- 290 J. P. Kumar, S. D. Giri and A. Sarkar, Mesoporous NiO with different morphology: Synthesis, characterization and their evaluation for oxygen evolution reaction, Int. J. Hydrogen Energy, 2018, 43, 15639-15649.
- 291 M. Kashif, M. Fiaz and M. Athar, One-step hydrothermal synthesis of ZnO nanorods as efficient oxygen evolution reaction catalyst, Inorg. Nano-Met. Chem., 2022, 52, 101-107.
- 292 N. Kim, D. Lim, Y. Choi, S. E. Shim and S.-H. Baeck, Hexagonal β-Ni(OH)₂ nanoplates with oxygen vacancies as efficient catalysts for the oxygen evolution reaction, Electrochim. Acta, 2019, 324, 134868.
- 293 X. Du, Z. Yang, Y. Li, Y. Gong and M. Zhao, Controlled synthesis of Ni(OH)2/Ni3S2 hybrid nanosheet arrays as

- highly active and stable electrocatalysts for water splitting, *J. Mater. Chem. A*, 2018, **6**, 6938–6946.
- 294 M. I. da Silva, Í. R. Machado, H. E. Toma, K. Araki, L. Angnes and J. M. Gonçalves, Recent progress in water-splitting and supercapacitor electrode materials based on MOF-derived sulfides, *J. Mater. Chem. A*, 2022, **10**, 430–474.
- 295 L. Zhang, Q. Fan, K. Li, S. Zhang and X. Ma, First-row transition metal oxide oxygen evolution electrocatalysts: regulation strategies and mechanistic understandings, *Sustainable Energy Fuels*, 2020, **4**, 5417–5432.
- 296 T. G. Ritter, A. H. Phakatkar, M. G. Rasul, M. T. Saray, L. V. Sorokina, T. Shokuhfar, J. M. Gonçalves and R. Shahbazian-

- Yassar, Electrochemical synthesis of high entropy hydroxides and oxides boosted by hydrogen evolution reaction, *Cell Rep. Phys. Sci.*, 2022, **3**, 100847.
- 297 L. Yu, T. Liu, R. Amine, J. Wen, J. Lu and K. Amine, High Nickel and No Cobalt—The Pursuit of Next-Generation Layered Oxide Cathodes, *ACS Appl. Mater. Interfaces*, 2022, 14(20), 23056–23065, DOI: 10.1021/acsami.1c22091.
- 298 J. M. Gonçalves, P. Roberto Martins, D. P. Rocha, T. A. Matias, M. S. Julião, R. A. Abarza Munoz and L. Angnes, Recent trends and perspectives in electrochemical sensors based on MOF-derived materials, *J. Mater. Chem. C*, 2021, 9(28), 8718–8745, DOI: 10.1039/d1tc02025k.